Terahertz Astronomy

Cryogenic IF Design Calibration and Measurement

by

Marko Neric

A Dissertation Presented in Partial Fulfillment
of the Requirements for the Degree
Doctor of Philosophy

Approved April 2023 by the
Graduate Supervisory Committee:

Chris Groppi, Chair
Philip Mauskopf
Paul Scowen
Georgios Trichopoulos
Daniel Jacobs

ARIZONA STATE UNIVERSITY

May 2023

ABSTRACT

Studying the interstellar medium (ISM) is the key to answering questions about how material that exists between the stars drives the evolution of galaxies. Current models for the ISM life-cycle exist, but several steps lack observational evidence. In this dissertation I present the work I completed in support of up-coming mission to further study the ISM. This work includes ancillary data analysis of the Carina Nebula for the upcoming balloon mission: astrophysics stratospheric telescope for high spectral resolution observations at submillimeter wavelengths (ASTHROS). I present a derived molecular gas map of Carina from Herschel dust continuum emission maps at wavelengths between 70-500 microns. I compare it to the distribution of atomic gas, using HI 21 cm data, and of multiple CO isotopologues for the $J = 1 \rightarrow 0$ rotational transition. I use these data sets to separate the CO–dark and CO–bright molecular components to study their relative contribution to the total molecular gas mass budget in Carina. I studied the transition between atomic and molecular gas in this region, by deriving the molecular fraction as a function of position, and comparing it to theoretical models of this transition. I also present the flight hardware design, testing, and space qualification of the intermediate frequency (IF) harness for the galactic/extragalactic ultra long duration balloon spectroscopic terahertz observatory (GUSTO). The harness transmits signal via novel cryogenic flexible stripline based transmission lines operating from 0.3 - 6.0 GHz. I designed three sets of 8-channel ribbons with characteristic insertion loss of 3.07 dB ft^{-1} at 5 GHz while the line was at a temperature gradient between 20 K - 300 K. Missions like GUSTO make use of non-linear mixing elements to achieve down-conversion of higher frequencies into IF bands. The mixers have a temperature dependent impedance that is difficult to measure. The last chapters of this work detail my attempt to

carry out in-situ vacuum cryogenic calibrations using industry standard commercial off-the-shelf calibration kits and cryogenic RF electro-mechanical latching switches. I present the complex impedance of a non-linear superconducting transmission line as measured with a cryogenic calibration.

DEDICATION

За мог покојног оца, мајку, и целу фамилију.

ACKNOWLEDGMENTS

I would like to start by thanking Sumner Starrfield who gave me my first opportunities in the field of astronomy. He was also instrumental in getting me into grad school in the first place, so none of this would be possible without his help and guidance. I also owe Mark Wagner a debt of gratitude for mentoring me in telescope operation, observation techniques, and data processing.

Thank you to Caleb Wheeler for being my friend and mentor, especially when I was an undergraduate. Thank you to Hamdi Mani who is easily responsible for several students succeeding in their Ph.D., and that is not an overstatement. A big thanks goes to Rebecca Dial for answering more than a few emails about the administrative process. I also want to list several of my colleagues from the lab group and beyond who were constantly a source of joy and support throughout. Sam Gordon, Genady Pilyavsky, Natalie Hinkel, Adrian Sinclair, Ryan Stephenson, Tom Mozdzen, Sean Bryan, Justin Mathewson, Jonathan Greenfield, Paul Horton, Cecilia La Place, Cassandra Whitton, Talia Saeid, Kyle Massingill, Emily Linden, Christina Bell, Daniel Lu, Ricardo Rodriguez, Madison Hedges, and Jeremy Meinke. People like you turn going to the lab from being a chore to being more of a reunion.

My advisor, Chris Groppi, I want to thank for the years of advice and financial support. You also gave me a tremendous amount of freedom to experiment and make mistakes on my own, and it proved invaluable. The lessons I learned from you let me grow into a researcher in my own way. You have shown many of us tremendous patience, and have always been willing to help no matter the cost. I especially want to thank you for the free beers. To my committee members I want to say I also appreciate your support, and wisdom.

A very special thank you to the people who pushed, and dragged me over the

finish line. Farzad Faramarzi, Sasha Sypkens, Jacob Glasby and Nani Glasby. You are each some of the hardest working and overall kindest people I know. These are not your only traits, just the ones I admire greatly. Farzad, and Sasha, you gave up a lot of your time to help me run instruments, and asked for nothing in return. The friendship and encouragement the four of you gave me through some of the hardest times in grad school I can never repay, and I will never forget.

TABLE OF CONTENTS

CHAPTER Page

LIST OF TABLES

Table Page

LIST OF FIGURES

Figure Page

Chapter 1

INTRODUCTION

1.1 Why study the ISM?

The underlying theme of my life for the better part of a decade has been the interstellar medium (ISM). The ISM is sometimes referred to as simply: "The dust and gas that make us up." It is then perhaps more appropriate to say the underlying theme of my entire life has been the ISM. In the following chapter I will introduce the key concepts of the ISM as we understand it. In this section I will discuss why it is important we study the medium, whilst refraining from (too much) further hyperbole. I will detail the components and different phases of the ISM, (section 1.2) as well as some of its intrinsic properties. I will also discuss the tools used by astronomers to observe the ISM in section 1.3, and in the following chapters I will present scientific results related to cutting edge research in the field (chapter 2). And lastly I will show novel work I have done to progress the technology used in ISM research, (chapter 3), and new techniques and methodology to improve measurement accuracy (chapter 4).

The interstellar medium is defined to be of all the matter and radiation between the stars within a galaxy. This includes a variety of components such as interstellar gas, and dust, magnetic, and gravitational fields, cosmic rays, electromagnetic radiation, and stellar winds. The vast majority of the matter, roughly 99% by mass, is in the form of dilute gas. To break it down further, $\sim 70\%$ of the gas mass in the ISM is hydrogen (H), in either atomic (HI), ionized (HII, or H+), or molecular

(H_2) form, and $\sim$ 28% helium (He), with 2% as heavier elements (Klessen and Glover 2015). The remaining 1% of material is not gas, but dust grains formed primarily by super novae (SNe) explosions, but also in stellar atmospheres and ejected into the ISM. These dust grains are small objects on the scale of microns (Draine 2010). What the dust is made of, remains unknown. Theories of the dust makeup include: silicates, polycyclic aromatic hydrocarbons, and iron, based on the observed emission/absorption profiles (Ryden and Pogge 2021).

The dust to gas ratio in the diffuse ISM is 1:100. Despite that large difference in composition the distribution of dust to gas is considered to be well mixed throughout the Milky Way. The gas component of the ISM can exist as different thermal phases, each with unique properties, and each phase is traced (or detected) from the emissions of specific atomic or molecular species. Since hydrogen is so abundant the phases are often categorized by the state of H in that region. The ISM phases will be detailed further in Section 1.2, but the big question to answer before that is: Why even study the ISM?

The shortest answer is that the physical and chemical processes that occur in the different phases of the ISM directly influence the makeup and evolution of galaxies. It is within galaxies that stellar nurseries form. This leads to stars, and subsequently to solar systems. The process of stellar evolution also returns matter and energy back in to the ISM through radiative feedback, stellar winds, and then more violent events like novae, and super novae explosions. That feedback can further drive star formation. Therefore understanding the dynamic process by which the medium changes is the key to understanding how galaxies like our own came to be, and how they may continue to evolve.

The order of events by which the ISM components evolve, otherwise known as

the life-cycle of the ISM, is also very important. That life cycle is described as a dynamic process, which begins and ends with turbulent, and violent stages, but also includes calmer segments. The life cycle is illustrated in Figure 1. This process begins with a warm gaseous phase. Shockwaves resulting from the death of large stars travel through the ISM collecting and compressing neutral HI, and ionized HII. The collected material clumps together and cools by radiating away energy. As regions cool and become denser, molecules can form. The clouds fragment into pockets of cool dense molecular clouds and star formation is initiated. Stellar winds and radiative transfer from the newly formed stars break up their parent clouds and give rise to further chemistry in the ISM. The larger stars $\gtrsim 8$ $M_\odot$ will go supernova and restart the process. This sequence of events also shows how the ISM is subdivided into smaller categories with different gas phases defined by the state of the local hydrogen.

1.2 Phases of the ISM

The life cycle of the ISM is pictured in Figure 1. This interpretation of the ISM life cycle comes from observations, and modeling. Early models of the ISM proposed a two-phase system in static equilibrium (Field, Goldsmith, and Habing 1969). One of the static equilibrium phase being a cold and dense collection of neutral hydrogen, and the second being a warm diffuse HI gas. Later a three-phase ISM model was introduced to account for the effects of supernovae (SNe) (McKee and Ostriker 1977). The third phase was an over-arching hot ionized medium energized by shockwaves. Warm ionized hydrogen gas and, molecular clouds are also important components.

They are sometimes referred to as the additional phases of the ISM in more recent work. Sections 1.2.1 - 1.2.5 give further details to these individual phases.

1.2.1 The Hot Ionized Medium (HIM)

The hot ionized medium, or sometimes called the hot inter-cloud medium is an expansive low density gas that hosts the other phases of the ISM. The HIM forms an extended atmosphere that rests above and below the galactic plane and fills the void between ISM components commonly being referred to as a coronal gas. The HIM is the first part of the three-phase model that is in relative thermal and pressure balance with the warm neutral medium, and the third phase being the cold neutral medium. The HIM is energized by SNe shockwaves. The temperature of the HIM is $T \gtrsim 10^{5.5}$ K, with a number density of $n \sim 0.004$ atoms cm^{-3} (Draine 2010). The volume filling factor $f_V = 0.5$ or in other words taking up 50% of the volume in the galactic disk, though the accuracy of f_V remains contested for each of the phases (Tielens 2005).

1.2.2 The Warm Ionized Medium (WIM)

The warm ionized medium is made up of a diffuse gas with a density $\gtrsim 0.2$ cm^{-3}, and a temperature on the scale of $T = 10^4$, $f_V = 0.1$ (Draine 2010; Ryden and Pogge 2021). The gas is ionized by O and B type stars emitting extreme ultra violet (EUV) and soft x-ray photons with energies between the ionization potential for hydrogen 13.6 eV and 100 eV. These stars formed in the denser regions and disrupted their parent cloud allowing the excess radiation to ionize H. As such, photodissociation

regions (PDRs) are typically found in this phase (Walker 2015b). The PDR are zones where far-ultraviolet (FUV) photons break apart, or disassociate, molecules. They can also be seen wherever FUV photons have a dominant interaction with gas clouds (Tielens 2005).

1.2.3 Warm Neutral Medium (WNM)

The neutral atomic gas in the ISM can be found in two parts. One is the warm neutral medium (WNM), an area where HI is the primary tracer, but temperatures are higher than in certain cool neutral regions, with T $\sim$ 8000 K. The WNM can be seen in areas near the WIM and in PDRs, it has hydrogen number density of n $\sim$ 0.5 cm^{-3}, $f_V = 0.3$ (Tielens 2005; Ryden and Pogge 2021).

1.2.4 The Cold Neutral Medium (CNM)

The cold neutral medium is the second form of atomic gas in the ISM. The temperature ranges from 80 - 100 K, and the density is believed to be between 20 cm^{-3} to 50 cm^{-3} (Ryden and Pogge 2021). The volume filling factor $f_V = 0.01$. The primary heating mechanism for the CNM is thermal energy transfer from collisions of dust grains with neutral gas. The dust grains themselves are heated by far infrared (FIR) radiation. The primary cooling mechanism is HI fine structure 21-cm line emission. Consequently this makes for a good direct detection method and diagnostic of the CNM. Parts of the CNM can become dense enough to form molecular clouds. The CNM and WNM/WIM were linked together by the two-phase model which predicted, for a set of pressures there could be two thermally stable

gas phases in the ISM, one dense and cool (CNM), the other diffuse and warm (WIM/WNM). Supernovae were proposed to regulate the pressure through the HIM which the other components inhabit and evolve from.

1.2.5 Giant Molecular Clouds (GMCs)

Supernova explosions occur roughly once every fifty years in the Milky Way. The resulting expulsion of stellar material sweeps up ISM material. Over time their shock fronts can overlap. Giant molecular clouds, as the name implies, are massive regions of molecular gas and dust. They are formed by constructively interfering supernova shockwaves and have between 10^3 and 10^7 solar masses of material within them (Walker 2015b). GMCs have further pockets that will condense to form cold dense molecular clouds (CDMs) which are an important component of the ISM because it is only here that star formation can occur. A molecular cloud will form in denser parts of the CNM. CDMs are characterised by H_2. The clouds have a temperature range of 10 K to 50 K, and densities from 10^3 cm^{-3} to 10^6 cm^{-3} (Walker 2015b; Ryden and Pogge 2021).

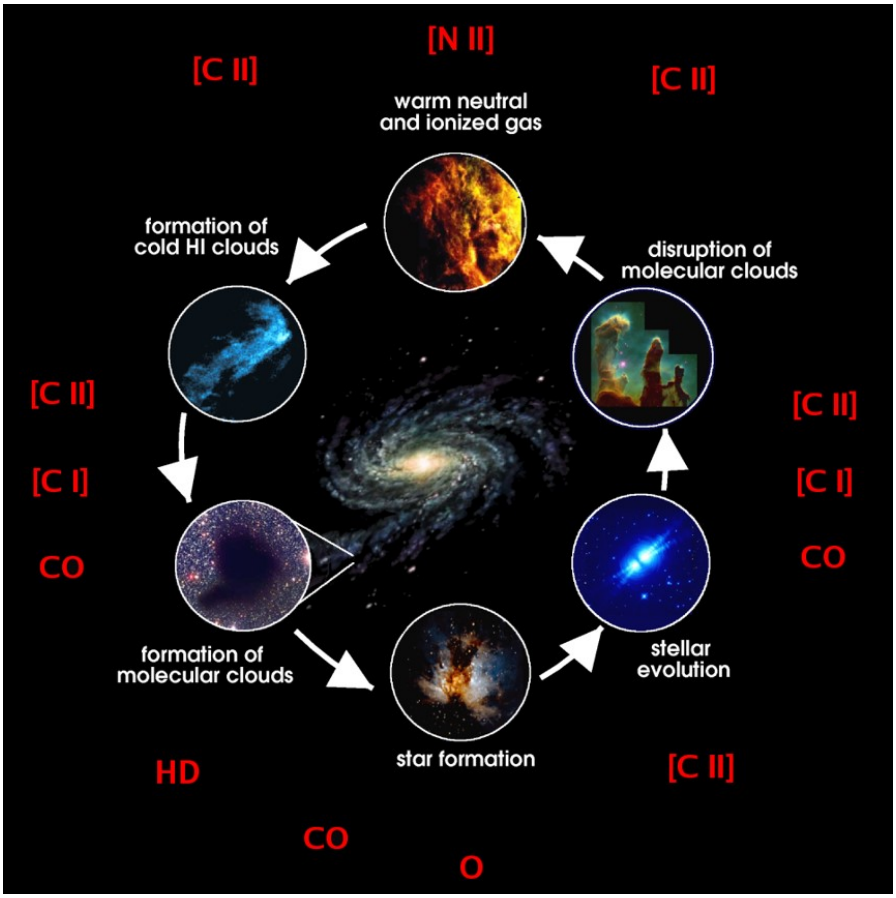

Figure 1. The Life-Cycle of the Interstellar Medium.

Source: Groppi et al. (2006)

Note: Here are shown several key steps in the life cycle of the ISM, and the most notable tracers of each step. This figure illustrates how overlapping supernovae shock waves sweep warm atomic material into denser clouds. The clouds condense and cool, and go on to form heavier molecules before fragmenting further and forming giant molecular clouds. The molecular clouds evolve into stellar nurseries that are broken apart through the process of stellar evolution which in turn dissipates the raw material of the cloud back into the diffuse ISM. The cycle restarts when the larger stars go supernova. The most common tracers of each phase are denoted in red. The diagram was originally made by Craig Kulesa, and has become a staple of any ISM presentation since circa 2006.

1.3 Tools for Studying the ISM

Characterization of the ISM is accomplished by observing galaxies in several different wavelength regimes. This is because the different phases of the ISM emit different wavelengths of light as they cool. These emission lines are the best diagnostic tools, but can be orders of magnitude different in scale, and therefore require their own dedicated and often incompatible observation platforms. To probe the structure of neutral atomic gas for example, one can use the fine structure transition of a neutral hydrogen atom. The lowest energy configuration for a neutral hydrogen atom is when the spin state of the nucleus is opposite, or anti-parallel, to the spin state of the electron. H can still exist in its ground state when the spins are parallel. This is called line splitting or degeneracy of a state. If the spin of the electron goes from parallel with the nucleus to anti-parallel, it emits a radio signal. The sheer abundance of H in the galactic plane makes an ever present stream of photons from this transition. The photons have a wavelength of 21-cm or a frequency of 1.42 GHz. 21-cm radio astronomy is its own field of research.

Molecular hydrogen is not a polar molecule and cannot be directly detected for the bulk of the ISM due to the low average temperatures where it is found. Most of the molecular hydrogen is formed in cold 10 - 100 K clouds, but the lowest temperature rotational transition for H_2 is T $\sim$ 500 K. To more effectively trace molecular clouds, other prominent material, namely carbon, nitrogen and oxygen must be used. These are the next most abundant atoms in the ISM. Multiple isotopologues of carbon monoxide (CO) will form along H_2 in denser regions. The isotopologues are chemical compositions where one or more components are isotopes. CO has a rotational transition J = 1 $\rightarrow$ 0 which is historically used to probe

molecular gas. The main isotopologue of CO used in this work is ^{12}CO which has a rotational emission of 2.61 mm or 115 GHz. This however does not give a full picture of the molecular clouds of the ISM. Grenier, Casandjian, and Terrier (2005) showed that there existed cold clouds invisible to CO or HI, but visible in gamma rays generated by cosmic-ray interactions in the neighboring gas. The molecular component where CO is below detection limits or carbon is heavily ionized are known as CO-dark clouds (Wolfire, Hollenbach, and McKee 2010). This is partly because H has a higher ionization potential of 13.6 electron-volts (eV) compared to C which is 11.6 eV and can still be neutral when C is not. So singly ionized carbon, [CII] is an excellent tracer for the rarely observed H-H_2 transition clouds of the ISM (Pineda et al. 2017). Radio continuum emission from dust grains can provide further details about both molecular and neutral hydrogen even where CO is dark. These maps however, will often contain more emission along the line of sight that his not related to the cloud being observed as they lack the spectral resolution to de-couple background emission in three dimensions.

1.3.1 THz Astronomy

Not only is [CII] an important diagnostic tool for molecular clouds, and crucial to tracing CO-dark gas, but it is also prominent throughout the ISM phases. As shown in Fig. 1 the most common and brightest emission line for most of the ISM life-cycle is [CII] which can even outshine HI. Several studies have already been conducted to collect data of our galaxy at these higher frequencies, and future missions are currently being planned to survey similar underrepresented emission lines. Observations of lines like [CII] which emits at 1.89 Terahertz (THz or 10^{12}Hz)

frequency, and [NII] (1.46 THz) are lacking because they fall into what is known as the terahertz gap. This is a window of electromagnetic radiation from 0.10 THz to 10.0 THz where observations are between microwave, and infrared wavelengths. Until recently, technology did not exist to make lab sources at these frequencies and as a result, observations in the THz regime have been limited or cost prohibitive.

For the case of line emission, the emitted radiation from THz sources are too high frequency to be processed by normal readout electronics and thus require some form of down conversion. One method for down conversion is heterodyne mixing which is well covered by Wheeler (2016). The term heterodyne refers to the fact that signals are of different power before mixing. In a heterodyne system an incident beam is convolved with a local (lab) source, and from the properties of non-linearity the resulting signal will consist of beat-frequencies. The response is filtered so that only frequencies which are the difference between incident sky beams, and local oscillator (LO) frequencies are collected. This creates an intermediate band that can be processed by modern electronics. The non-linearity of a device arises for several reasons based on material or construction, but what it means is that the object depart from the expected linear relation of current and voltage V = IZ, known as Ohm's law. Most electronic devices are non-linear, with two main types of non-linear devices used in modern THz astronomy are the superconductor-insulator-superconductor (SIS) mixer (Zmuidzinas and Richards 2004), and the hot electron bolometer (HEB) mixer (Gousev et al. 1994). HEB mixers like ones made from niobium nitride NbN can achieve higher frequencies than typical SIS making them more viable above 1 THz. A NbN HEB mixer (Khosropanah et al. 2007) will be the focus of section 4.1.

To make matters more complicated, the Earth's atmosphere is a good absorber

of radiation in THz frequencies. Observations must be carried out at high altitude or if possible in space. A good example of a THz space mission is the European Space Agency's Herschel Space Observatory 3.5 m telescope, with the heterodyne instrument for the far infrared (HIFI) (Pilbratt et al. 2010; Roelfsema et al. 2012). High altitude missions can be accomplished by balloon payloads or aircraft. A high altitude aircraft example is the stratospheric observatory for infrared astronomy (SOFIA) which was a 2.5 m telescope aboard a Boeing aircraft that could operate up to 45,000 ft and took measurements between 0.3 and 1600 μm (Erickson 1995; Casey 2004). Previous THz balloon missions include the stratospheric terahertz observatory (flight 1 and flight 2) (Walker et al. 2010). Future balloon examples like the galactic/extra-galactic ultra-long duration balloon spectroscopic terahertz observatory (GUSTO) (Walker, Kulesa, and Goldsmith 2020) will observe THz lines including [NII] 205 micron emission and [CII] 158 micron line with a 0.9 m aperture telescope to survey the galactic plane. Details about GUSTO are further discussed in section 1.4. One up-coming mission in particular: the astrophysics stratospheric telescope for high spectral resolution observations (ASTHROS) will observe multiple lines of [NII], for curated targets exhibiting signs of various ISM phases, with a 2.5 m telescope (Siles et al. 2020). I will discuss the ASTHROS mission in section 1.5.

1.4 GUSTO Mission Background

GUSTO is a NASA Explorer Mission of Opportunity regulated as a Class-D space mission that will use state of the art THz technology to probe the ISM by mapping part of the Milky Way for about 100 square degrees, and Large Magellanic Clouds (LMC) for 24 square degrees (Walker 2015b). GUSTO will be looking for the fine

structure transitions [CII], [OI], and [NII]. These are some of the brightest cooling emission lines in the galaxy. They are able to penetrate dense regions of the ISM that are opaque to other frequencies. The transitions [CII], [OI], and [NII] correspond to wavelengths of 158 μm (1.89 THz), 63 μm (4.75 THz), and 205 μm (1.46 THz) respectively. The high frequencies involved require high altitude measurements. GUSTO will be launched from Antarctica, and is planned to be airborne for a period of about 100 days. The operating flight altitude of the mission will be 33 km, where it will be above the THz interference of Earth's atmosphere. Because these lines fall in the THz gap, heterodyne techniques must be used. GUSTO will have three 8 pixel heterodyne arrays, one for each target band.

The science objects for GUSTO can be broken down into five main parts. The first goal is to determine the life cycle of interstellar gas in our Galaxy. The high spectral and spatial resolution of the GUSTO hetorodyne arrays make this task possible. GUSTO will survey the Milky Way in regions where star formation is occurring to look for signal of the above mentioned lines and identify clouds of interest. Emission spectra of [CII] can help measure the mass and position of clouds, and the combined measurements of other atomic species can help separate the warm and cold components of the ISM. For example detection of [CII] that coincide with HI emission can be a good diagnostic of the CNM spatial distribution, density, and pressure. Likewise [NII] is a good diagnostic for the WNM as seen in Figure 1 and can help distinguish if the surrounding gas is ionized.

The second goal is to witness destruction and formation of star forming giant molecular clouds clouds. This particular goal is very important because there are no direct observations of GMC formation to date. GUSTO would have the ability to validate existing theories of GMC formation or indicate new possible explanations for

the process. This survey aims to highlight all of the molecular hydrogen observable in its scan path and catalogue them where CO and HI surveys may have missed. The molecular clouds observed in this way would be in various stages of their evolution. By observing numerous clouds, their location within the galaxy, and their structure, that data can be compared and associated with relevant theories to identify which yield the best predictions. This will also provide maps of material dispersed by destruction of the molecular clouds and how they effect star formation rates.

The third goal is to understand the dynamics and gas flow into and within the galactic center. The center of the galaxy has an immense amount of molecular gas with $\sim 4 \times 10^7$ $M_\odot$ (Dahmen et al. 1997). This region has been studied in far infrared lines before, but not at sufficient angular resolution. This mission will enhance previous studies with improved accuracy and allow comparison to models of mass flow of the galactic center.

The fourth goal is to improve the understanding of the Large Magellanic Cloud (LMC). More precisely GUSTO aims to investigate the exchange between star formation, stellar winds, radiation, and how the local ISM in the LMC is structured. What makes the LMC interesting is that it is a lower metallicity galaxy. Here the metallicity (Z) is the amount of elements heavier than H and He not only in the ISM but in stars as well. Heavier elements are formed in stars and expelled and distributed back into their surrounding environments. So as time goes on the ISM is enriched and the next generation of stars will have an increased Z. Detailed studies of the LMC can provide insight into the earlier environment of our own galaxy.

The final goal is to construct Milky Way and LMC templates for comparison to distant galaxies. This objective is straightforward. By observing a large portion of our own Galaxy as well as the lower mass and lower metallicity LMC, the lessons

learned can directly influence future missions. The scope of the survey will provide characteristic ISM observations at different pressures, and other physical conditions, that can help interpret data of the ISM in other distant galaxies.

The large areas covered by this survey require increased pixel count, up from a single pixel array scheme to eight. It also needed a longer flight duration platform. Both of these requirements can be impacted by the method of signal transport. The physical space taken up by transmission lines, and the way they are routed directly limit the number of pixels per array. The heat load transferred into the instrument by the transmission lines can also change how much time a mission may fly for due to limited coolant. A specialized intermediate frequency (IF) harness needed to be designed and fabricated to exact specifications in order to carry the signals after the heterodyne process and address these issues. In this dissertation I show the results of hardware design and testing for the custom built GUSTO IF system which was my contribution to the project. The harness will be discussed in section 3.3.

1.5 ASTHROS Mission Background

ASTHROS is another balloon-borne payload. It will have a 2.5 m telescope, whose mission will be to observe fine structure lines of [NII] in regions of ionized gas. The ratio of intensity between the 122 μm and 205 μm lines yields the electron density of the observed gas (Goldsmith et al. 2015). The mission will use a 4-pixel heterodyne array. The spectral resolution varies with the source observed, for example the Carina Nebula will see a 3 kms^{-1} resolution. The high spectral resolution of ASTHROS will allow it to map the physical distribution of the gas in three dimensions. Nitrogen is a superior probe of ionized gas, because it has

an ionization potential of 14.5 eV which is higher compared to that of H at 13.6 eV. Hydrogen being at a lower ionization potential and greater abundance means wherever [NII] is detected there is a sufficient energy from bright stars to ionize not only H but heavier elements. Signal from [NII] is not absorbed by dust so it is less impacted than other IR sources. ASTHROS is scheduled to launch from Antarctica in December 2024 for a 21 day mission at roughly 40 km altitude. The mission will image specific sources in the Milky Way, and the M83 galaxy. The observation strategy seeks to highlight sources believed to be in distinct stages of their evolution.

There are three main science goals for ASTHROS with the first being to complete the picture of the density and dynamical structure of the ionized components of the ISM. Light from massive stars ionizes the surrounding gas especially in stellar nurseries where new stars are formed. The structure of the ionized gas component and the spatial distribution are directly influenced by the stars formed inside of them. ASTHROS will probe the traces of ionized gas that will lead to three dimensional maps of the observed regions. The structure is ultimately influenced by the dynamical feedback systems in the ISM which leads in to the next goal.

The second goal is to determine the key mechanisms and influences of stellar feedback on the ISM. This feedback regulates ongoing star formation which is considered an inefficient process due to the fact that only a small amount of the ISM is converted to stars. The forming of stars is one of the main drivers in galaxy evolution so studying the feedback of stellar material from the end of stars back to the ISM helps build on that understanding. That feedback is usually in the form of stellar winds, and super novae events. From the [NII] emission studies, the resulting maps will have kinematic information on the ionized regions.

The third goal is to determine the physical conditions of ionized gas found in

extra-galactic sources. One of the key targets of the ASTHROS mission will be the entire galactic disk of the M83 galaxy. This is the first time the entire barred-spiral galaxy will be observed in these lines.

Another source to be observed is the Carina nebula, which I have investigated using initial ancillary data. The benefit to looking into this source in existing studies is that even at lower frequencies there is information to be gleaned. Studies of the nebula in CO and dust continuum can show how much of the nebula is in the form of molecular hydrogen that is CO-dark. Since ASTHROS is operating at THz frequencies, and the LO technology exists to fine tune channels, [CII] observations are possible. The analysis in chapter 2.1 highlights the need for more observations in [CII].

Chapter 2

ANCILLARY DATA AND ANALYSIS FOR ASTHROS

2.1 The Carina Nebula

The Carina Nebula also known by the new general catalogue designation NGC 3372, or referred to as the Carina Nebula Complex (CNC), is a very active star forming region in the Milky Way. The benefit to studying Carina in depth is that the nebula is early enough into its evolution that it still produces new stars, but already progressed enough that older stars have gone supernova. Since it is such an active star forming region, and the process of stellar evolution is providing feedback into the parent system it serves as a great template for several steps in the ISM life cycle. Carina is a molecular transition cloud located at RA = $10^{\rm h}45^{\rm m}02^{\rm s}.23$, Dec = $-59°41'59.8''$ (J2000) at a dist of $\sim$ 2600 pc (Kuhn et al. 2019). It is home to $>$ 60 O type stars including one of the most luminous known stars in the galaxy η Car (Smith 2006).

Small scale maps of Carina in [CII] from STO-2 (Seo et al. 2019) and SOFIA (Young et al. 2012), as well as a larger scale [NII] map (Oberst 2009) exist but broader surveys of those lines will be the objective of future studies. In this work I look at Carina in emission lines of HI, ^{12}CO, ^{13}CO, and C^{18}O. I am presenting estimated maps of hydrogen column density N(H + H_2) and for the first time, a molecular fractional map f(H_2) showing its spatial distribution using dust continuum maps. In this chapter I will compare that molecular fraction to predictions based on models. From radio continuum maps I estimate the gas mass in the form of ionized

hydrogen. Multiple CO lines were used to designate regions as diffuse atomic cloud or dense molecular cloud as well as demonstrate how much of the nebula exists as molecular hydrogen without observable CO. An independent estimate of the CO-dark molecular hydrogen column density traced from a dust continuum map would allow one to use [CII] emission to determine the thermal pressure distribution of gas in the those regions.

2.2 CO-Dark Gas

Gamma ray observations of the ISM molecular component show that H_2 clouds can form with little to no CO present, by tracing an excess of gas not seen in either CO or HI (Grenier, Casandjian, and Terrier 2005). This may be due in part to the fact that CO is photo-dissociated in PDRs and the carbon atoms either remain neutral or, more often, become ionized C^+ while H is able to shield itself and continue to form H_2 (Hollenbach and Tielens 1997). Theoretical models predict that a high column density of hydrogen or dust (in higher metallicity zones) would protect the inner layers of a cloud from UV radiation (Busch et al. 2019). The result would be an optically thick gas layer at the surface of H_2 which is better protected than C, and forcing CO formation to occur later and deeper in the cloud (Madden et al. 2020; Wolfire, Hollenbach, and McKee 2010). Models and observations explain that the excess C would be primarily in the form of C^+ that is emitting mainly in [CII] at 158 μm wavelengths in an envelope surrounding CO cores. Dust continuum measurements can prove useful at uncovering CO-dark gas, but they are derived from modelling and require assumptions like dust-to-gas ratios which can have large uncertainty (Madden et al. 2020). Molecular clouds are already of interest because

they are a precursor to star formation. The same conditions, i.e. the density, and self shielding required for H_2 to stably form are thought to be the same conditions that lead to star formation. The effectiveness of CO to trace H_2 varies sharply with metallicity (Chevance et al. 2020). Thus CO not only underestimates the molecular component of the Milky Way but of other galaxies which have poorer metallicity regardless of other evidence of star formation. It is also worth mentioning that the conversion factor that relates CO to H_2 column density is also considered to be a rough estimate, which adds to CO being a less efficient tracer than previously thought. Galactic modeling places the gas mass of the CO-dark region at $\sim 30\%$ for the MW (Wolfire, Hollenbach, and McKee 2010). These reasons motivate the need for further THz surveys of the molecular ISM. Since ASTHROS is concerned with structure and distribution of the molecular clouds, it cannot rely on CO observations alone to identify regions of interest, especially for lower metallicity targets. The astronomical source I collected the most ancillary data for was Carina, and this included dust continuum and CO maps. In the following sections I demonstrate how the CO emission fails to constrain the total molecular gas mass, and that the amount of excess dark gas falls in line with estimates for the Milky Way.

2.3 Data

The following sections detail where the original CO (section 2.3.1), HI (sec 2.3.2), dust continuum (sec 2.3.3), and radio continuum (sec 2.3.4) data were obtained. There is also information on initial data processing.

2.3.1 Mopra CO Data

The CO data I used comes from the Mopra Southern Galactic Plane CO Survey from the 22-m single dish radio telescope Mopra at the Australia telescope national facility (Burton et al. 2013; Braiding et al. 2015; Braiding et al. 2018). The survey mapped several CO lines including ^{12}CO, ^{13}CO, and C^{18}O for approximately 250 square degrees of the Southern Galactic Plane. The region covering the Carina Nebula, which is the focus of this work, includes published observations detailed in Rebolledo et al. (2016), and unpublished observations that will be presented in Cubek et al. (2023).

The specific survey FITS data cubes presented in this work were the J=1 $\rightarrow$ 0 transitions of ^{12}CO, ^{13}CO, and C^{18}O which correspond to frequencies of 115 GHz, 110 GHz, 109 GHz respectively. The data cubes for all three lines covered a spatial region in galactic longitude (l): 285.0 $\lesssim$ l $\lesssim$ 290.0 degrees, and galactic latitude (b): -1.49 $\lesssim$ b $\lesssim$ 1.51 degrees. The line of sight axis for the CO spectral cubes had units of velocity corrected for the local standard of rest V_{LSR}. This may seem strange because the other two dimensions of our cube are positions in latitude and longitude, so why then is the third axis velocity? The telescope is measuring frequency signals from sources moving away and towards us. The measured frequency of the atomic species is then different from the rest or laboratory frame. The difference is known as the Doppler shift: $\Delta\nu = \nu_0\ \Delta$v c^{-1}. The difference between the measured frequency ν and the rest frequency ν_0 is equal to the difference in velocity between observer and object Δv, and inversely proportional to the speed of light c. The velocity and rotation of our galaxy are well studied and the velocity of an object relative to our solar system tells us where in the galaxy that object is. The mean velocity of our

solar system within the Milky Way is known as the local standard of rest (LSR). It is for those reasons that we solve the Doppler shift equation for Δv relative to LSR.

Spectral velocity coverage was -645 $\lesssim$ V_{LSR} $\lesssim$ 664 kms^{-1} for ^{12}CO, -579 $\lesssim$ V_{LSR} $\lesssim$ 315 kms^{-1} for ^{13}CO, and -589 $\lesssim$ V_{LSR} $\lesssim$ 305 kms^{-1} for C^{18}O. The effective spatial resolution of the instrument was $\sim$ 36 arcseconds ($''$), and spectral resolution of the original images was 0.1 kms^{-1} . The processed images used in this work had spectral resolution of 1 kms^{-1} . The data cubes were in units of antenna temperature T_A (K). The antenna temperature is a misleading name. It does not imply the physical temperature of the antenna or the actual temperature of the emitting source. It is instead defined as the theoretical temperature a perfect black body would have for the equivalent power per unit frequency (P_ν) as the antenna is receiving from the source: $T = P_\nu\ k^{-1}$. Here k is Boltzmann's constant. Some of that theoretical power is lost due to an efficiency factor of the telescope η_{mb}, so the corrected value is called the main beam temperature. The main beam efficiency for this data set was $\eta_{\rm mb}$ = 0.55. Using the equation $T_A = \eta_{\rm mb} T_{\rm mb}$, I converted all Mopra cubes to main beam temperature ($T_{\rm mb}$). An integrated intensity map of CO with V_{LSR} ranging from -30 to +30 kms^{-1} before subtracting the background noise can be seen in Figure 2. Figure 3 shows the same image with only pixels above 3σ (or three times the standard deviation of background noise) visible after the masking, and background subtraction which will be further discussed in section 2.4.2. The integrated intensity map is a sum of all of intensity along the line of sight as discussed in section 2.4.1. This is also called the moment map. The rms noise per channel for the ^{12}CO data was $\sim$ 1.2 K, and for the rest was $\sim$ 0.5 K (Braiding et al. 2015).

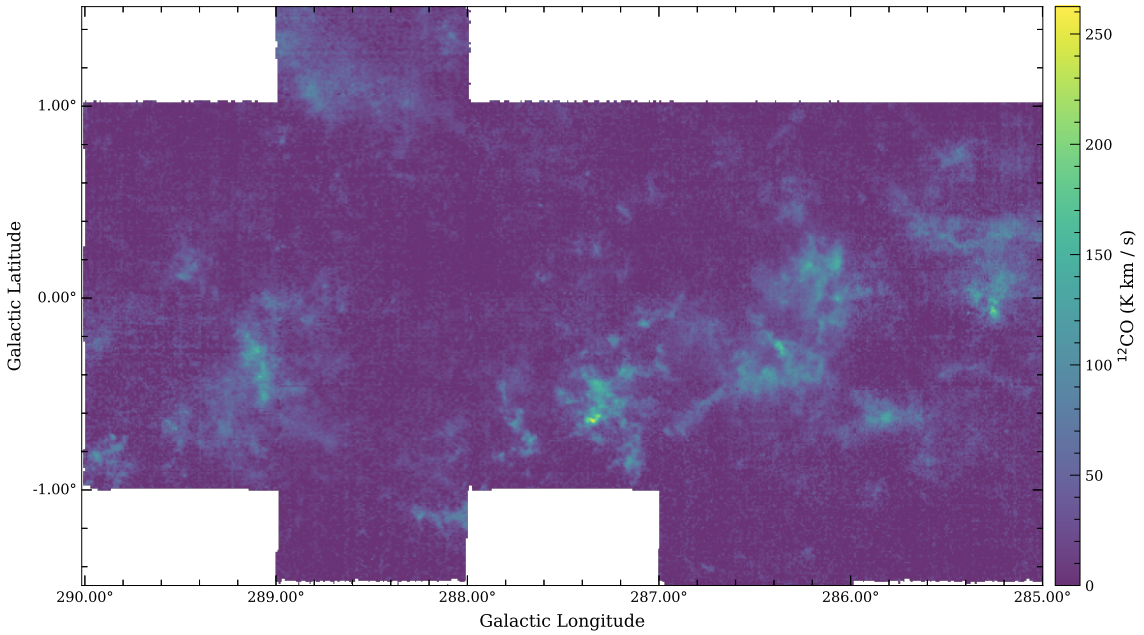

Figure 2. ^{12}CO Before Subtraction

Note: A raw moment map of integrated intensity with velocity (in local standard of rest) from -30 kms^{-1} to +30 kms^{-1}. This image shows the original boundary of the data. It also includes all of the background signal that is not coming from the Carina Nebula Complex. A second image containing a slice of ^{12}CO from 287 to 288 degrees galactic longitude was stitched in from the same survey. Fig. 3 was created using a dilated mask (see Sec 2.4.2)

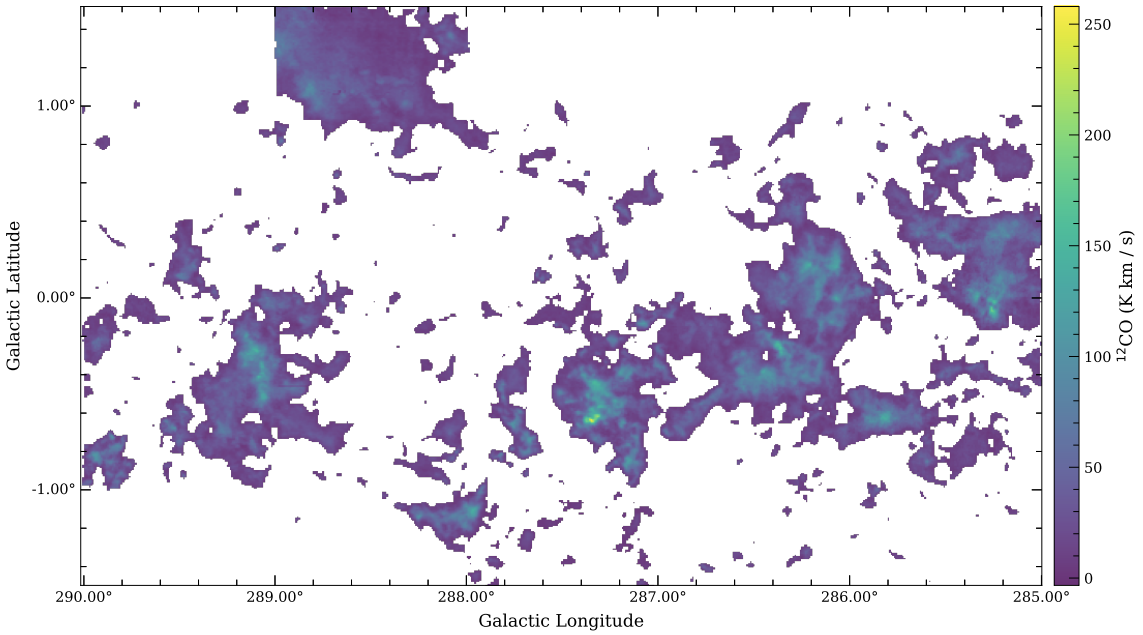

Figure 3. Integrated Intensity Map of $I_{^{12}CO}$

Note: Integrated intensity map (moment 0) of ^{12}CO emission data with full spatial coverage and spectral coverage from -30 $\lesssim V_{LSR} \lesssim$ +30 kms^{-1}. The noise σ = 2.8 K kms^{-1} was calculated by applying a dilated mask as detailed in 2.4.2. The dilated mask had smoothing factors for the spatial component 3X and 5X for spectral. Units are in K km s^{-1}.

2.3.2 ATCA HI Data

Neutral atomic hydrogen in the ISM is best traced by the HI 21-cm line (1420 MHz). I made use of HI map data for Carina first presented in Rebolledo et al. (2017). These highly detailed maps of the Carina nebula and neighboring complexes were made from observations conducted at the Australia Telescope Compact Array (ATCA). ATCA is an astronomical interferometer which uses several separate telescopes in an array to achieve a higher angular resolution than any one of the systems can achieve alone. The spacing between interferometer telescopes is known as the baseline. At higher angular resolution the baseline is also long and the array loses sensitivity to detect emissions for extended sources because of a lack of shorter baseline observations. This is known as the short spacing problem. Single dish measurements are used to compliment array measurements by setting the zero point and scaling of the interferometric map. This data was calibrated using single dish observations from the Parkes telescope to correct for the short spacing. Spatial coverage for the 21-cm Carina map included the galactic l, and b regions: $285.8 \lesssim l \lesssim 289.0$ degrees, and $-3.00 \lesssim b \lesssim 1.00$ degrees. The spectral coverage ranged is $-55.50 \lesssim V_{LSR} \lesssim 144.57$. The spatial resolution for the HI data was $\sim 35''$ and the spectral resolution was 0.5 kms^{-1} . The HI 21-cm emission line data was truncated to match the CO data. The noise sensitivity per channel of the HI data was 8 K.

2.3.3 Herschel Dust Continuum Data

Molecular hydrogen gas column density was derived by Rebolledo et al. (2016) using dust continuum emission images taken as part of the Herschel Infrared Galactic

Plane Survey (Hi-GAL) (Molinari et al. 2010). The PACS and SPIRE instruments were used during this survey to take data spanning the wavelengths 70, 160, 250, 350, and 500 μm. These images are available on the Herschel science archive. Rebolledo et al. (2016) used spectral energy distribution to fit the infrared data points to a modified black body curve. The authors could then fit temperature and mass density of the nebula. Mass density was converted to a column density assuming the dust emission came entirely from molecular hydrogen. Dust emission can trace both atomic and molecular hydrogen depending on the physical conditions in the nebula. For the purpose of this work I adopted the same assumption (dust was tracing only molecular hydrogen) and believe it to be valid considering that lower temperature dust will be traced by IR emission and the observed temperatures are associated with molecular clouds, while diffuse gas is at much higher temperature. If I were however, to treat the dust map as total column density N(H + H_2) which included emission from diffuse atomic hydrogen I would be able to predict the resulting N_{H_2} map using HI data. I will show that this approach resulted in a large over-subtraction of molecular hydrogen which further supports the assumption of entirely molecular dust emission. This approach is detailed in Section 2.4.3. The N_{H_2} map derived from dust has a $\sigma = 1.3 \times 10^{21}$ cm^{-2} and resolution $\sim 36''$ (Rebolledo et al. 2016). Fig. 4 shows the molecular hydrogen from dust continuum map with units particles per cm^{-2}.

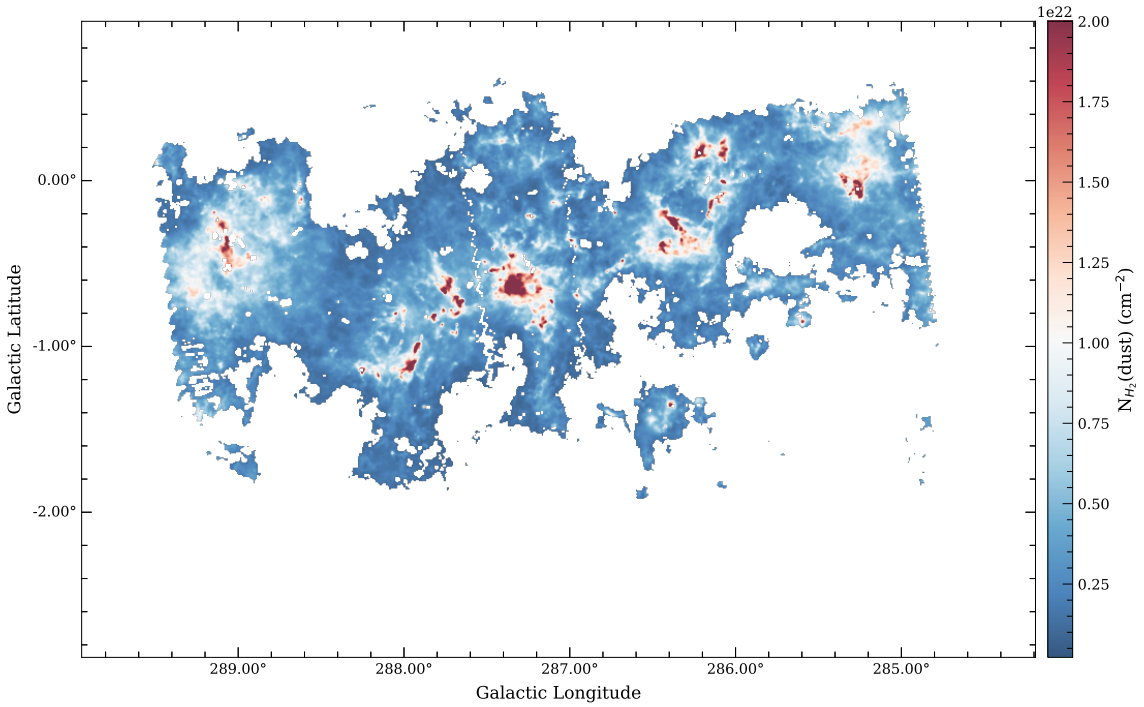

Figure 4. Molecular Hydrogen Column Density

Note: Map of N_{H_2}(Dust) derived using SED fitting of dust continuum images from $\lambda = 70$ - 500 μm from Rebolledo et al. (2016). The $\sigma_{\rm rms} \sim 10^{21}$ cm^{-2} and only pixels above 3σ are shown.

2.3.4 Radio Continuum Data

To complete the picture of the total hydrogen mass budget in the Carina Nebula, I used images of ionized hydrogen traced by 1-3 GHz maps of the radio continuum from (Rebolledo et al. 2021). In heavily ionized regions the gas behaves like a plasma with a high density of ions to recombine with electrons that result in a continuous radio emission. This data was obtained at the ATCA along with HI and other bands as a part of a broader study into Carina and the nearby Gum 31 Complex. The coverage was from $285.5\,' \lesssim l\,' \lesssim 289.1$ degrees, and $-3.20\,' \lesssim b\,' \lesssim 1.14$ degrees. The units were in Jansky (Jy) beam^{-1}, with a beam resolution of $24.4'' \times 15.8''$, and $\sigma = 2$mJy beam^{-1}. A Jansky is a commonly used unit in astronomy where 1 Jy = 10^{-26} Wm^{-2}Hz^{-1}. Table 1 contains a list of all data used, and some helpful parameters.

Table 1. Ancillary Data for Carina

Line	λ (m)	ν (Hz)	Instr.	Resolution
^{12}CO	2.61E-3	115E9	MOPRA	$36''$
^{13}CO	2.72E-3	110E9	MOPRA	$36''$
HI	2.1E-1	1.42E9	ATCA	$\sim 35''$
Dust	(70-500)E-6	(4.20-0.60)E12	Herschel	$\sim 36''$
H+	(8-70)E-6	(1-3)E9	ATCA	$\sim 16''$

Note: List of all the data used to make images and do analysis of the Carina nebula. CO, HI, and H+ data were stored in 3D position-position-velocity FITS data cubes. The dust map was a 2D FITS image.

2.4 Preparing Ancillary Data

The data files were processed from their raw form to a reduced image that removes errors or artifacts based on the observing telescope, and weather conditions. In order to do comparisons between the data sets required further preparation. All data analysis was done using standard python routines, the spectral cube sub package, and the astropy library. I wrote scripts to convert 3D data sets to 2D images, scripts to change resolution to a common value, re-scale, and reshape the data to a common grid in the following section 2.4.1. Special steps in the masking of the CO data is explained in section 2.4.2. The final column density maps are discussed in section 2.4.3.

2.4.1 Integrated Intensity Maps and Image Rescaling

All files were stored in the standard FITS format with the HI and CO data being FITS data cubes with spectral units of K. The first step toward converting the 3D spectral cubes to 2D column density maps was to create integrated intensity maps. This was done by integrating intensity values over an entire spectral line for specific velocities also known as a zeroth moment map:

$$M_0 = \int I_\nu d\nu \tag{2.1}$$

The data cubes spanned as wide a velocity range as 1300 kms^{-1} and contained extraneous information in the form of background clouds. I identified the velocity range of the Carina nebula from the averaged spectrum as in Figure 5. For CO the main peak was contained within -30 $\lesssim$ $\mathrm{V_{LSR}}$ $\lesssim$ -10 kms^{-1} which is the approximate

velocity range of the Carina nebula (Schneider et al. 2015). The secondary peak in CO emission from -10 $\lesssim V_{LSR} \lesssim$ +30 kms^{-1} comes from clouds not associated with the overall CNC. Since the column density maps of molecular hydrogen were estimated from IR emission, which contain data from everything along the line of sight, it was impossible to decouple the secondary emission peak from the IR data. I extended the final CO velocity range to -30 $\lesssim V_{LSR} \lesssim$ +30 kms^{-1} because this was the region that will have contributed to the N_{H_2}(dust) estimate. This velocity range also removed excess channels in CO and HI that are noise. Figure 3 shows the ^{12}CO integrated intensity map for this velocity range in units of K kms^{-1} . The map has also had all pixels below $\sim 3\sigma$ removed. The masking process is further discussed in 2.4.2. The full spatial coverage was preserved. The same process was repeated for ^{13}CO and C^{18}O data cubes.

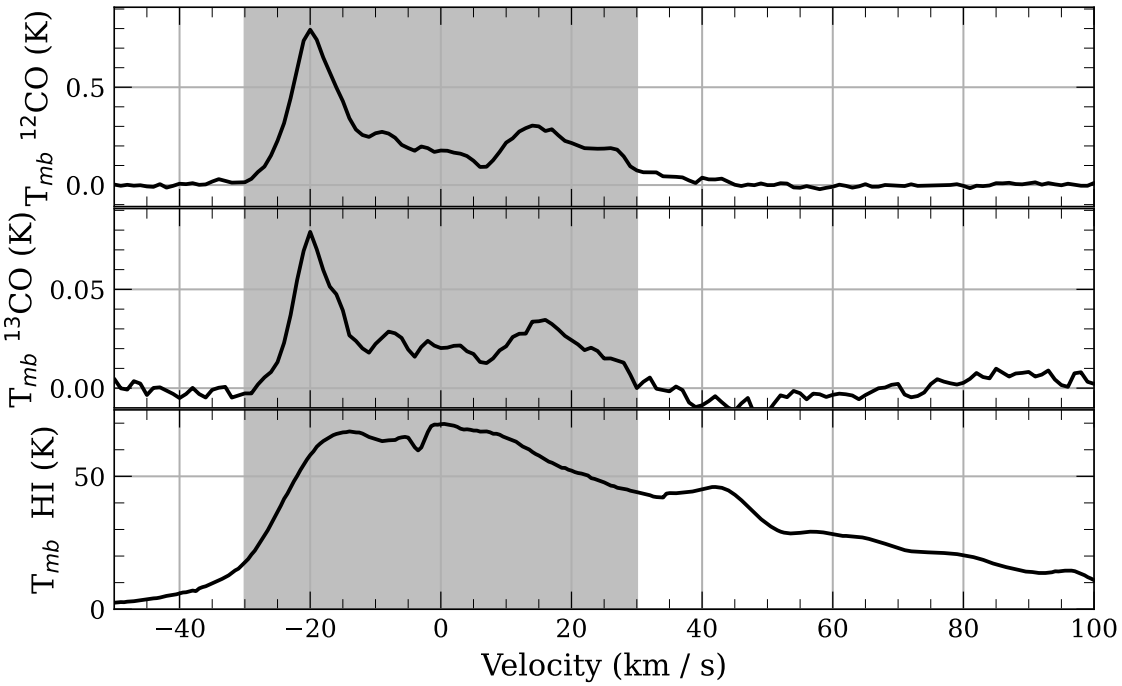

Figure 5. Spectral Cube Velocity Window

Note: The average spectral intensity of the Mopra ^{12}CO, ^{13}CO, and HI cube for a window from -55 $\lesssim$ v_{LSR} $\lesssim$ 100 kms^{-1}. The spectral units of the position-position-velocity cubes are K, and the spectral axis is in kms^{-1}. Not pictured here is the C^{18}O cube because it was much weaker relative to the other cubes. The strength of the HI signal was very high, as expected, because of how prevalent it is throughout Carina and the Milky Way. Emission from ^{12}CO was stronger than ^{13}CO because it can come from the diffuse part of the transition cloud as well as the dense areas, whereas ^{13}CO will only be found in the dense molecular regions. The dark grey region highlights the velocity range used when working with the FITS cubes, and encompasses velocities from -30 to +30 kms^{-1} . This window is chosen to try and exclude background emission from beyond the nebula but preserve key information present in all images.

A map of HI can be seen in Fig. 6 with units of K kms^{-1}. Integrating the 8 K noise per channel from section 2.3.2 gave a map $\sigma \sim 30$ K kms^{-1}. The majority of the HI map had signal above 3σ except for pixels near the center where the low atomic column density meant the hydrogen was likely ionised there. This was confirmed by overlapping pixels from the radio continuum map seen in Fig. 7.

In order to do a pixel by pixel comparison of HI data to CO, the HI moment map had to be resampled and regridded to match projection of the CO cube. HI was resampled into the CO coordinate grid because the HI had higher resolution, albeit slightly. The HI data was smoothed to the beam FWHM of the CO data by convolution with a 1-d gaussian filter kernel before resampling. The sigma factor used in the gaussian smoothing function was calculated as:

$$\sigma = \frac{1}{2\sqrt{2\ln(2)}} \frac{\Theta_{\mathrm{CO}}}{\text{Pix-scale}_{\mathrm{HI}}} \tag{2.2}$$

Where Θ_{CO} is the full-width at half maximum value of the beam of the Mopra CO data in units of degrees. Pix-scale$_{\mathrm{HI}}$ is the conversion value for degrees per pixel in the HI data cube. The resulting sigma value is in pixels.

After gaussian smoothing, the data was resampled to a lower resolution. Then they could be re-grid to match the projection of the other data set's world coordinate systems (WCS). This same process was repeated on the dust column density map.

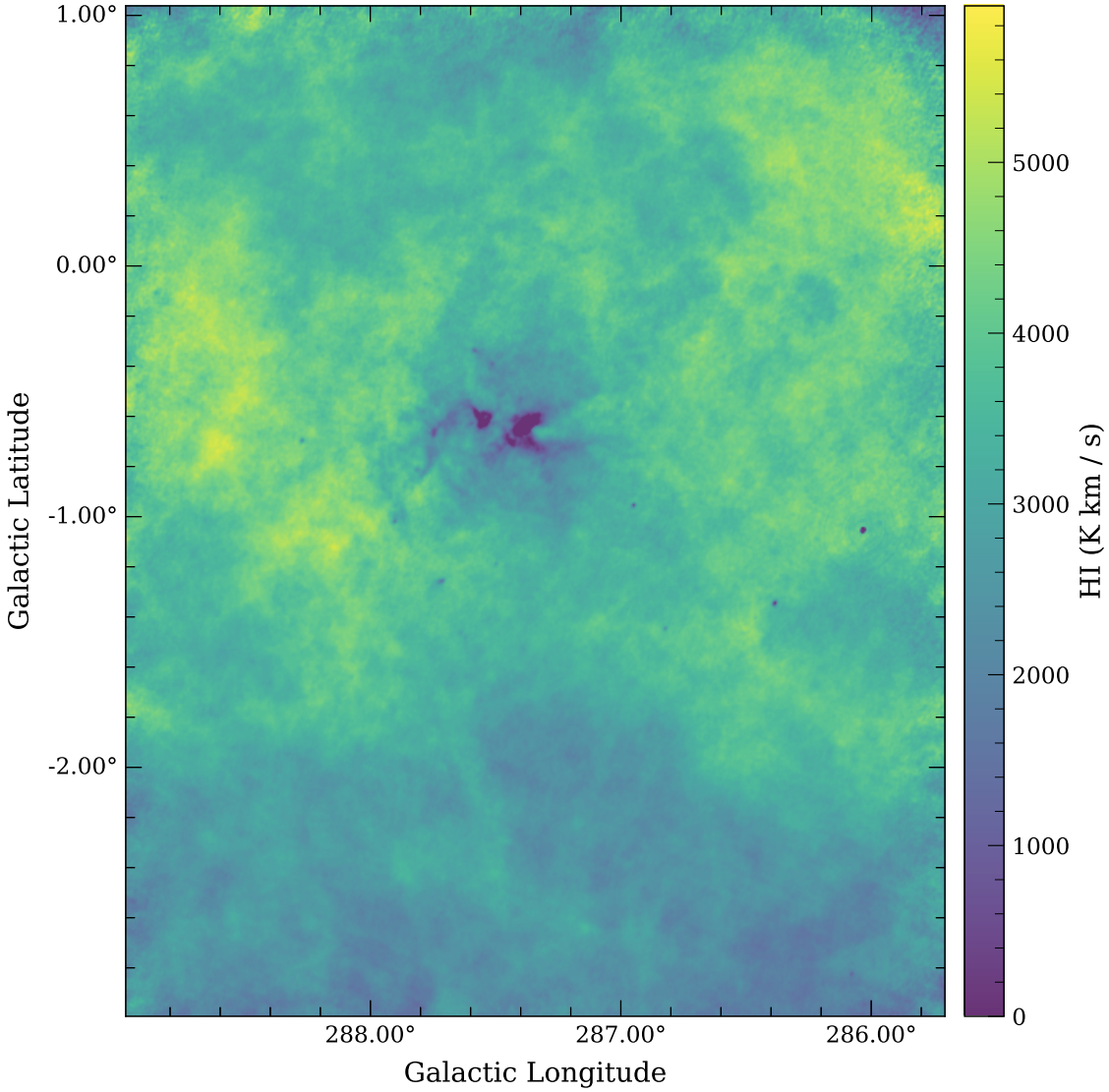

Figure 6. HI Moment Map

Note: Integrated intensity map of the HI 21-cm line in the Carina Nebula. The velocity ranges from -30 to +30 kms^{-1} . In the center of the data set is a region of very low HI emission and this is likely due to a high volume of hydrogen present as H+.

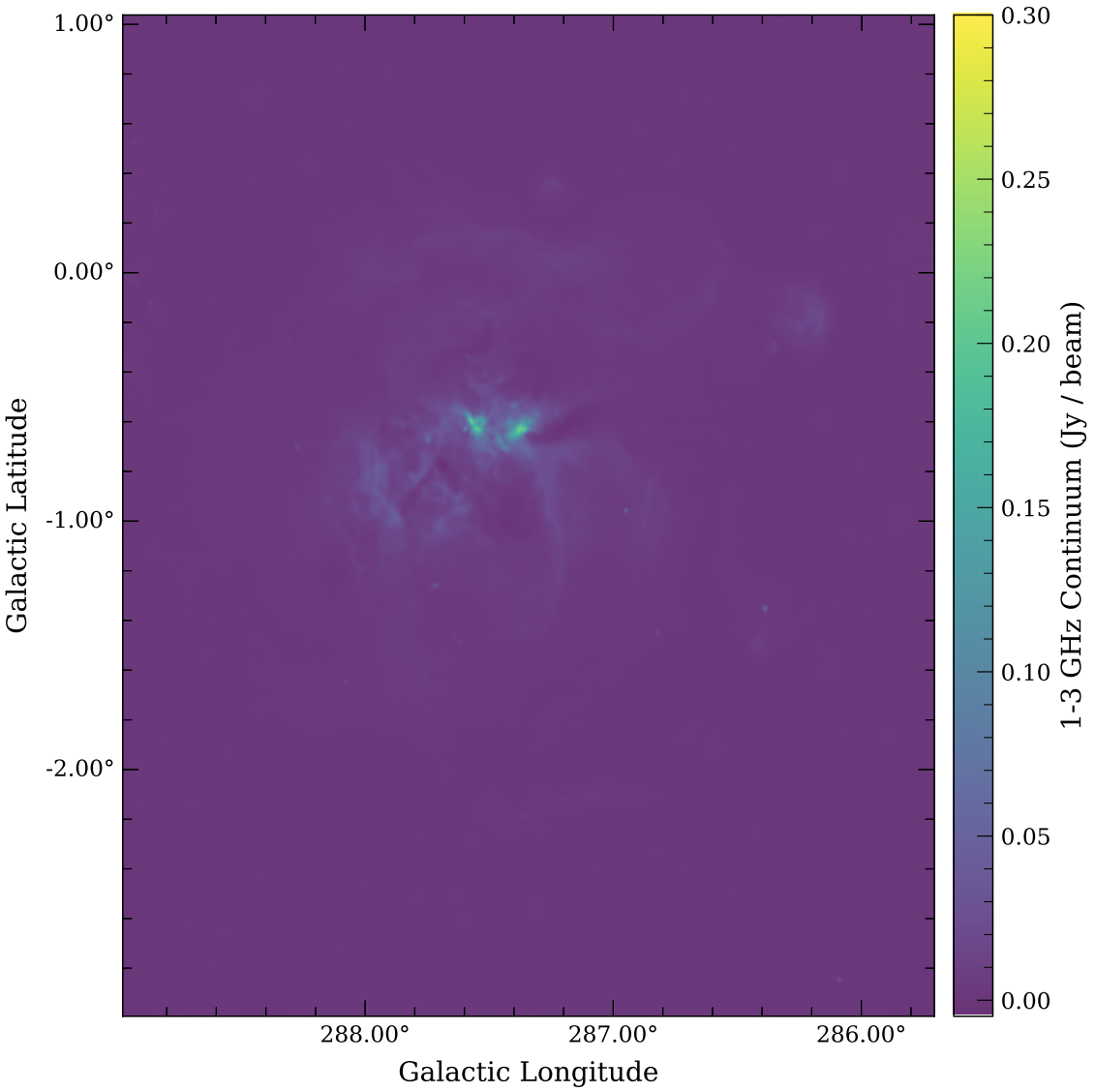

Figure 7. H+ Moment Map

Note: The radio continuum emission image averaged over 1 - 3 GHz. The spatial coverage is from 285.5 $\lesssim$ l $\lesssim$ 289.1 degrees, -3.20 $\lesssim$ l $\lesssim$ 1.14 degrees, and rms σ = 2.8 mJy beam−1. Units are in Jy beam^{-1}. Higher ionization corresponds to empty or dark region of the HI map.

2.4.2 CO Masking

Background subtraction for the Mopra data proved to be more difficult than the other cases. A straightforward calculation of the rms noise and pixel masking using n $\times$ $\sigma_{\rm rms}$ did not effectively remove the background. The method outlined in Rosolowsky and Leroy (2006), Rebolledo et al. (2015), and Rebolledo et al. (2016) was followed which, enhanced the signal to noise ratio of extended emission line profiles by creating a signal mask from a smoothed cube and applying it to the original image to identify regions of significant emission.

The basic steps of the process were to smooth the position-position-velocity cube in the spatial and spectral domains by some factor x. This was called the signal mask and it would be applied to the original data. Following this step, one would calculate the rms noise from a relatively empty region of the map, this was $\sigma_{\rm smo}$. Then the signal cube was masked by some threshold n $\times$ $\sigma_{\rm smo}$, keeping only pixels that were at or above this value for at least two consecutive velocity channels. This threshold limit was intended to include pixels with strong emission peaks. Then n was typically reduced to include the extended emission surrounding the peak. With all other pixels removed, a mask was made that could be applied directly to the original image.

In this work the spectral resolution of 1 kms^{-1} was intentionally degraded by a factor of 5 using a gaussian smoothing function. The data was further smoothed spatially by a factor of 3 for a new beam resolution of $\sim$ 100 arcsec. The noise for the dilated ^{12}CO cube was estimated to be $\sigma_{\rm smo}$ = 0.36 K and then $n_{\rm edge}$ = 3.8. Thus pixels below $\sim$ 4$\sigma_{\rm smo}$ were rejected and the resulting image was used to mask the original data cube. Figure 3 was made using the dilated mask method. The final

image included only pixels above 3σ where $\sigma = 2.8$ K kms^{-1} which was found from $\sigma_{\rm smo}$, the velocity resolution, and number of channels used in the integrated intensity map like the HI σ in section 2.4.1. For the remaining CO cubes I calculated $\sigma_{\rm smo,^{13}CO}$ = 0.18 K, $n_{\rm edge} = 2.5$ for ^{13}CO , $\sigma_{\rm smo,C^{18}O} = 0.18$ K, $n_{\rm edge} = 1$ for C^{18}O which is again only used for qualitative purposes since C^{18}O signal was so much weaker than the others.

I could then further separate the Mopra CO data by regions of density. The carbon monoxide isotopologues ^{13}CO, and C^{18}O were less abundant than ^{12}CO since their transitions are only found in the denser regions of the molecular gas. Using the same approach as in Pineda et al. (2010) and Goldsmith et al. (2008) I defined a set of density masks as follows. Mask 0 was pixels that contain no signal from any CO source above the threshold 3σ limit. Mask 1 only counted signal from ^{12}CO and had no overlap with ^{13}CO or C^{18}O. Mask 2 was the region where both ^{12}CO and ^{13}CO signals overlapped, and Mask 3 was where ^{12}CO, ^{13}CO, and C^{18}O were detected. Figure 8 shows all the masked regions made with Mopra CO data. Mask 0 is in white, Mask 1 is in dark blue, Mask 2 is in black, and Mask 3 is in pink. C^{18}O was particularly weak in signal compared to the other two CO lines. Thus the inclusion of Mask 3 was more for qualitative purposes and should highlight only the densest regions of the nebula.

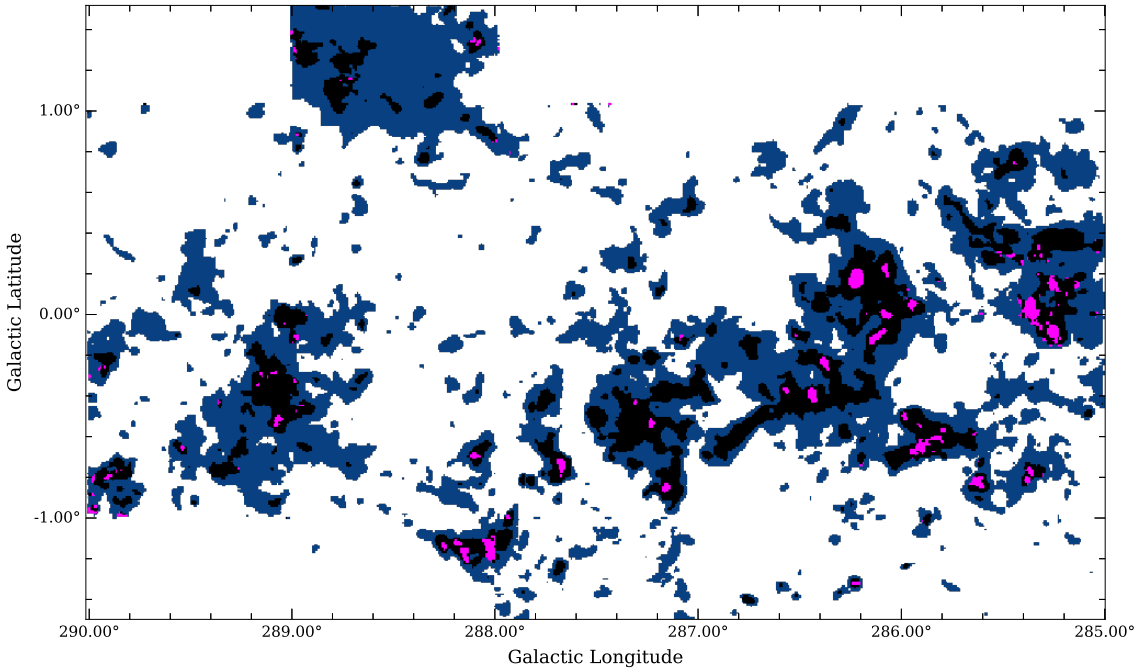

Figure 8. Mask Overlay

Note: Various masks of the ^{12}CO Mopra data highlighting the different regions of density. Mask 0 is in white showing the region where no signal from any CO source is present. Mask 1 is in dark blue highlighting the more diffuse part of the cloud where only ^{12}CO is detected above threshold levels. Mask 2 is in black showing denser parts of Carina where both ^{12}CO, and ^{13}CO are detected. Mask 3 highlights the densest regions traced by ^{12}CO, ^{13}CO and C^{18}O.

2.4.3 Column Density Maps

Column density maps can be made from integrated intensity images using a conversion factor that is different depending on the spectral line being integrated. In order to calculate the column density of molecular hydrogen that was traced by ^{12}CO I used the conversion factor $X_{CO} = 2 \times 10^{20}$ cm^{-2}s K^{-1}km^{-1} (Pineda et al. 2017) and equation 2.3.

$$N_{H_2}(^{12}\mathrm{CO}) = X_{\mathrm{CO}} I_{^{12}\mathrm{CO}}. \tag{2.3}$$

Here $I_{^{12}\mathrm{CO}}$ is the integrated line of sight intensity of ^{12}CO with units K km s^{-1}. The same process was repeated on the HI data to calculate column density from the atomic hydrogen. I used the conversion factor $X_{\mathrm{HI}} = 1.82 \times 10^{18}$ cm^{-2} s K^{-1} km^{-1} and integrated intensity from HI.

The molecular hydrogen column density map derived from dust N_{H_2}(dust) was created by Rebolledo et al. (2016) and reproduced here in Figure 4. As mentioned in sec 2.3 the image was made by spectral energy distribution (SEDs) fitting of far infrared (FIR) dust data to a grey body function. The data used in the fit included 70, 150, 250, 350, and 500 μm Herschel images brought to a common angular resolution and fit pixel by pixel. This method yielded a mass density for each pixel which could be converted to an H_2 column density assuming the dust was tracing only molecular hydrogen by using the equation

$$N_{H_2}(\mathrm{dust}) = \frac{n_{\mathrm{dust}}}{\mu_{H_2}\, m_{\mathrm{H}}\, R_{\mathrm{dg}}} \tag{2.4}$$

which is Equation 10 in Rebolledo et al. (2016). The variable n_{dust} is for mass density in units g cm^{-2}, μ_{H_2} was the mean molecular weight assumed to be 2.72

with units of hydrogen mass, m_H was the mass of the hydrogen atom, and $R_{dg} = 0.01$ was the dust to gas ratio. As mentioned previously this assumption is likely true due to the thermal considerations of the nebula.

If I were, however, to assume the dust continuum emission was tracing both H and H_2 and not just molecular hydrogen than I could find total hydrogen column density N(H + H_2) from Equation 2.4 by using the mean molecular weight for hydrogen instead. This is $\mu_H \sim 1.7$ accounting for a helium correction. Then taking the column density of hydrogen derived from HI and subtracting it from the total column density would give a new N_{H_2} map. Fig. 9 is the resulting image. Contour lines of ^{12}CO and ^{13}CO are overlaid for a qualitative assessment. If this map were accurate the molecular hydrogen traced by dust would at a minimum contain the same data as molecular gas traced by CO emission. Because this was not the case, i.e. this method under-predicted the molecular hydrogen, I could assume this method resulted in an over-subtraction and that the dust continuum emission was indeed coming from a mostly molecular component.

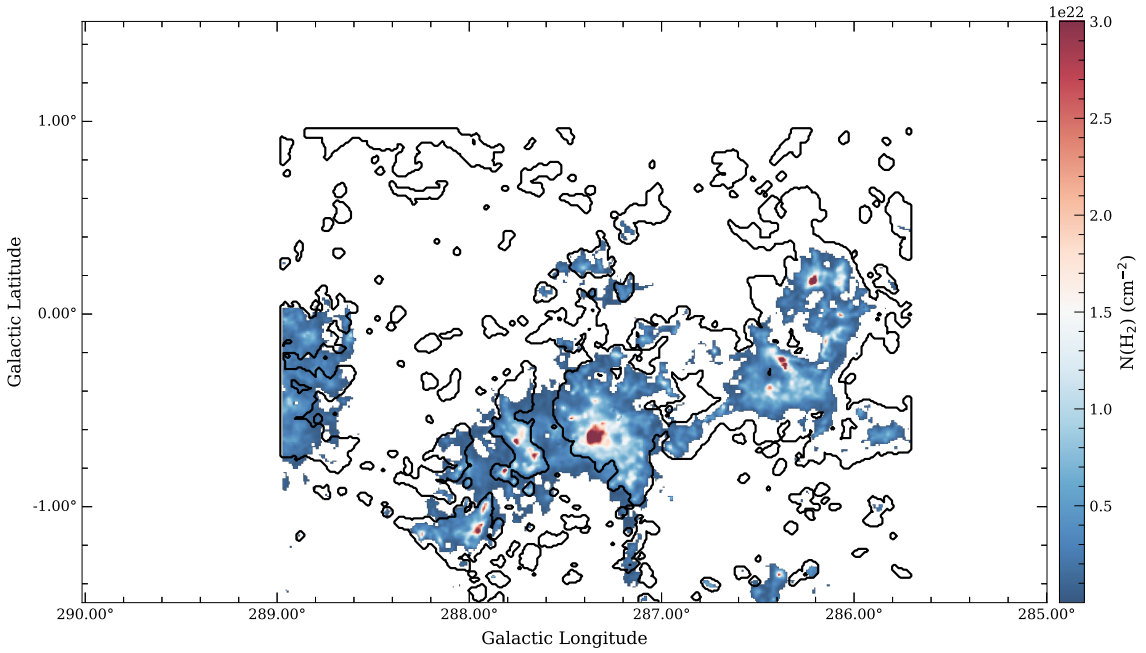

Figure 9. N_{H_2} Map Over-Subtraction

Note: Molecular column density derived from dust continuum emission assuming dust is tracing both atomic and molecular hydrogen. The map is made by subtracting column density of hydrogen derived from HI emission since N(H + H_2) = N(H) + $2N_{H_2}$. Contour lines of CO emission are added to show this method results in an over-subtraction of hydrogen column density. Dust emission would be able to detect more molecular gas than CO measurements so the lower quantity implies that dust emission is originating from entirely molecular regions.

Another check that the dust is tracing molecular hydrogen is to plot pixel by pixel the dust compared to CO emission. I used masks of ^{12}CO and ^{13}CO to isolate identical pixels in the dust map. Particularly useful here was the ^{13}CO which should have trace the denser parts of the molecular cloud. Plotting the pixels on a log-log scale can show any one-to-one correlation as a diagonal line. I do this for the entire nebula that overlaps with CO in Figure 10. The solid identity line represented the region where the density of each pixel is equal between the two maps. The dashed lines represented the bounds $\pm$ 40 %. The gaussian density plot assigned a weight to how correlated the pixels were. For the entire CO region some 60 % of pixels have a strong correlation and most of them fall within the bounds of the identity line. I also repeated the process for a specific region of Carina spanning less than 1 square degree known as the northern cloud, the region pictured in Figure 11. Here there was a strong convergence along the identity line which was made more pronounced by the fewer pixels used, as seen in Figure 12.

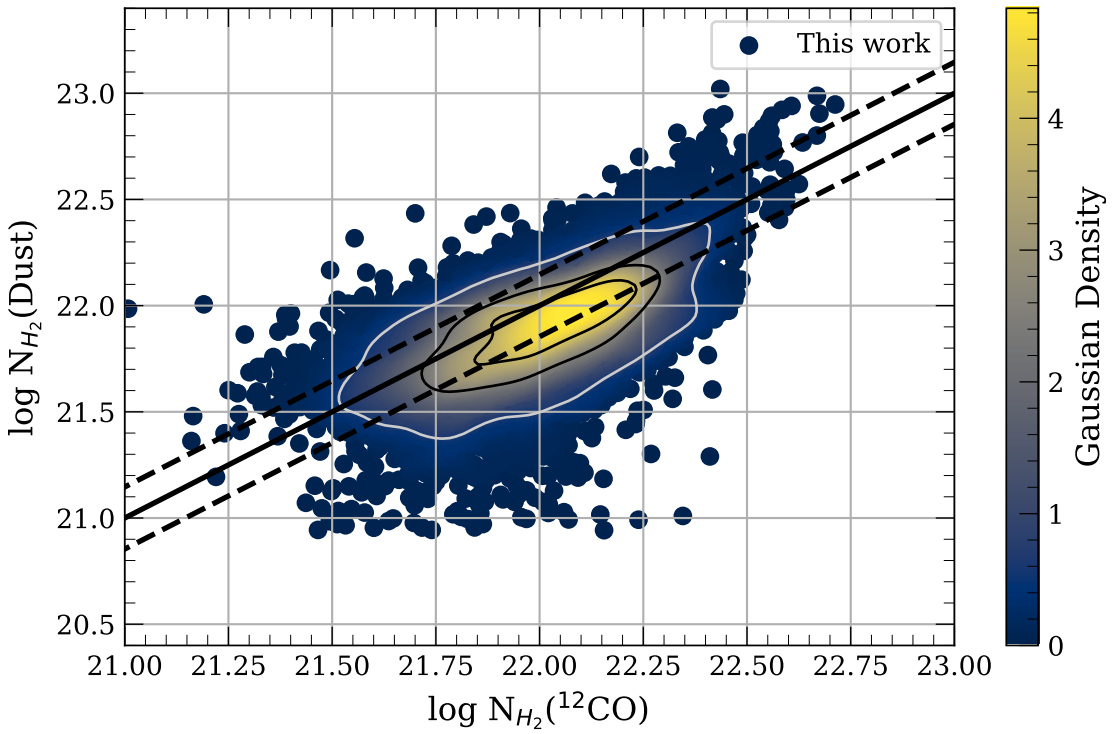

Figure 10. Dust Correlation of the CNC

Note: Log-log plot of molecular hydrogen column density N_{H_2} as it is traced by dust and ^{12}CO emission vs H_2 derived from the dust continuum. The white contour highlights the region containing 90 % of the pixels, while the second, and third contours highlight 60 %, and 30 % respectively. A Gaussian density is used to differentiate areas of heavy over-lap. The solid diagonal line shows where the one-to-one correlation would be. It is flanked by dashed lines showing ± 40 %. This shows that the majority of column density in overlapping pixels is within 40 % agreement between dust and CO.

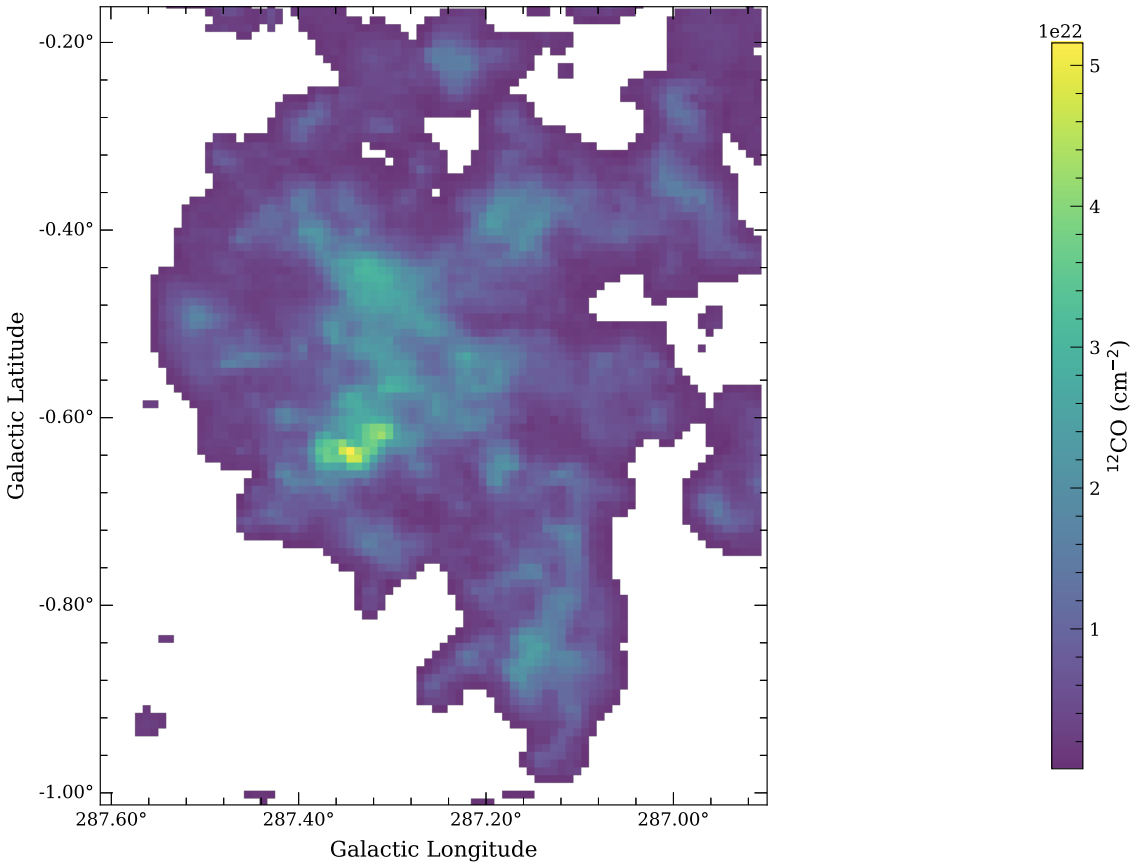

Figure 11. ^{12}CO Emission from the Northern Cloud

Note: Map of CO emission spanning the Northern Clouds of the Carina Nebula Complex. This is a dense part of the giant molecular cloud with bright star clusters but is not believed to be actively forming new stars.

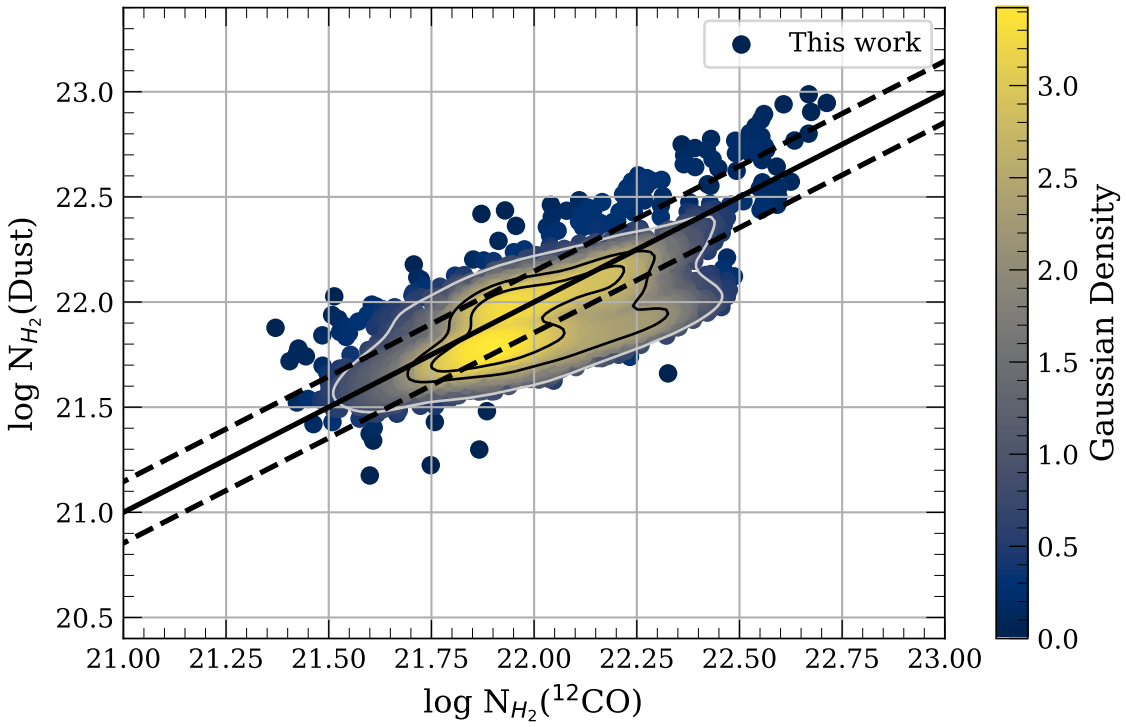

Figure 12. Dust Correlation of the Northern Cloud

Note: Pixel-by-pixel comparison of dust and CO emission in the norther cloud of the Carina Nebula. As in Figure 10 The contours are at 90, 60, 30% of pixels. The solid and dashed diagonal lines shows where the one-to-one ± 40%. This shows that the strongest convergence of column density in overlapping pixels is within 40% agreement between dust and CO.

The choice of X_{CO} also factors in to the accuracy of H_2 column density derived from CO. In Fig. 19 of Rebolledo et al. (2015) they apply a similar approach with density plots to show why $X_{CO} = 2 \times 10^{20}$ cm^{-2}s K^{-1}km^{-1} is a good value for Carina. Going forward Fig. 4 of this work will be used for calculations involving molecular hydrogen column density.

The presence of ionized gas has an impact on the overall H column density. To better understand the H+ contribution, I used Radio continuum maps of 1-3 GHz from Rebolledo et al. (2021) which are reproduced here as Figure 7. Diffuse radio emission was present throughout the nebula, as very strong absorption features in HI images (Figure 6) which coincide with very strong radio continuum emission. Before the continuum image could be used to compare directly to HI and the CO images, one must convert the map to column density. To do this I used the method outlined in chapter 10 of Wilson, Rohlfs, and Susanne (2009). First I converted the original H+ continuum image to a map of temperature brightness T_b by using Rayleigh-Jeans law at each pixel. The brightness temperature from the Rayleigh-Jeans law is defined as the temperature of an ideal, equivalent black body which will give the same power per unit area per unit frequency per unit solid angle as the observed source:

$$T_b = \frac{c^2}{2k\nu^2\Omega} S_\nu \tag{2.5}$$

Here T_b is in degrees kelvin, S_ν is the observed flux density in units of Jy, and Ω is the main beam solid angle in units of steradian. The center frequency of the band is $\nu = 2.1$ GHz, and k is the Boltzmann constant. I converted the continuum image from Jy beam^{-1} to Jy sr^{-1} with standard astropy functions and making use of the fact that for a gaussian the beam area is $\Omega = 2\pi\sigma^2$. The FWHM value for

major and minor axes of the beam are $\Theta_{\rm maj} = 6.78 \times 10^{-3}$ degrees, and $\Theta_{\rm min} = 4.39 \times 10^{-3}$ degrees respectively. The ratio of the standard deviation of the beam to the FWHM for a Gaussian is again $\sigma = (2\sqrt{2\ln(2)})^{-1}\ \Theta$. In order convert the temperature brightness map to one of optical depth I made use of the relation:

$$T_b = T(1 - e^{\tau}) \tag{2.6}$$

Here the optical depth τ is defined as

$$\tau = \int \kappa_\nu ds \tag{2.7}$$

Where κ_ν is the linear absorption coefficient. From Kirchoff's law $\kappa_\nu = \epsilon_\nu \left(B_n u(T)\right)^{-1}$ and ϵ_ν is the emissivity and $\mathrm{B}_n u(\mathrm{T})$ is the spectral radiance. I assume constant electron temperature along the line of sight for an HII region in local thermodynamic equilibrium (LTE) to be T $\sim$ 8000 K for ionized gas. I can relate the optical depth to emission measure EM using the following:

$$\tau \approx 3.014 \times 10^{-2} \left(T\right)^{-3/2} \left(\nu\right)^{-2} \mathrm{EM} < g_{\rm ff} > \tag{2.8}$$

Here T is in units of K, ν is in GHz, EM is pc cm^{-2}, and $<\mathrm{g_{ff}}>$ is the free-free gaunt factor used as a quantum correction when calculating continuous emission in the classical approach (Brussaard and Van De Hulst 1962; De Avillez and Breitschwerdt 2015).

$$< g_{\rm ff} > \approx \ln\left[4.955 \times 10^{-2} \nu^{-1}\right] + 1.5 \ln\left(T\right) \tag{2.9}$$

Where ν is again in GHz, and T in kelvin. Relating EM to electron density n_e is the equation:

$$\mathrm{EM} = \int_{\mathrm{los}} n_{\mathrm{e}}^2 ds \tag{2.10}$$

The electron number density $\mathrm{n_e}$ is in units of $\mathrm{cm^{-3}}$. Here it is important to note for ionized hydrogen $\mathrm{n_e^2} \sim \mathrm{n_e n_i}$ and if one assumed a uniform temperature in the ionized regions, the electron density would remain constant and 2.10 becomes $\mathrm{EM} = n_{\mathrm{e}} \int_{\mathrm{los}} n_{\mathrm{i}} ds$ with the integral now being a sum of the ionized hydrogen along the line of sight or in other words the column density of H+.

$$N_{\mathrm{H+}} = \frac{\mathrm{EM}}{n_{\mathrm{e}}} \tag{2.11}$$

An average electron density for the Carina nebula from [NII] emission was derived by Oberst (2009) to be $\mathrm{n_e} = 29\ \mathrm{cm^{-3}}$, and was used in the calculation of $\mathrm{N_{H+}}$. The converted column density image can be seen in Fig. 13.

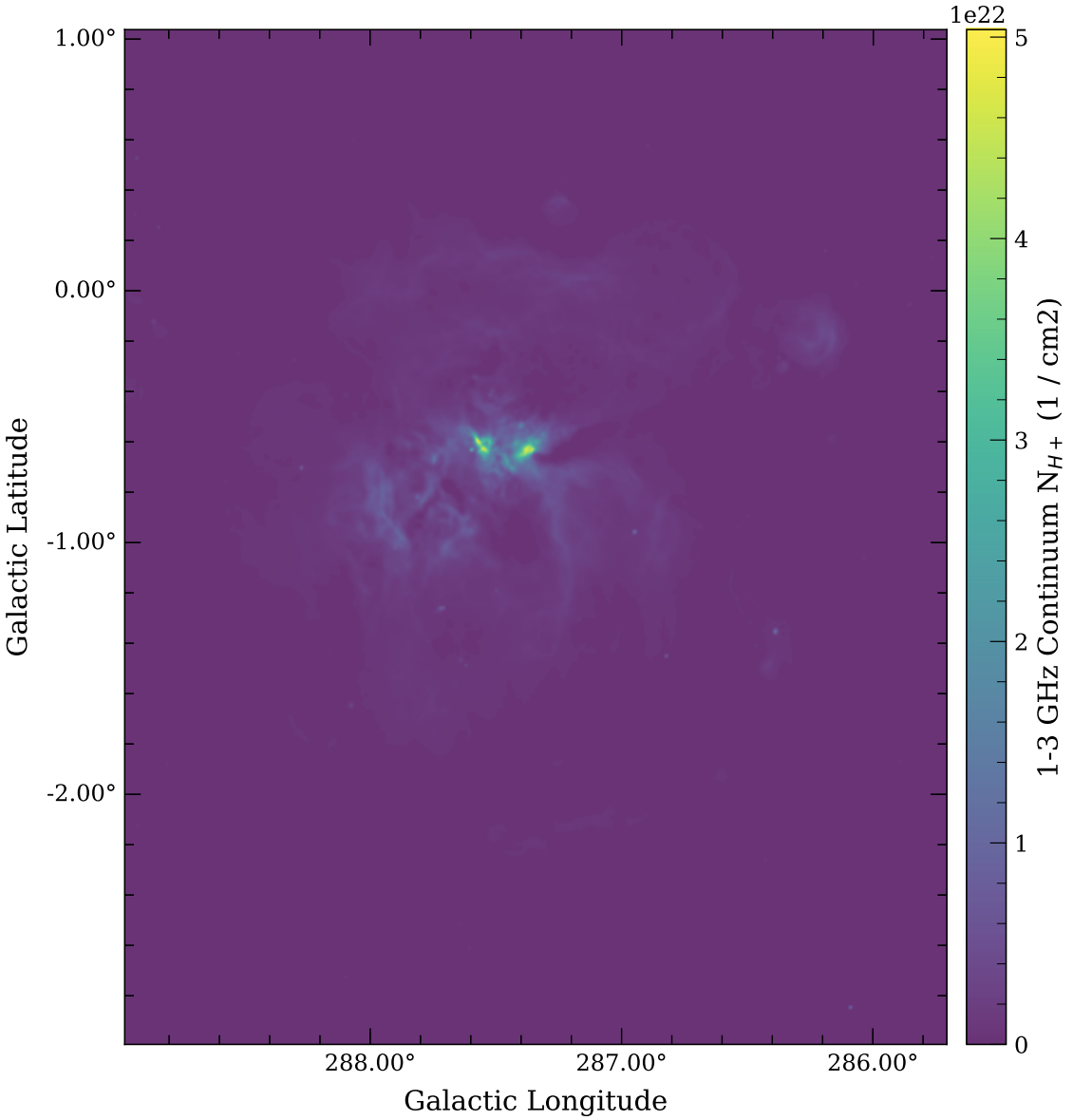

Figure 13. Column Density as a Function of Ionized Gas

Note: Hydrogen column density as a function of ionized hydrogen N_{H+} derived from averaged 1 - 3 GHz radio continuum images.

2.5 Analysis

When the ancillary data was further processed and prepared, I could start to make predictions and estimates from combining different maps. The fraction of gas that was molecular compared to the overall cloud is discussed in section 2.5.1. I compare the derived maps to theory in section 2.5.2. I predict the CO-dark region of the nebula in section 2.5.3.

2.5.1 Molecular Fraction From Dust Maps

Next I derived an estimate for the fraction of the Carina Nebula in the form of molecular hydrogen. To do this I first had to write the total neutral column density as it came from atomic and molecular hydrogen as $N(H + H_2) = N(H) + 2N_{H_2}(Dust)$. After following through with the steps outlined in sections 2.4.1, 2.4.2 and 2.4.3, I had maps for molecular hydrogen column density N_{H_2} from the dust continuum and N(H) from HI emission that were all re-sampled and rescaled and in the same column density units. This allowed for direct combination of the HI map to the dust continuum map which would yield $N(H + H_2)$. This hydrogen column density map is shown in Figure 14 with the denser parts of the map coincided with strong CO emission. The molecular fraction $f(H_2)$ as shown in Figure 15 is given by,

$$f(H_2) = \frac{2N_{H_2}}{N(H) + 2N_{H_2}} \tag{2.12}$$

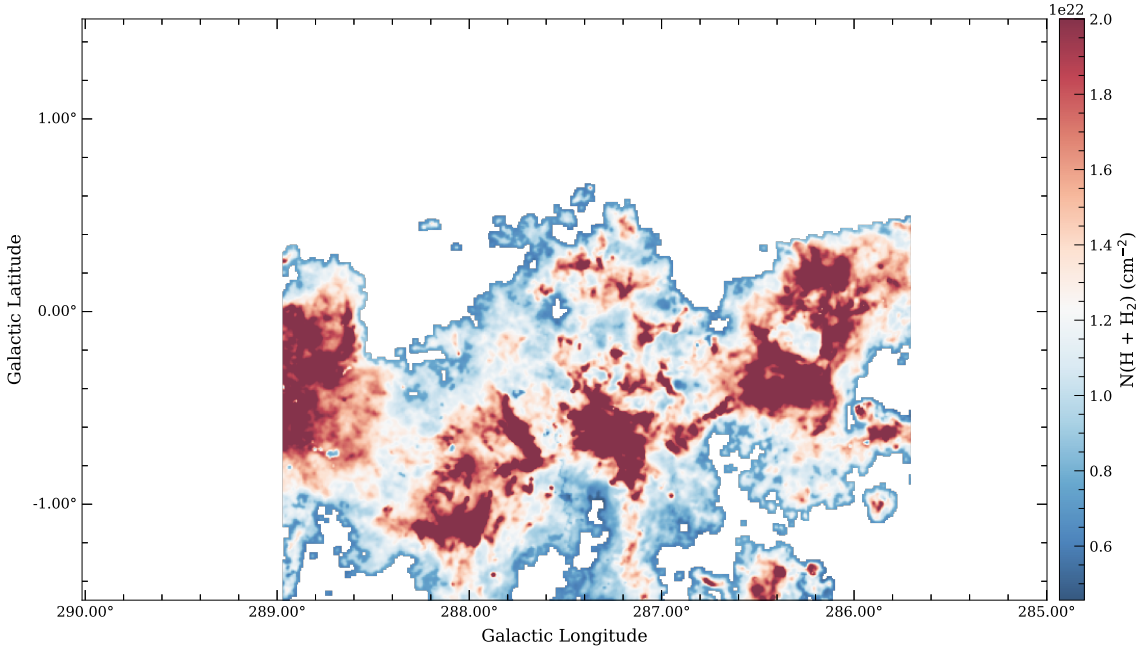

Figure 14. Hydorgen Column Density N(H + H_2)

Note: An intermediate step to the molecular fraction is the total hydrogen column density map N(H + H_2) with units cm^{-2}. Image made from adding atomic hydrogen to the dust continuum map of molecular hydrogen. The HI data is narrower in Galactic longitude coordinates and results in a slight truncation of the molecular hydrogen coverage in the final column density map.

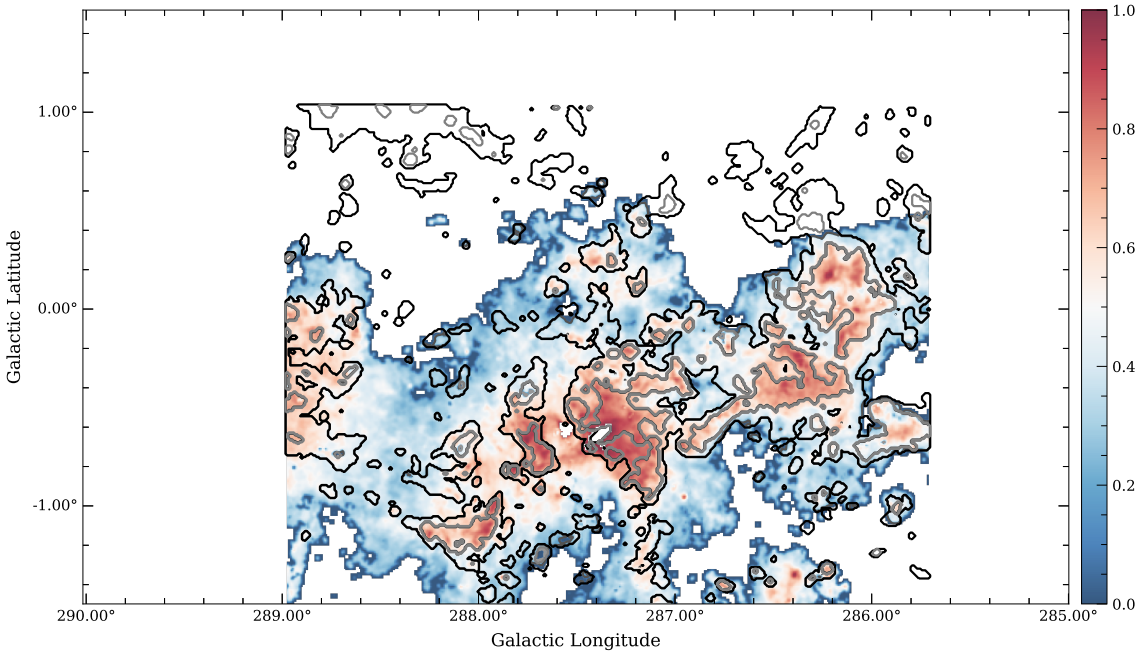

Figure 15. Molecular Fraction f(H_2) Map

Note: This map was estimated from dust continuum data and HI 21-cm line emission maps. The image contains only pixels above 3 σ of N_{H_2}, and regions of very low HI column density are also removed from the image as they most likely indicate ionized regions. The contours in the image represent CO masks 1 (black) and 2 (grey) to identify which regions belong to diffuse gas or dense molecular clouds respectively.

Pixels have been removed from Fig. 15 based on 3σ cuts of the HI, and dust continuum maps used to create N(H + H_2) and by extension f(H_2). A contour outline of CO Mask 1 (pixel with emission from only ^{12}CO) is superimposed in black, while a contour outlining Mask 2 (pixels from ^{12}CO + ^{13}CO emission) is seen in grey. Several pixels with high f(H_2) are within the Mask 2 outline as this mask should identify denser regions of the nebula. The black outline of Mask 1 not only shows the diffuse region but also the edge of the detectable CO emission. From this map I could immediately see that there was a significant portion of molecular hydrogen that was not traced by CO data.

2.5.2 Theoretical Models

The theoretical value for the molecular fraction f(H_2) as a function of surface density and metallicity Z' was defined in detail in Sternberg et al. (2014) and McKee and Krumholz (2010). Figure 16, and Figure 17 are plots of molecular fraction as a function of total column density for each pixel in the maps as well as the theoretical curves for f(H_2). The entire derivation will not be reproduced here, however several key components beneficial to reproducing these plots will be discussed now. The fundamental parameter for the HI to H_2 transition is given as equation (51) in Sternberg et al. (2014) and transcribed as equation 2.13 below.

$$\alpha G = \frac{I_{\rm UV}}{(n/100{\rm cm}^{-3})} \frac{\phi_g}{1 + (2.64\phi_g Z')^{1/2}} \tag{2.13}$$

$I_{\rm UV}$ is a scaling factor for the field intensity of far ultra violet (FUV) photons from 6 eV $\lesssim$ hν $\lesssim$ 13.6 eV in free-space, n is the total volume density of hydrogen in units of cm^{-3}, Z' is the metallicity, and ϕ_g is a scale factor used to compare grain

cross sections between Sternberg et al. (2014) and McKee and Krumholz (2010) which is 1.9 or 1.0 / 1.9 for the respective papers. Another important difference to note is that in McKee and Krumholz (2010), the denominator of equation 2.13 does not have the $(2.64\ \phi_g\ \mathrm{Z'})^{1/2}$ term. Equation (98) in Sternberg et al. (2014) is the optical depth of of HI-dust given here as equation 2.14.

$$\tau_1^p = 1.6\ \ln\left[\frac{\alpha G}{3.2} + 1\right] \tag{2.14}$$

Equations (96) and (97) of Sternberg et al. (2014) allow for the calculation of total HI column density and molecular fraction respectively and here as equation 2.15 and equation 2.16.

$$N_{1,\mathrm{tot}} = \frac{1}{\sigma_\mathrm{g}}\ \ln\left[\frac{\alpha G}{2} + 1\right] \tag{2.15}$$

Where $\sigma_g = 1.9 \times 10^{-21}\ \phi_g$ Z' cm^{-3} is the FUV grain absorption cross section in units of cm^{-2}

$$f_{H_2}^p = 1 - \frac{1}{y} \tag{2.16}$$

Here y = Σ_{gas} / $\Sigma_{\mathrm{gas,\ HI}}$ which is the ratio of total gas mass surface density to surface mass density of HI. The relation between total gas density and total gas mass surface density Σ_{gas} [M$\odot$ pc^{-2}], is $\mathrm{N_{tot}} = \frac{\Sigma_{gas}}{1.124\times10^{-20}}$. Then one may use y = $\mathrm{N_{tot}}$ / $\mathrm{N_{1,tot}}$ and equation 2.16 becomes a function of $\mathrm{N_{tot}}$. For equations 2.13 - 2.16 I followed the approach in Sternberg et al. (2014) to calculate for a geometry that is a planar slab sandwich with isotropic radiation. The metallicity for Carina is assumed to be the same as the rest of the Milky Way Z' = 1. This leaves only the FUV field intensity and hydrogen volume density n as free parameters. In Sternberg et al. (2014) the authors used a low volume density that was proportional to $\mathrm{I_{UV}}$

for a region in a two-phase equilibrium between a cold neutral medium (CNM) and warm neutral medium (WNM). This resulted in a version of equation 2.13 where the parameter αG only depends on Z'. In this scenario for Z' = 1 the equivalent ratio I_{UV} / n = 0.043 cm^3. This did not prove to be a good fit to my predicted data, however both I_{UV} and n have a wide range of values they can take. Further varying this ratio was done until the fit shown in Fig. 16 was achieved at I_{UV} / n = 400 cm^3. Assuming two-phase equilibrium volume density n = 23 cm^{-3} would give $I_{UV} \sim 10^4$. This is in the range of parameters for I_{UV}, however it is worth noting that pixels accounted for in these images that span many regions of varying n, and I_{UV}. For these reasons it is unlikely that a single value for density or field intensity would be constant for the entire region and that the ratio measured is likely an average for the most part in the nebula. The solid red line in the Figure corresponds to the equations in Sternberg et al. (2014), and the dotted line is the approach in McKee and Krumholz (2010) where as previously mentioned the αG denominator is changed and $\phi_g = 1.0/1.9$.

By contrast if I look at a similar plots of the Large (LMC) and Small Magellanic Clouds (SMC) in Pineda et al. (2017), here they assumed an intensity field 1.3 x stronger than McKee and Krumholz (2010) and Sternberg et al. (2014) for the LMC, and a field 1.9 x stronger for the SMC. For both cases they assumed the same density ($n_{cnm} \sim 20$ cm^{-3}. Both LMC, and SMC have fractional metallicity compared to Carina. The average curve fit for the Carina nebula matches more closely to the SMC line profile than the LMC. In order for the curves to be similar the higher metallicity of the Carina nebula would then require a much higher I_{UV} field. Using masks from section 2.4.2 where mask 1 traces pixels from the diffuse region of the cloud and mask 2 traces the dense I separated the f(H_2) map. Fig. 16

is a density plot with pixels shared by f(H_2) and ^{12}CO (mask1). Fig. 17 shows f(H_2) pixels traced by ^{12}CO and ^{13}CO. I also included the mask 0 maps which show all of the molecular fraction not coincident with any CO emission as Figure 18. The mask 0 plot showed two distinct regions of dense pixel groupings. One near f(H_2) $\sim$ 0.4, and the other near 0. This is low molecular fraction region is representative of the dust map boundary where the column density was nearly below the detection limit. Because the boundary was fairly consistent over the entire map there is a large volume of pixels with similar values. The line is fit to the higher fraction data as this grouping is comprised of the majority of the nebula.

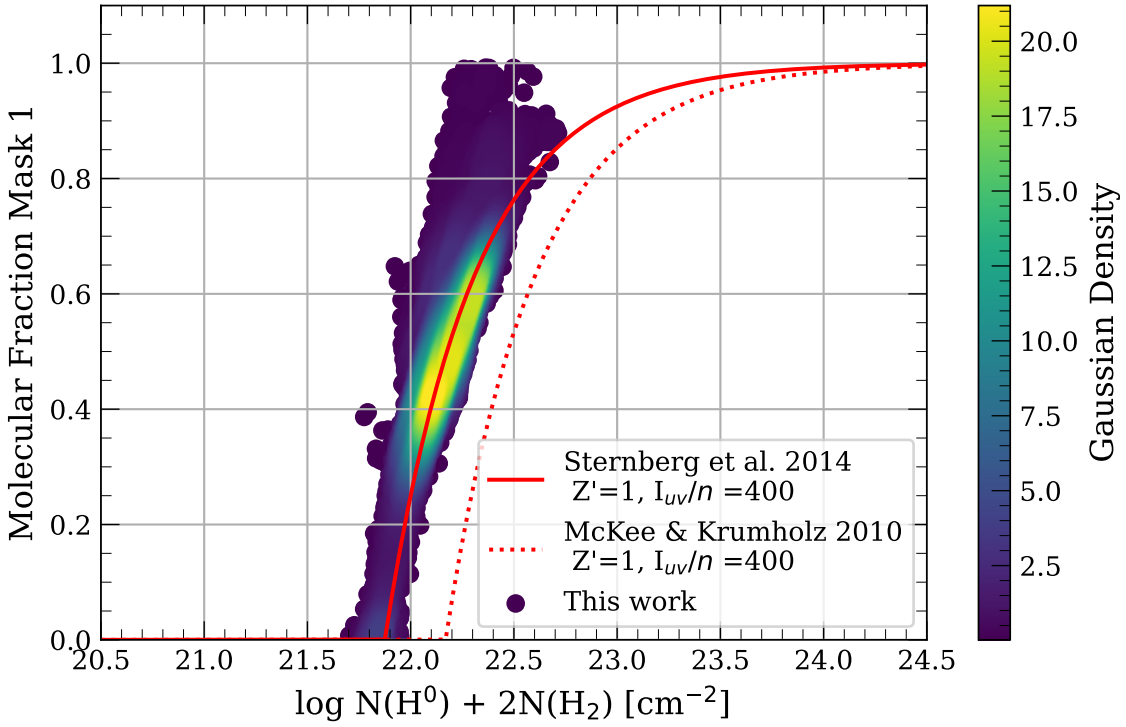

Figure 16. Molecular Fraction vs Dust Mask 1

Note: Molecular fraction f(H_2) plotted against column density from dust on a log scale. Due to tremendous overlap between data points the molecular fraction is plotted with a gaussian density for convenience. The f(H_2) data points in this plot correspond to pixels that overlap only with ^{12}CO emission or mask 1 as discussed in section 2.4.2. These pixels belong to the diffuse region of the molecular fraction map outlined in black. The theoretical lines from Sternberg et al. (2014) (red solid line) and McKee and Krumholz (2010) (red dashed line) are plotted against the data with an approximate best fit where the ratio I_{uv} / n = 400 cm^3.

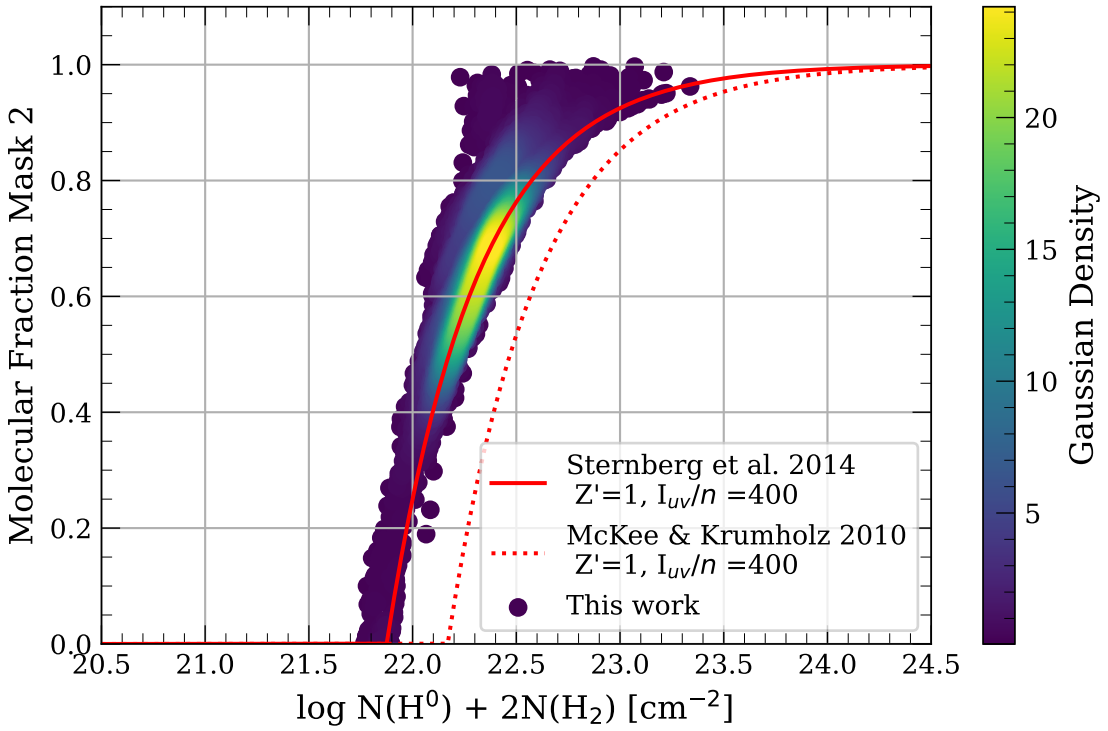

Figure 17. Molecular Fraction vs Dust Mask 2

Note: Molecular fraction f(H_2) plotted against column density from dust on a log scale as in Fig. 16, but this time for the pixels overlapped by mask 2 the denser region. These pixels correspond to the grey contour of Fig. 15. Here I_{uv} / n = 400 cm^3.

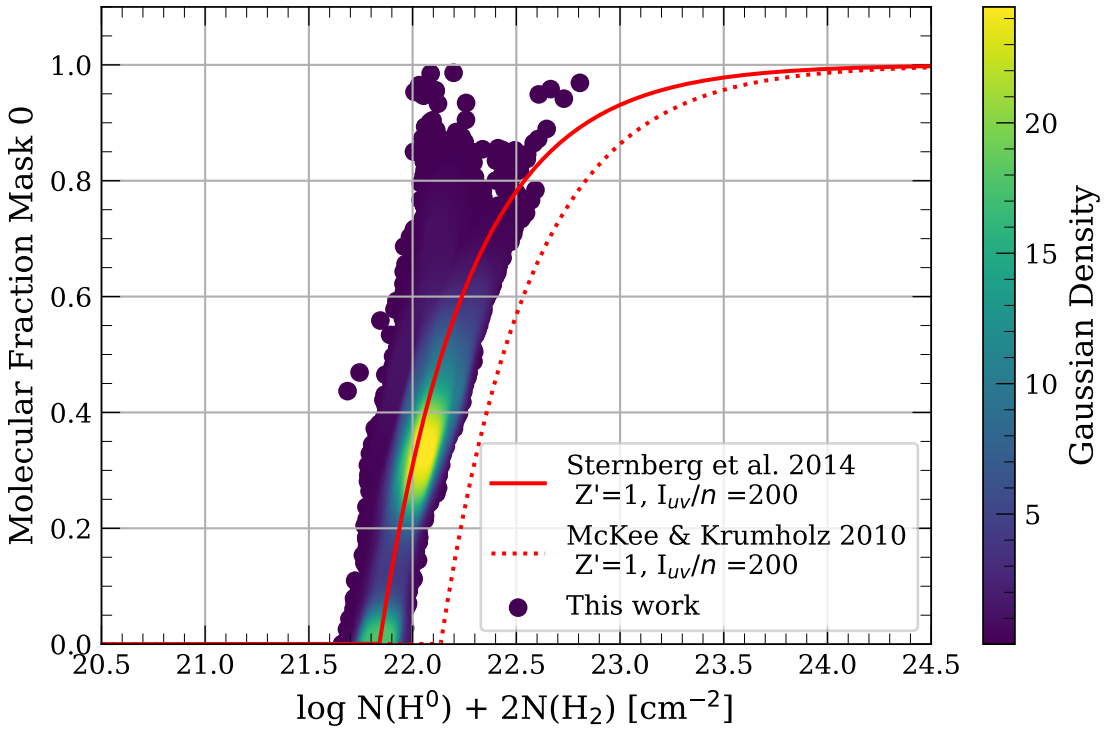

Figure 18. Molecular Fraction vs Dust Mask 0

Note: Molecular fraction f(H_2) plotted against column density from dust on a log scale as in Fig. 16, but this time for the pixels with no overlapping CO emission. These pixels correspond to the background outside the black contour of Fig. 15. Here I_{uv} / n = 200 cm^3.

Several estimates for the FUV field intensity are given by region in Wu et al. (2018) that range from $\sim 10^3$ - 10^4 which includes the well studied Trumpler 14 region with estimated intensity at 1.4×10^4 (Brooks et al. 2003). Estimates for the field intensity as a function of distance are presented in Smith (2006) and Roccatagliata et al. (2013) where the field is between 100 - 1000 as far as 10 pc from the center of Carina and nearly 10^5 in within clusters at a distance of 1 pc. It is worth noting that these values are in Habing units $G_0 = 1.6 \times 10^{-3}$ cm^{-2} s^{-1} while the I_{UV} is normalized to the Draine field which is $1.7 \times G_0$.

2.5.3 CO Dark Gas Prediction

In order to estimate the region of the Carina Nebula that will be CO dark one needs to compare how much material is traced by CO emission to how much material is found through dust observations. Both methods provide estimates for molecular hydrogen, however where CO is below detection limits, emission from the dust will still be present. In Figure 19 I added N_{H_2} pixels above 3σ with no CO overlap as a green Mask 4. The CO and N_{H_2} data have wider spatial coverage in galactic longitude than HI. Pictured in Fig. 19 is a qualitative mask 4, within the boundaries of which showed how CO emission alone was insufficient at determining molecular hydrogen. Data outside the green boundary fell below the background noise of the N_{H_2} image. CO emission was left outside the boundary to show that with wider dust observations even more of the molecular hydrogen could be hiding in CO dark regions.

For quantitative analysis only the area of coverage that coincides with all three data sets will be considered. The area of overlap for all data is detailed in Figure 20.

The overlapping region highlighted in black shows where HI, CO, and N_{H_2} pixels are coincident, and the white contour outlines ^{12}CO emission was added for reference. Using a distance of 2600 pc (Kuhn et al. 2019), the CDELT pixel increment of 30", and the mass of a hydrogen atom, the total mass in each pixel could be calculated and summed. There were uncertainties in the column density maps that were predominantly from the conversion factors X_{CO}, and X_{HI}. The values were estimated to within ± 30% (Bolatto, Wolfire, and Leroy 2013) for CO conversion factor, and ± 32% (Chengalur, Kanekar, and Roy 2013) for X_{HI}. This was partially due to the assumption that the conversion factors were constant throughout the entire nebula, when that was not likely the case. For the Mopra ^{12}CO data discussed in Section 2.3.1, $\sigma_{CO} \sim 10\%$ for a total uncertainty of ± 40% which is in approximate agreement with Figure 12. From that, the total mass of Mask 1, 2, and 3 from CO emission is $(3.65 \pm 1.46) \times 10^5$ $M_\odot$. Mask 4 has a total mass of $(2.13 \pm 1.34) \times 10^5$ $M_\odot$ that is not accounted for by CO emission. In other words between 22% and 39% of Carina is CO-dark. This coincides in the upper bounds with observations of individual clouds which are estimated to be ∼ 30% (Wolfire, Hollenbach, and McKee 2010), while the average for the entire MW was simulated to be between 42% to 46% (Smith et al. 2014). Variations along the line of sight can be from 12% to 100% in the most extreme cases (Liszt and Pety 2012).

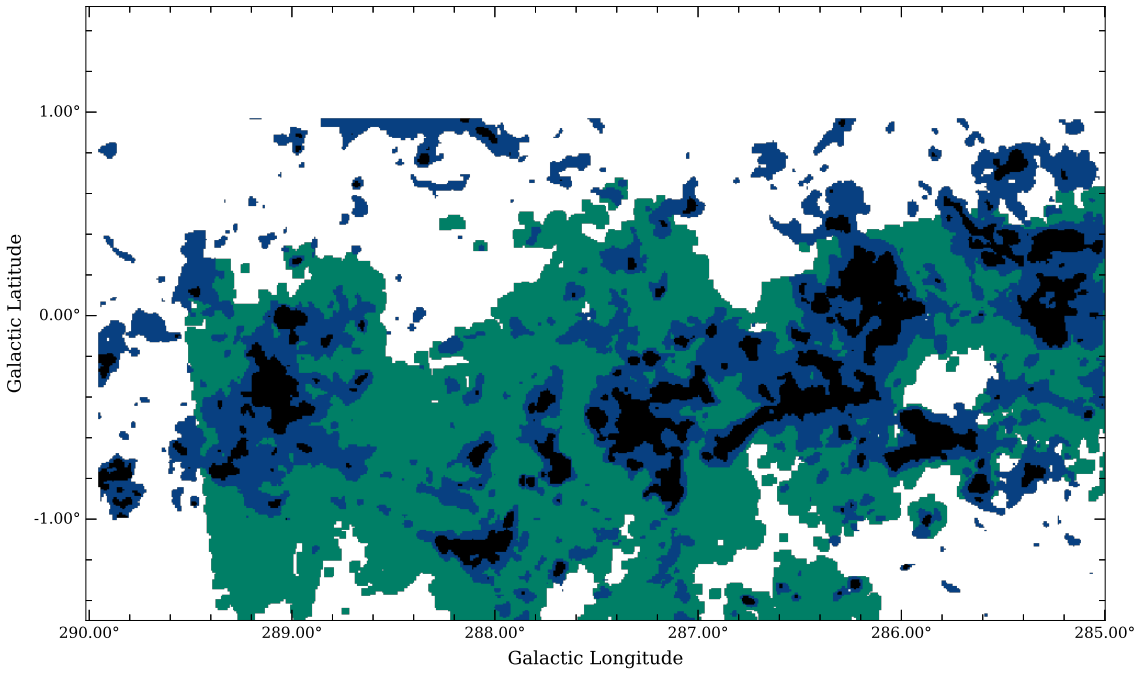

Figure 19. CO-Dark and CO-Bright Region Masks

Note: The masked regions of ^{12}CO seen in Fig. 8 where the pixels that detect only ^{12}CO are in dark blue, pixels with both ^{12}CO and ^{13}CO in black. In addition to those masks, a green masks is presented that identifies pixels with only N_{H_2} emission. This highlights the potential region of the Carina nebula where molecular hydrogen is not being traced by any CO line. Green mask boundary is at the noise floor for dust emission.

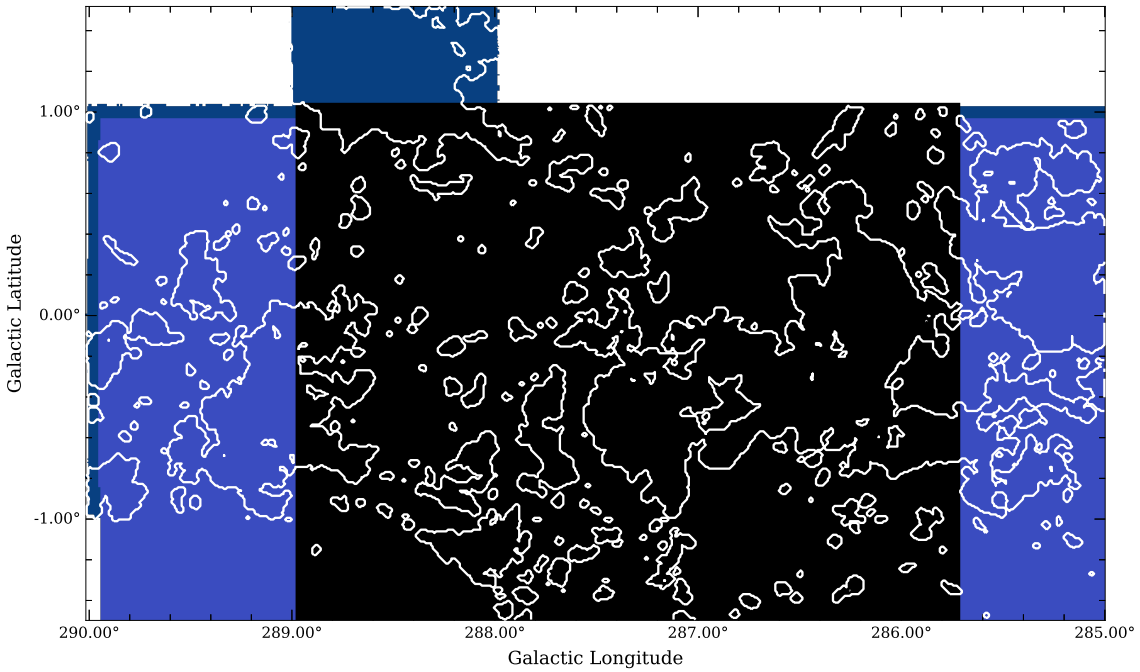

Figure 20. Map Boundary Image

Note: Overlapping masks of spatial coverage for all data sets used. The dark blue background shows the coverage of all the CO data cubes and is mostly covered by dust emission. In addition to the mask itself an outline of ^{12}CO emission above noise floor is outlined in white. The N_{H_2}(dust) map is in light blue. HI is masked in black and coincides with the approximate region of overlap for all three maps. This image is a qualitative illustration of how the different ranges in these data, set the bounds of the final molecular fraction f(H_2) map.

Table 2. Mass Distribution in Carina Nebula

M(H + H_2 + H+)	M(H_2)$_{CO}$	M(H_2)	M(H)	M(H+)
10^5 $M_\odot$	10^5 $M_\odot$	10^5 $M_\odot$	10^5 $M_\odot$	10^4 $M_\odot$
6.24 ± 2.71	3.65 ± 1.46	2.13 ± 1.34	3.67 ± 1.20	4.41 ± 1.74

Note: The mass budget of the Carina nebula by component.

Looking at the excess mass in column three of Table 2, it is obvious that there remains a wealth of CO-dark gas to be explored. These ancillary data sets for Carina fit well to the theoretical models based on standard assumptions for the nebula. However, estimates from ancillary data are just the first steps, with the next being direct observations. Both GUSTO and ASTHROS will make observations of the Carina Nebula. In the case of GUSTO, the main prediction will be that the singly ionized carbon maps produced in the survey will uncover an additional H_2 reservoir previously unseen in CO and possibly even some material that was missed by dust emission. From newer survey measurements, like those that will be attempted by GUSTO, updated gas mass estimates can be made. ASTHROS will deploy a more targeted approach to probe ionized gas, but ASTHROS also has some tuning capability to observe [CII]. While there is ample motivation for tuning, at this time, that remains outside its mission.

Repeating this type of ancillary data analysis for multiple sources and regions will further highlight the need for broader surveys in the THz range. ASTHROS target sources include TW Hydra, G33.6.0.2, and the M83 Galaxy. If sufficient ancillary data exists for those sources the same process carried out for Carina may be repeatable for the additional targets. Ultimately higher frequency, and higher resolution missions are needed and it will be up to the future generation instruments and astronomers to unlock the next era of ISM study.

Chapter 3

FLEXIBLE PRINTED CIRCUITS FOR IF SYSTEMS

3.1 Motivation for New Transmission Technology in THz Instruments

Until now I have only covered the science products of ancillary data for studying molecular clouds. Observations at terahertz frequencies are necessary for further imaging of the ISM. The remainder of my work is focused on the hardware and sub systems of THz instruments. As I mentioned in section 1.3.1, THz technology has only recently become viable. THz astronomy is in its infancy relative to other observing strategies. Most instruments have very low pixel counts like the STO which flew with 4 pixels for each line [CII], and [NII]. GUSTO itself has 3 arrays of 8 pixels each.

The raw signals are too high frequency to be read directly by electronics. The current state of the art for terahertz astronomy instruments is to transmit intermediate frequency (IF), or down-converted signals, via discrete sets of semi rigid coaxial cables. The cables transmit signal collected by individual pixels in a larger focal plane array and carries that data to readout electronics. Coax lines have a long history of use and predictable performance. As the pixel count goes up in an instrument so too does the count of individual coax lines.

A very popular and durable type of coaxial cable is the UT-085 stainless steel to stainless steel SS-SS coax which has an outer diameter that is 0.0865 inches (2.2 mm) and terminates with an SMA connector. Coax cables can be hand formed to meet limited geometries that allow them to be routed through an instrument. Even

for arrays of < 100 pixels, routing and assembly using individual coax cables can be very challenging since they take up significant physical space. Most astronomical observations at higher frequency require the use of cryogenics in order for their detectors to function. These systems require sophisticated vacuum chambers called cryostats to be able to maintain cryogenic temperatures. Cryostats are typically segmented by thermally isolated chambers known as stages that are shielded to help prevent thermal leak from ambient temperatures. Coax lines bridging the detector with the readout system must then be segmented so they can be thermally coupled to each stage. The coax exit the cryostat through vacuum sealed hermetic feed throughs. The connectors are typically individual coax through components. A blank flange is machined with small holes drilled for the feed throughs. The flange needs to be able to form a seal with typically an o-ring or copper gasket which limits how many feed-throughs can go on a blank. All of this adds cost to the overall system and as a result coax scales poorly for larger pixel counts. In order to accommodate future THz focal plane arrays of potentially 1000 or more pixels a new technology for transmitting signals needs to be implemented. I discuss some of the tools for describing transmission lines in section 3.1.1. In section 3.1.2 I talk about a potential coax alternative which was a prototype flexible transmission line ribbon. I talk about my additions to that original design in section 3.2. I then discuss how that design was implemented for a NASA mission in section 3.3.

3.1.1 Signal Transmission S-Parameters

Before I propose a new transmission technology I want to explain how we characterise devices and cabling. Transmissions for a broad range of frequencies

can be measured by a vector network analyzer (VNA). The VNA measures voltage differences between input and output signal ports and typically displays that data as an s-parameter. S-parameters are commonly used in RF electronics which can often have more than 2 ports. In Pozar (2011) they are defined as:

$$S_{ij} = \left.\frac{V_i^-}{V_j^+}\right|_{V_k^+ = 0 \text{ for k} \neq \text{j}} \tag{3.1}$$

The convention commonly used is that the negative sign implies signal reflected from a port, and the positive sign is from signal incident on a port. Meaning that S_{11} is found by driving port 1 with an incident wave of voltage V_1^+ and measuring the reflected wave amplitude V_1^- coming out of port 1. The incident waves on all ports except the jth port are set to zero, which means that all ports should be terminated in matched loads to avoid additional reflections. The transmission factor, other wise known as the gain for a two port device would be written as S_{21} (read out loud as: "S-Two-One"). S_{11} is referred to as the reflection coefficient, sometimes denoted as Γ. This has a special property of relating the input impedance seen at port 1 to the intrinsic impedance of the system.

$$S_{11} = \frac{Z_{\text{in}} - Z_0}{Z_{\text{in}} - Z_0} \tag{3.2}$$

Z_{in} is the input impedance, and Z_0 is some intrinsic system impedance typically taken to be 50 Ω. S_{11} and Z_{in} are complex numbers. S-parameters are given in units of decibels (dB) which converts power or voltage ratios from a linear to a logarithmic scale.

$$\text{dB} = 10\log_{10}\left(\frac{P_i}{P_j}\right) \tag{3.3}$$

Where P_i and P_j are units of power using the same convention as above. Some results are given in (dBm). A value in units of dBm means the power received by a load is $P_j = 1.0$ mW. One can express power in terms of voltage: $P = IV$. I is the variable for current, and V the electric potential or voltage. We can also make use of Ohm's law $V = IZ$ where Z is complex impedance. This results in $P = V^2Z^{-1}$. We can plug that back into the equations 3.3, recalling equation 3.1 and use the exponent rules for logarithms and equivalent impedance to get:

$$\mathrm{dB} = 20\log_{10}\left(\frac{V_i}{V_j}\right) = 20\log_{10}\left(S_{ij}\right) \tag{3.4}$$

This allows us to express the s-parameters in decibel form which makes certain math operations easier. A few more important terms to define here are the insertion loss (IL), return loss (RL), and isolation of a multi-port system. The insertion loss measures how much signal that was transmitted was not received or was "lost". This describes how much loss is attributed to actively inserting the device or interconnect into the system. For example in a two-port system the signal carried forward from port 1 to port 2 is S_{21} and the insertion loss is found by:

$$\mathrm{IL(dB)} = -20\log_{10}\left|S_{21}\right| \tag{3.5}$$

The convention here is to use a minus sign so that the value of IL is non-negative because the term loss already implies signal is being reduced by that value. Return loss measures the loss in signal power from the incident wave to the reflected one. Just like IL it is measured in dB and found from the s-parameter S_{11}:

$$\mathrm{RL(dB)} = -20\log_{10}|S_{11}| \tag{3.6}$$

Isolation on the other hand measures how much signal "leaks" or "bleeds" into an adjacent transmission path. It is also referred to as cross-talk. In a three-port device with active transmission S_{21} is non-zero but port three is terminated with a load, then there should be no transmission from port one to port three. i.e. S_{31} would be infinitely negative in theory but in practicality will be some very negative number. This will not be the case where transmission lines are very close to one another without sufficient insulating material or shielding. The concept of S-parameters give us the tools necessary to characterize and compare the performance of RF transmission lines.

3.1.2 Prototype Flex Lines

One potential solution for signal transport is to replace discrete sets of coax with a multi-channel ribbon that is flexible and easy to work with so that it can route through difficult spacing. A ribbon that does not require complicated feed-through systems to pass different cryogenic stages. A 16-channel flexible ribbon based on a stripline (Barrett 1955) architecture was developed by McGarey et al. (2014). A stripline is a transmission line similar to a coaxial cable as seen in Figure 21. The primary difference being that where the coaxial cable is round the stripline is flat or rectangular. A common analogy is that a stripline is just a coax that has been run over by a heavy truck. Striplines have a rectangular center that is the signal trace. Signal is sandwiched between an insulating dielectric material, and another layer above that which is a ground plane with the same conducting material as the signal trace. Striplines were developed as transmission lines for planar application in printed circuit boards with the benefit that they are better

isolated than alternative planar designs and therefor many striplines can be added to the same board with little interference from one another (Fromm 1955). This was a motivating factor for McGarey et al. (2014). While the bulk of their circuit was stripline based, ultimately the signal had to terminate in some type of connection to be measured. The original authors and testers simulated several designs with various terminations including stripline to microstrip, and stripline to radial transitions. Their best results came from a stripline to radial case. This simulation was created by tuning circuit elements over multiple layers. In the central layer was the signal trace plane, where the rectangular center conductor was terminated by a small circular mid pad. In the next two layers were the substrates which were unchanged. In the ground layers the copper was removed at the same position as the trace mid pad. This created an island where a circular anti-pad was resting on the exposed substrate. This part of the transition served as a land for connectors. A signal via was drilled through the center of the three pads. A series of 7 additional vias were rung around the anti-pad in a fence shape to control the signal transition from stripline to a radial coax. Because these were ground vias they had to connect the top and bottom ground layers. More details about the transition can be found in section 3.2.1 which gives the dimensions used in impedance matching. Impedance tuning of a stripline can be done by varying specific parameters such as the trace thickness, the width of the central signal trace, and the separation between the ground and signal layers. The manufacturing of the flex circuit put certain limits on the thickness and spacing so tuning for the main body was done with the signal strip. The radial transition could be tuned to impedance match by varying the width of the three pads, single mid, and two anti. The width of the signal vias and placing of the ground vias also contributed to these factors. Because of the radial transition,

the 16-channel design could make use of G3PO press on type connectors instead of the SMA which required hand tightening to achieve a mating connection. This meant that all 16 transmission lines could be connected in one single act. While the designers considered the first flex ribbon a success they did note improvements could be made. In order to fit 16 terminating connectors in such a small space the signal carrying transmission lines that run the length of the circuit had to be routed with sharp 90 degree right angle turns. The steep angle of these turns as apposed to a more gradual slope caused additional return loss. This however was anticipated and the original authors also made a smaller version of their ribbon with only four channels. The four channels were parallel straight line like the ribbon in Fig. 22. It was that in-line version of the flex ribbon that I used as the initial template for my own design.

Figure 21. Stripline vs Coax

Note: A very basic drawing of the cross-section for a stripline (left), and coax (right). Both operate on a similar principles with a center conductor for signal transmission through a dielectric substrate and conductor shielding. Actual coax will have several additional layers of physical and environmental shielding as well. The stripline is generally used for planar circuit board RF transitions.

3.2 Eight Channel Design Goals

The original flex circuits achieved many of their design goals. The ribbons carried RF signal across multiple channels with little to no cross-talk. They were significantly more flexible than coax. Connections were easy and quick to make. The transmission performance of the ribbon was comparable to that of coax when the ribbon was at an operating cryogenic temperature. The four channel ribbon improved upon the return loss from the 16 channel variant. The ribbon was compact and light-weight. How to scale the technology up to higher trace count, and improve the form factor of the ribbon were of high interest to me. The flexible material itself was a Kapton substrate made on Rogers material boards. The ground and signal traces were copper. The copper ground plane was extended to the full width of the ribbon so all the buried signal traces would share the same ground. If the signal traces were well isolated however, there would be no need for the full copper plane to extend the entire circuit. Rather, a pattern could be traced out of the top and bottom planes such that only narrow strips remained above and below the signal traces. The question I had to answer was how narrow the ground plane could be and still function as a stripline. This reduction would not only improve the flexibility of thee ribbon overall, but also reduce the heat-load of the cable. Considering some missions operated with a limited supply of coolant, reducing the amount of heat entering the system would be key to extending mission life time. Some cryogenic systems will require very complicated routing paths for the flex ribbons. Another goal of mine was to determine a safe bending radius of the flex so that when the ribbons are designed for a custom mission they can be safely routed through narrow spaces and avoid the sharp angle turns that plagued the 16-channel ribbon. The

following section 3.2.1 goes into detail about the simulation of general purpose flex ribbons as well as the proof of concept for the reduced ground plane. Examples of custom designs for the GUSTO IF harness are discussed in section 3.3, and the designs for future missions are in section 3.4.

3.2.1 Eight Channel Simulations

The first generation flex circuit consisted of multiple IF channels embedded in a Dupont 8545 Kapton substrate that was 4 mils, or 4 thousandths of an inch (0.10 mm), thick on each side. The Kapton was plated with 1/2 ounce copper roughly 0.8 mils (0.02 mm) thick. The circuits had a radial coax like transition in their central conductor to break out the signal traces from the buried Kapton layers. This allowed them to have surface mount connectors on both ends. Hot vias were used through the board layers. The via was essentially a hole drilled through the circuit board. A conducting material or solder is used to plate the hole so there is a physical conducting path between the bottom and top layer that the via is added to. A hot via is a term for a signal carrying via. The alternative form is the ground vias which were used to ensure top and bottom layers of ground were indeed the same ground. The separation between channels was initially 0.232 in (6.00 mm). I began simulation work using this as the starting point.

The new circuits were simulated using 3D EM analysis software CST Studio Suite. I began by modeling three 50 Ω stripline transmission lines in the same substrate. Impedance matching is an important concept for RF design. The impedance of two interfacing components must be the same or there will be reflections in the form of

standing waves as the signal sees the impedance mismatch. It is customary in RF design to match connections to 50 Ω.

An in-line arrangement like the one seen in Fig. 22 was easier to draw and simulate. This approach however was quickly abandoned as I realized a staggered array would make the width of the circuit more compact while still fitting a minimum of eight traces. This would bring the traces closer together and increase the risk of cross-talk. Understanding the effects of reducing separation between signal traces is the first step toward increasing the number of channels per flex ribbon. The closer I could fit the channels together the more channels I could ultimately fit on a single ribbon. The initial channel spacing was set to 0.24 inches (6.1 mm) and simulated. The spacing was reduced by increments of 0.01 in. The insertion and return loss over a 5 GHz bandwidth were virtually unchanged even at 0.05 inches (1.3 mm) separation between traces. The channel spacing was then chosen to be 0.12 inches, or 120 mils ($\sim$ 3.0 mm). This was because the signal traces would transition out to surface mount connectors. Leaving extra spacing at the connector sites would make hand soldered assembly easier and this would also accommodate several different connector types to give more options.

Figure 22. Four Channel In-Line Prototype Cable

Note: In this image we see a pair of four channel in-line flex cables using one of the original designs by McGarey et al. (2014).

The total width of a straight 8-channel circuit was 1.1 in (2.8 cm). To radially transition out of the stripline, the trace was terminated by a 0.04 in (1.0 mm) circular pad, with a plated through hole 0.006 mil (0.15 mm) signal via at the center to escape the substrate. Through hole vias were chosen over blind to reduce the fabrication cost of the circuit. A 0.03 in (0.76 mm) anti-pad connected the hot vias to the surface and was set by the size of the central conductor. This anti-pad matches the center conductor size of several surface mount SMP type connectors. Ground vias are implemented in a semi circle fence around the anti-pad to complete the transition. CST Studio Suite simulations were used to optimize the transition impedance to 50 Ω. The field lines behaved as expected for a radial transition, and the impedance was calculated to be 49.9 Ω at 2.65 GHz, roughly the center frequency for a 5 GHz IF bandwidth as shown in Figure 23.

A three channel version of the flex ribbon using this geometry was simulated in CST. Four ports at the connection sites were used in the simulation. Simulation port 1 was placed at the connector site of the incident signal, and port 2 the output. Ports 3 and 4 were defined at the adjacent channel connections. Simulations of only three channels was more desirable, as the computation time for simulating the full 8-channel version was on the order of days. The length of the flex circuit was simulated at 20 in (0.51 m). Using four ports allowed for the simulation of insertion loss, return loss, and isolation in the same simulation run.

The RF design goals for the prototype were to achieve an insertion loss < 6 dB per ribbon length at 5 GHz, return loss of 20 dB or greater over the bandwidth, and negligible cross-talk between signal traces, some $\leq$ -50 db. The simulated results of a signal trace and two nearest neighbors are shown in Figure 24. The insertion and return loss were at acceptable levels, and the isolation between channels was

very promising at 70 dB or better for the full bandwidth. The simulation was done without a lossy substrate, but the copper was edited to have an increased conductivity that simulated cryogenic temperatures. Insertion loss was expected to be worse for the real circuit and for room temperature measurements.

Flexible ribbons have inherent advantages over coax when complicated routing of transmission lines within an instrument are needed. Kapton substrate is extremely durable and allows for dramatic bends and turns out of the plane of the flex circuit. In plane bends were problematic for the first generation flex circuit. In order to solve this problem I introduced a gradual bend in one end of the transmission line where the innermost bend radius of the ribbon is no less than 1 inch (25 mm). A 3D model made in CST of the straight varient can be seen in Fig. 25, and the curved circuit can be seen in Fig. 26

The next design goal of particular interest was reducing the overall heat load of the flex circuit. One option for this was to reduce the metal content of the flex circuit, in this case the 1/2 ounce copper layers. The dimensions of the radial center conductor were already optimized for achieving the right impedance so, the only copper that could be removed had to come from the top and bottom ground layers. Reducing the copper cladding to 1/4 ounce copper would improve heat load, but result in more expensive fabrication cost. A significant reduction in heat load could still be achieved by cutting a pattern into the ground layers. That changed the top layer from a full-plane ground to one of thin strips that rest on the substrate just above their respective signal traces. This still allowed for stripline based signal transmission for the individual channels. The narrower the ground strips could be the more the heat load would be reduced.

Table 3 shows the analysis of the heat load for the flex circuit with different

width ground stripes and how they compare to SS-SS coax. UT 85 is the most commonly used coax, with UT 47 used as a substitute when there is less space to work with. UT 20 is also used to conserve space but less frequently since it has an outer diameter of 0.023 in (0.58 mm) making it much easier to break. For these reasons the metric for comparison was the heat load of UT 85. The chart shows that despite the fact that copper is more conductive than stainless steel, reducing the amount of conducting material in a cross section of the transmission line can give equivalent or better heat load.

Table 3. Thermal Calculations and Comparison of Flexible Circuit to SS-SS Coax

Circuit Type	Cross Sectional Area (m^2)	Thermal Load (WmK^{-1})	Ratio to UT 85
Flex(15 mil)	1.70×10^{-8}	6.83×10^{-6}	0.25
Flex(25 mil)	2.74×10^{-8}	1.10×10^{-5}	0.41
Flex(260 mil)	2.70×10^{-7}	1.08×10^{-4}	4.01
Coax(UT 85)	1.66×10^{-6}	2.70×10^{-5}	1.00
Coax(UT 47)	5.98×10^{-7}	9.75×10^{-6}	0.36
Coax(UT 20)	9.89×10^{-8}	1.61×10^{-6}	0.06

Note: Thermal conductivity of stainless steal is 16.3 $WK^{-1}m^{-1}$, and for Cu: 403 $WK^{-1}m^{-1}$. Thermal analysis shows the narrowest ground stripes far surpass industry standard UT 85 coax in heat performance.

The narrowest ground strip width that was considered was 0.015 in (0.38 mm). This was set as the limit since there was a danger of misalignment between the ground strip and signal trace during fabrication if they became comparable in width. There was also a risk of misalignment of the width of the ground strip approaches the manufacturer tolerances. The stripline width was 0.003 in (0.076 mm). CST simulations of reduced ground planes showed a negligible change in loss even with ground strip widths as narrow as 0.01 in. This was too close to fabrication tolerance. Three widths were chosen for the prototype. There were 15 (0.38 mm) and 25 mil

(0.64 mm) ground strips and a full ground plane variant. In addition, a copper tab was added to the design of the striped flex circuits so they could be heat sunk to a cold plate. This was not needed for the full ground version because they could have a heat sink soldered to any part of the main body as it had no reduced metal surfaces. Fiber glass composite material FR-4 was used at the ends of the flex circuit to provide rigid support for the connection sites only. Multiple version of the flex circuit were designed and sent for fabrication. Each design highlights a feature from the above simulations that needed to be experimentally validated.

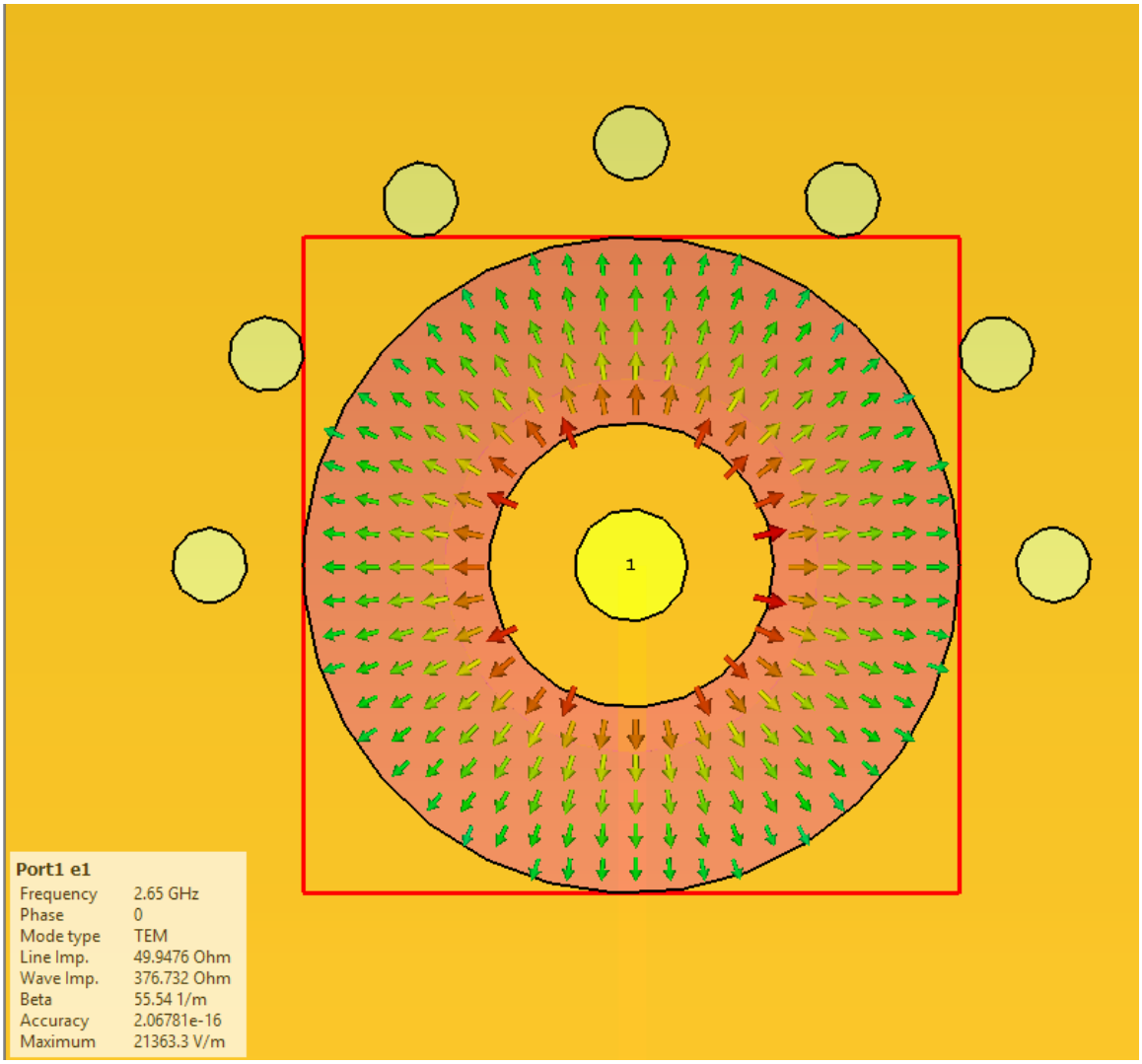

Figure 23. Radial Transition Simulation

Note: CST simulation of the radial transition from the stripline. Seen at the top layer of 1/2 ounce copper this is the assembly site for the surface mounted SMP press on connectors. Also seen is the propagation of EM fields through the Kapton substrate, and the calculations for the port impedance. Simulations were done over a 5 GHz bandwidth.

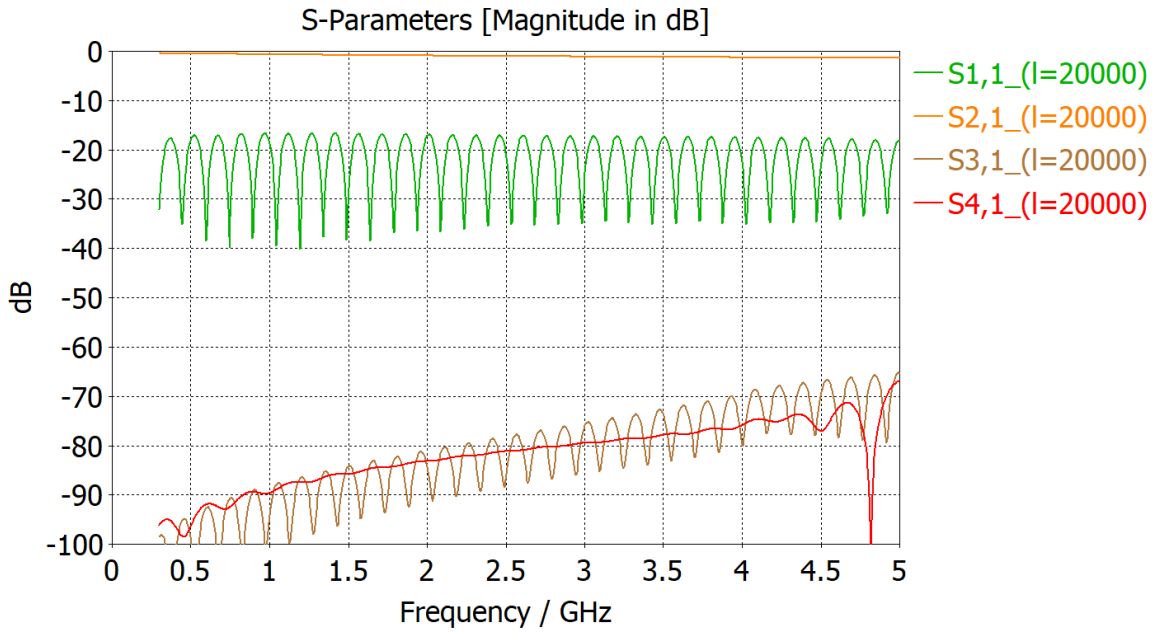

Figure 24. Eight Channel CST Simulation

Source: Neric et al. (2019)

Note: CST Studio Suite Simulated transmission characteristics of a three channel flex ribbon. Input signal was from port 1 to port 2. Ports 3 and 4 were the nearest neighbors and used to simulate isolation. Design goals for insertion loss (< 6 dB), and isolation (> 30 dB) are met according to software.

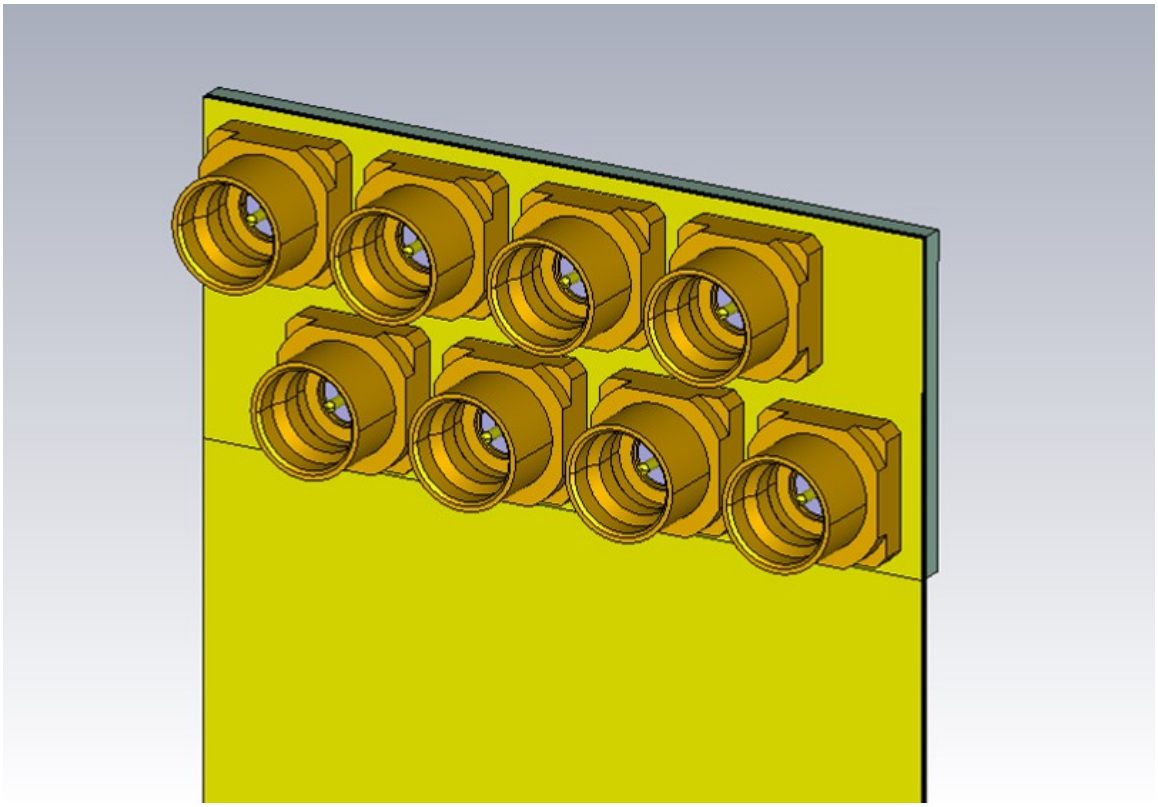

Figure 25. Eight Channel Staggered Prototype Cable

Note: A flex circuit in CST with a staggered array to make it more compact than the in-line versions.

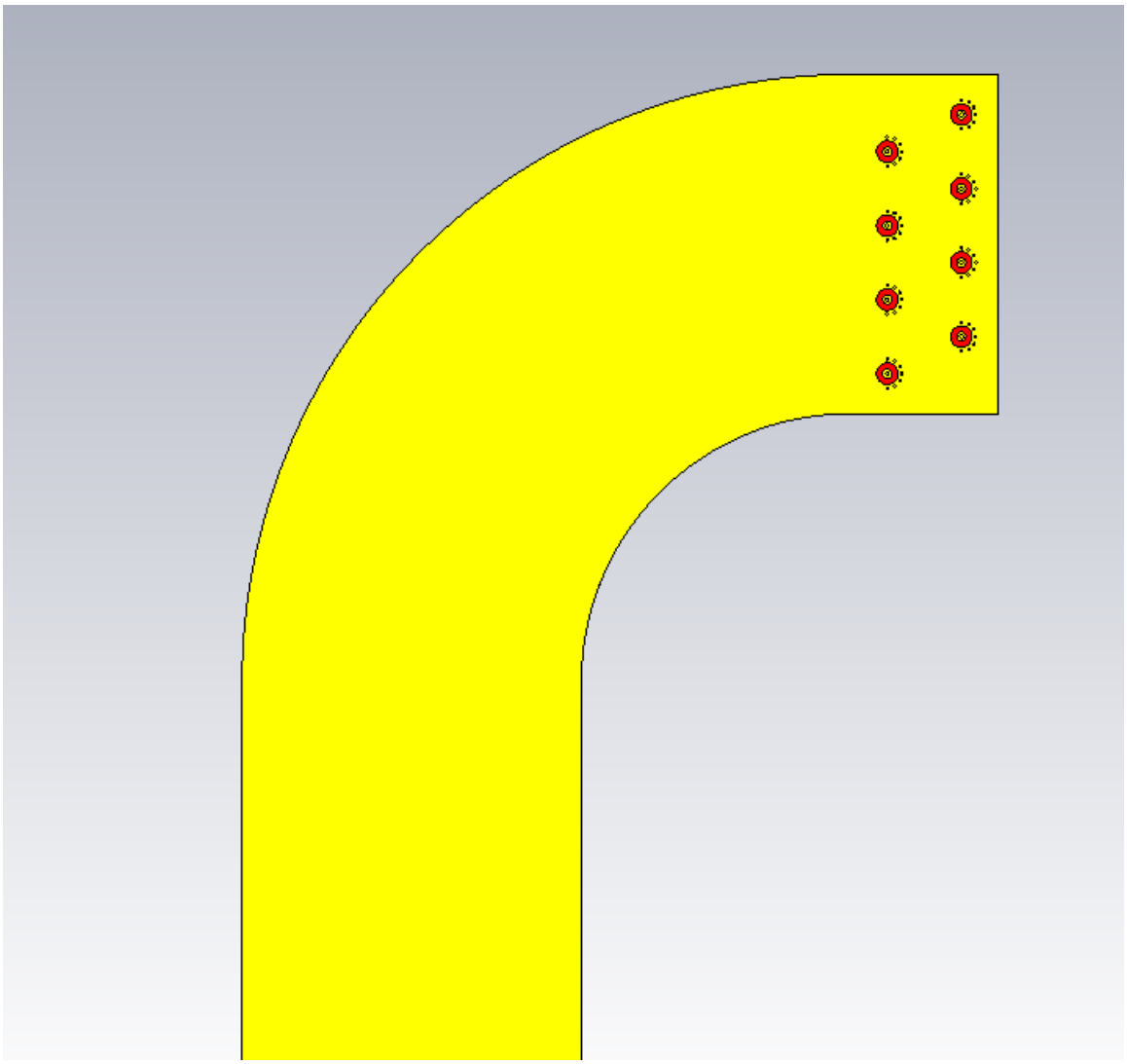

Figure 26. Flex Circuit with Bend

Note: CST model of an 8-Channel flex circuit that has a gradual curve design. Effective for unique routing, and otherwise identical to the staggered 8-channel circuit. This diagram does not show the connectors only the anti-pad connection sites.

3.2.2 Initial Testing and Results

Six versions of the flex circuit were fabricated by Coast to Coast Circuits, Inc. at their California facilities. Three of the flex circuits were staggered 8-channel single ribbons with no bends. The full length of an individual ribbons was 20 in. One board had full ground planes, another had its ground striped down to 25 mils. The last one had ground strips of 15 mil width, see Figure 27. Each of the striped flex circuits had an extended T-shaped copper tab that would serve as a heat sink. Another set of three flex circuits were made with full ground, 25 mil, and 15 mil ground strips, but these had a gradual curve at one end.

The full ground circuits were tested first in order to get comparison data to the striped version. Limited detent Amphenol RF SMP connectors were hand soldered to both ends of two channels (4 ports). The limited detent indicating a stronger than normal retaining force when the connectors were inserted. This was enough to test transmission, return loss, and isolation. For the room temperature test a Rhode & Schwarz ZVA 24 Vector Network Analyzer (VNA) that was calibrated with a ZV-52 electronic calibration module was used for RF measurement. The calibration was done with 0 dBm test power, and averaging set to 16 times. Mini-circuits 18 GHz coaxial cables with SMP adapters were used in the calibration and testing. Data was taken from 0.3 to 5.0 GHz. Results can be seen in Figure 28.

Room temperature testing of the flex circuits showed that the ribbons with 15 mil ground had an insertion loss at 5 GHz that was only 0.3 dB worse than the full ground case. The result was a 6% difference in power. An RF system can make use of several amplifiers in its chain that would produce more than enough gain to correct for this. Considering the overall heat-load improvements, the small loss was

otherwise more than acceptable since the 15 mil ground case would conduct 25% of the heat of a UT 85 coax. Since the flex circuits were designed for use in a cryostat, the follow up performance test needed to be done at cryogenic temperatures that resemble possible test conditions.

The limited detent connectors were problematic in testing since they required a lot of force to demate SMP connectors. The bullet adaptor that links SMP connectors would tend to detach from the test instrument and remain in the flex circuit. A special tool was required to remove the adapters without damaging them. Smooth bore SMP connectors were considered as a viable replacement option that offered ease of removal. It was anticipated that the smooth bore connectors would benefit from a clamp to hold connection sites together in moving instruments.

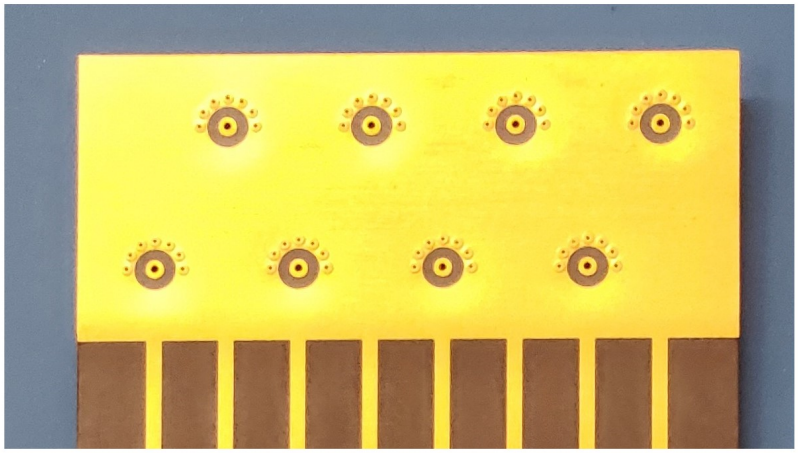

Figure 27. Eight Channel Staggered Ribbom

Note: Here is pictured a flexible circuit ribbon with eight stripline based channels terminating in radial coax transitions. The copper stripes seen on the top layer of the ribbon are the ground planes. The signal traces are buried underneath. SMP press on connectors can be soldered to the radial transitions at the central anti-pad which has a through via that extends through the board into the signal trace.

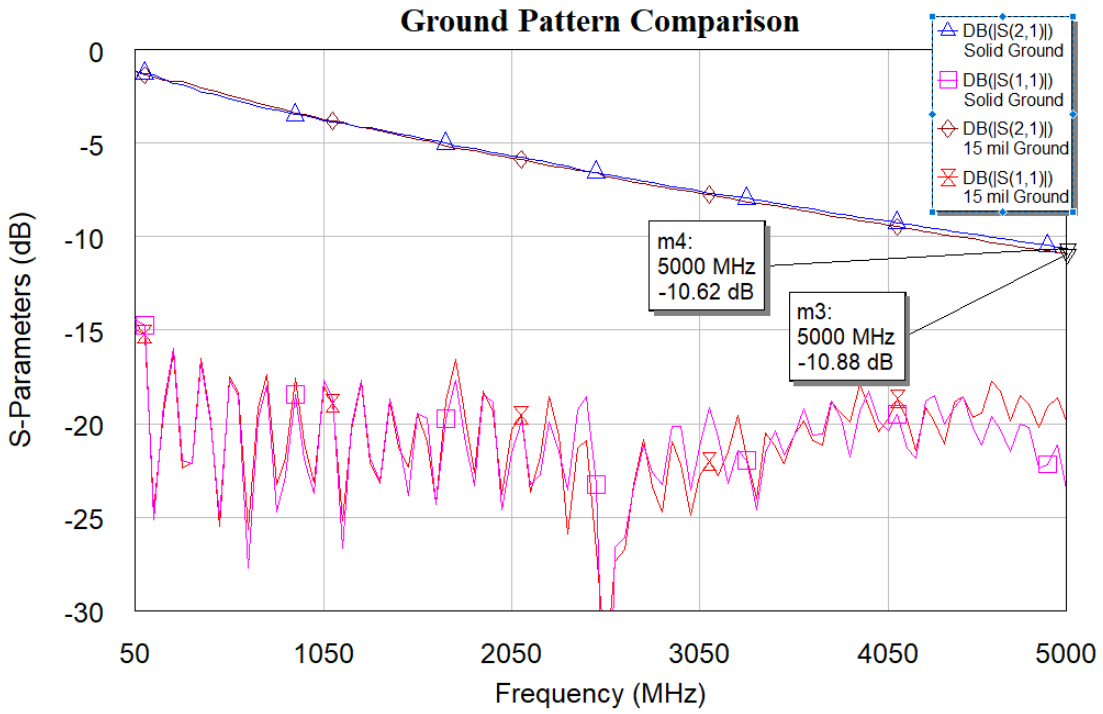

Figure 28. Ground Plane Comparison Measurements

Source: Neric et al. (2019)

Note: Room temperature transmission characteristics of a 8-channel straight flex circuit with SMP connectors. The two measurements include one circuit that has a solid ground plane, and a flex circuit with 15 mil strips in lieu of a single plane. The maximum loss at 5 GHz is only 0.3 dB which corresponds to $\sim 6\%$ loss in power. This is easily corrected for using low noise amplification.

Cryo testing was done in a 10 K closed cycle cryogenic test chamber. Vacuum flanges were machined with a slit for the flex circuit to be fed through. The opening in the flange was only slightly larger than the flex circuit dimensions. Here we can see another major benefit of the flex ribbon. I previously mentioned (section 3) that routing coax lines through the heat shields of a cryostat were made more complex by the need to install expensive hermetic feed-throughs for each cable. The flex circuit could be bonded or encapsulated into the flange using commercial off the shelf bonding material. 3M 2216 epoxy adhesive was used to seal the flex circuit into the flange. It was easy to mix and work with and could bond directly to the ribbon without impacting RF performance.

The test environment was brought down to 20 K temperature. This test bench was capable of reaching 10 K temperatures, however for most missions the flex circuit operating temperature would be a higher value. Figure 29 shows the setup before cool-down. The flex circuits were potted into a vacuum flange. A copper braid heat strap was soldered to the heat sinking tab on the flex circuit. The braid was then clamped to the 10 K test stage by a copper bracket. Channel one of the VNA was used as the input and connected to channel one of the flex circuit using a short SMA-SMP adapter. The other end of the flex circuit was not potted so it remained inside the cryostat. The output was read at channel two of the VNA through a stainless steel coax line with another SMA-SMP adapter, and an existing hermetic feed through on the test bench.

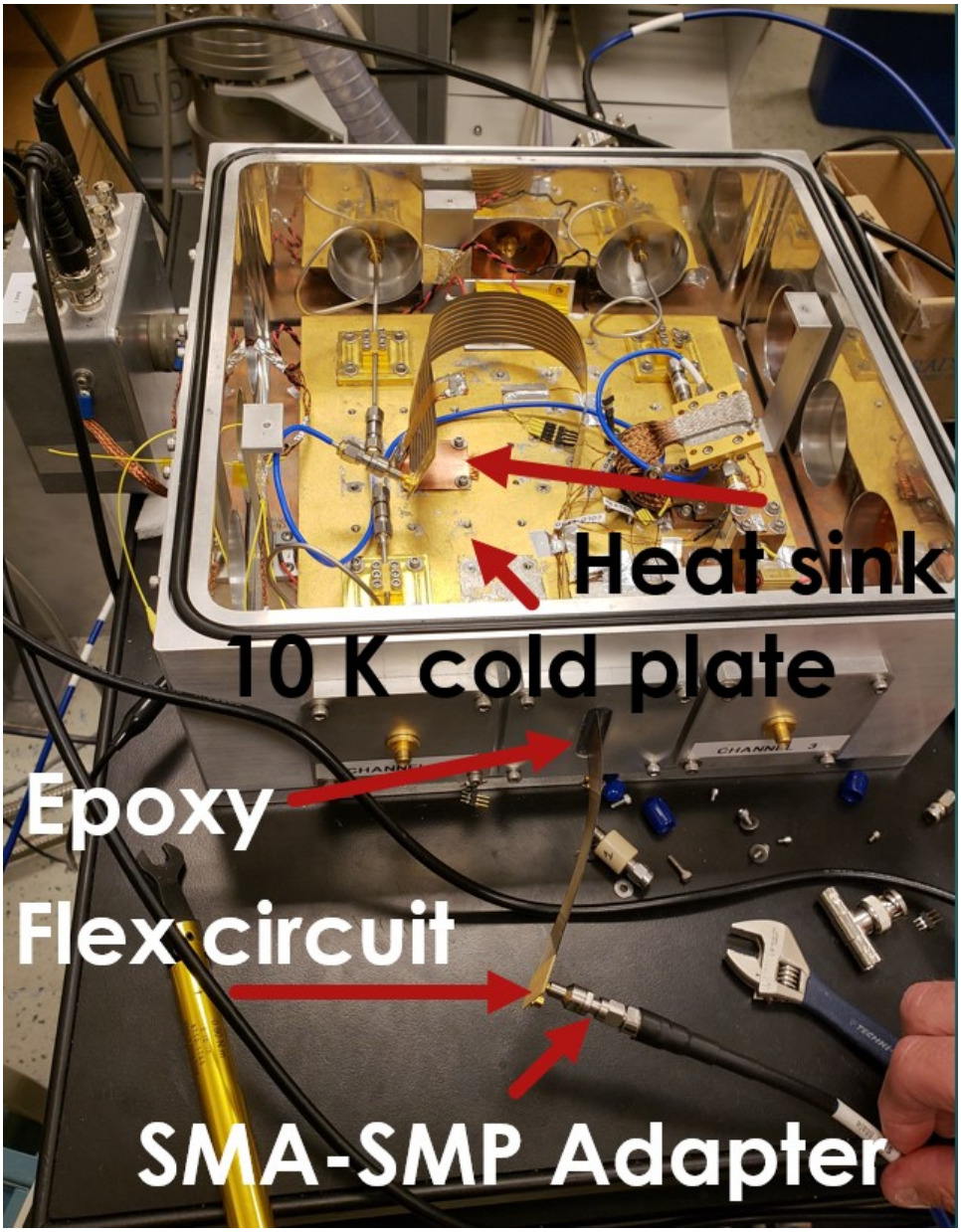

Figure 29. Cryostat Setup

Note: Test bench setup of 10 K cryogenic vacuum chamber. Flex circuit is inserted through a vacuum flange and potted with epoxy. VNA leads were attached to opposite ends of the same channel to capture insertion and return loss. A 50 Ω load terminated the adjacent channel.

Figure 30 shows a plot of the 15 mil flex circuit under the above test conditions. The insertion loss of the flex circuit at 5 GHz was 3.5 dB/ft. Other parameters remained nominal even at cryogenic temperatures. The system was left to run overnight, and then cycled several times with the circuit installed in the cryostat. There was no noticeable change in performance. This was slightly worse IL performance than the UT-85 coax (2.83 dB/ft) at the same frequency. Regardless, the benefits gained from enhanced routing capacity, reduced heat-load, and overall cost savings were more than enough to persuade three future missions to use the flex in their IF. Now that a general purpose design had been validated with measurement, I could apply this as a template to an actual mission. The first one I will discuss is the IF harness for GUSTO. The catch now would be fitting the circuit parameters to match that of a NASA regulated mission.

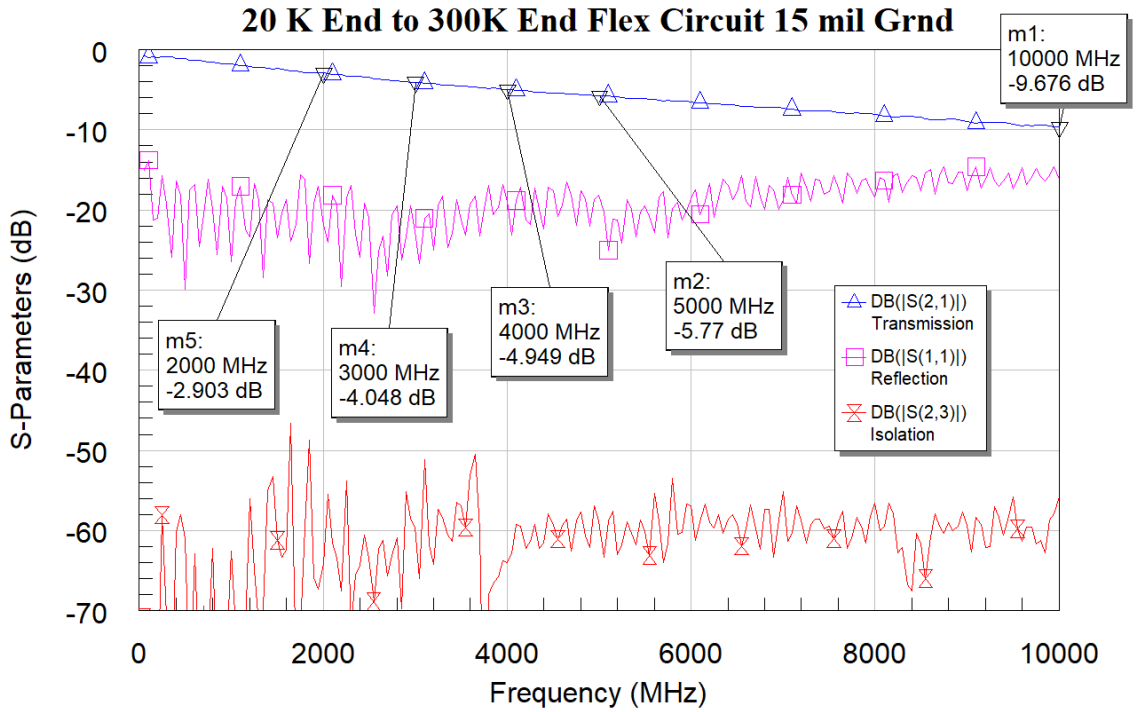

Figure 30. Flex Eight Channel Cryo Test

Source: Neric et al. (2020)

Note: Transmission characteristics of an 8 channel, 20 inch long flexible circuit. The circuit was measured with 1 mW input power delivered to one end inside a cryogenic system held at a constant 20 K temperature, while the output was read at 300 K. The insertion loss of the flex circuit is 5.77 dB at 5 GHz, making the loss 3.5 dB/ft at 5 GHz. The return loss at 20 dB shows that only 1% of the incident power is being reflected back to the input port over a 0 – 6 GHz bandwidth, and a maximum of 3% reflection beyond 6 GHz. Despite the very close 0.12" spacing between channels in the flexible ribbon, the cross talk is negligible at $<$ -50 dB meaning there is sufficient shielding between traces within a single ribbon.

3.3 GUSTO IF Harness

GUSTO will make use of heterodyne techniques like those discussed in 1.3.1. This requires an incoming high frequency signal to be mixed with a user provided signal of similar frequency via a local oscillator (LO). The mixing of the incoming signal (in this case light from distant sources commonly referred to as sky beams) with an LO signal will create a modulated response. The response is filtered so only the desired difference frequencies are collected. The resulting signal is the IF band.

There are multiple components to an IF harness starting with cryogenic wide-band low noise amplifiers (LNAs) (Weinreb, Bardin, and Mani 2007). Since the incoming signals from these distant sources are generally very weak by the time they reach the instruments, there is a need to amplify the incident power. Ideally that power amplification will be stable over the desired bandwidth and introduce as little noise, or uncertainty in the incoming signal as possible. GUSTO will use LNAs operating over a bandwidth of 0.3 - 5.0 GHz. This will cover the IF of all three spectrometers on the instrument. One spectrometer per observing frequency [CII], [NII], and [OI]. The amplifiers were designed and tested at ASU by Hamdi Mani and built by him and Justin Mathewson (Mani and Mauskopf 2014).

Part of the IF harness will rest on a 20 K stage of GUSTO's airborne crysotat while the other end exits the cryostat into warm low noise amplifiers. This is because the non-linear device that is responsible for down-converting the THz sky beam to the 0.3 - 5 GHz IF band is a superconducting hot electron bolometer (HEB) mixer. I will discuss this device further in section 4.1. The signal must be brought out of the cryostat via transmission lines.

Two choices for the transmission lines of the harness were considered. The

first was 24 sets of stainless steel - stainless steel (SS-SS) semi rigid coaxial cables. The benefits of semi-rigid coax include their well characterized performance, and their repeated use in commercial and space applications which gives coax a long heritage. Stainless steel is often chosen for transmission in and out of vacuum cryogenic systems due to its low thermal conductivity despite more signal loss than alternatives like copper. The drawbacks to using coax were discussed in section 3.1. They become more evident as the pixel count in an instrument increases. The resulting increase in pixels requires an increase in transmission lines. For a system using coax this means each cable must be individually installed to the same specifications. This increases the risk of individual failure while also increasing the overall form factor of the harness and installation

The second option considered was to make the IF harness using the new ASU cryogenic flexible transmission line ribbons. This quickly became the obvious choice since they could be custom designed to meet the specific routing needs of the mission without significant signal loss. The prototypes in section 3.2.2 achieved similar RF performance to coax, and transferred significantly less heat into the cryogenic system. The drawbacks to this approach are that the best RF performance was achieved when the ribbon was at cryogenic temperatures, and that was slightly higher in signal loss than SS-SS coax. The GUSTO LNAs were designed to adjust for this.

The LNAs for each of GUSTO's three 8-pixel heterodyne arrays would be installed in a specially designed enclosure housings. These enclosures included 8 LNAs and a breakout board for DC and RF paths. Each individual LNA would need 4 DC lines and a single RF output. The RF paths on the breakout board were striplines that meander from the LNA output, and terminated in a series of closely

spaced SMP connectors. The SMP connectors would mirror the flex circuit channel spacing. This would serve as the attaching point for a flex circuit. A picture of the enclosure is shown in Figure 31. The use of the flex circuit and breakout board with embedded paths over traditional cabling allowed for a very compact system.

In the following sections I go over the assembly and testing of the flex circuit tailored to meet GUSTO's complex routing path and other design constraints. Due to the fact that GUSTO was classified as a space mission many of us had to be specially trained for the assembly of space hardware. We were required to be certified before even handling the flight equipment. Each of us is an IPC J-STD-001 certified specialist in: soldered electrical and electronics assembly and space application electronics hardware. All assembly and testing was done inside a class 100 clean room. For the work discussed in section 3.3.3, I required an additional certification: NASA-STD-8739.1 Operator/Inspection certified for polymeric application on electronic assemblies for encapsulation and bonding.

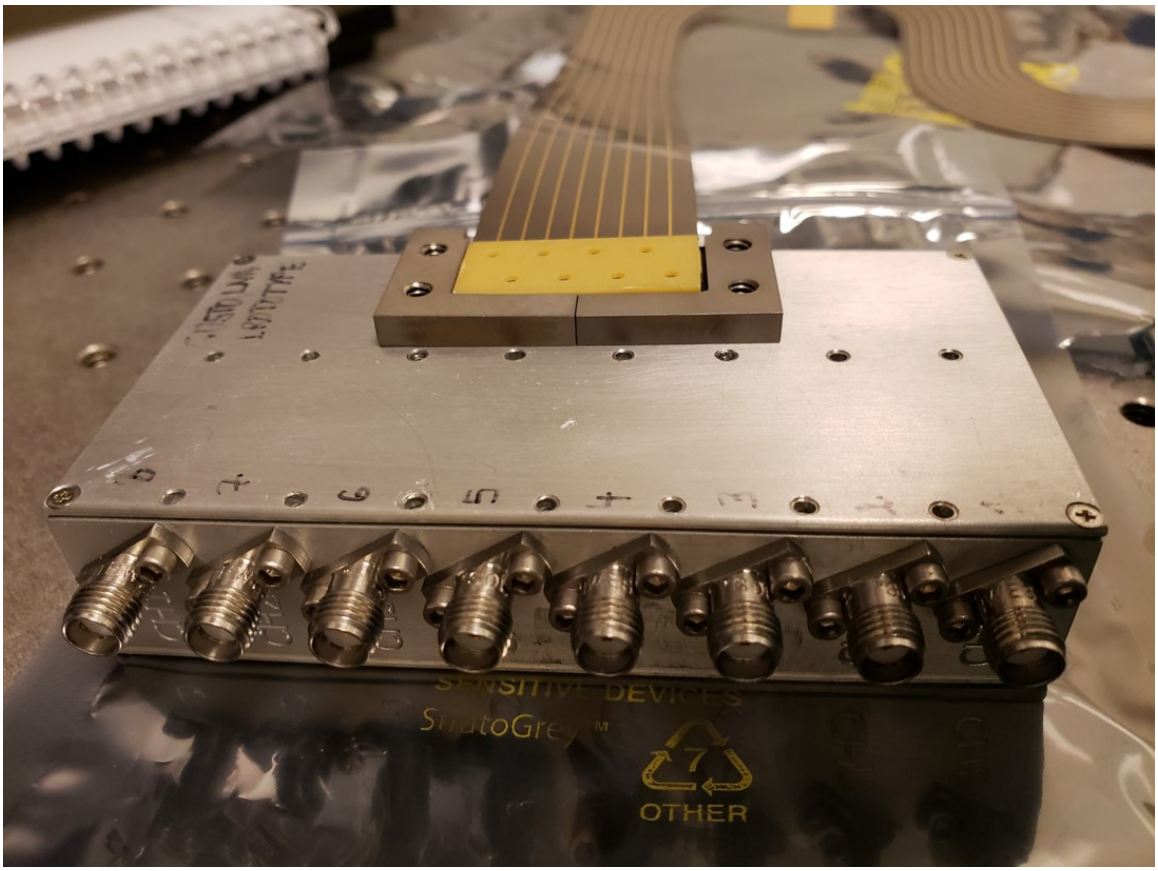

Figure 31. Flex Line with LNA Enclosure

Note: Custom designed eight channel flexible printed circuit board attached to an LNA enclosure box housing 8 cryogenic wide-band low noise amplifiers. This is the Cold IF for one of GUSTO's three heterodyne receiver bands.

3.3.1 GUSTO Flex Circuit Design

The limiting size of the individual flexible ribbons was the size of the panel which the flexible printed circuit material was made from. These had a working area of about 18 inches x 20 inches. To mitigate cost it was advantageous to fit as many flexible ribbons on the same panel as possible. The average length of GUSTO's IF bands was 3.30 feet and each band took a different path inside the cryostat. For these reasons, a single ribbon could not comprise the entire harness. Instead each of the three IF bands was made of two flex ribbons. One ribbon designated a "cold" circuit because it is held closest to the 20 K stage of the cryostat, and the other known as the "warm" circuit which would interface with the outside of the cryostat. The cryostat designed for the GUSTO mission had a particularly challenging path the IF harness needed to go through. Based on what I learned in testing the general purpose design in section 3.2.1, the flexible transmission lines were custom designed with short in-plane turn radii. This resulted in 6 uniquely shaped ribbons. Figure 32 shows a rendering of the GUSTO cryostat and the installed IF bands. Figure 33 shows the reference design for one of the cold circuits. This circuit would have to bend and fold to make its final path through the cryostat, but the same structure could not be possible with traditional coax.

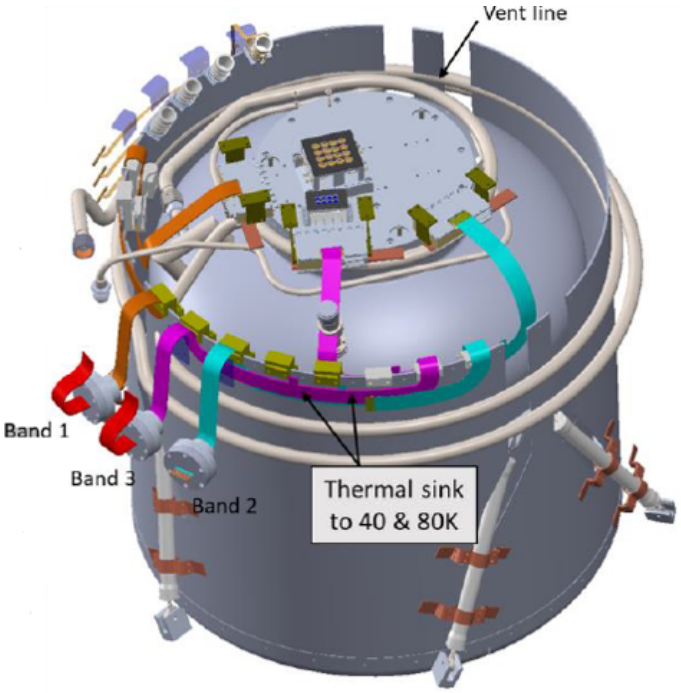

Figure 32. GUSTO Cryostat IF Route

Source: Neric et al. (2020)

Note: This image of the GUSTO cryostat demonstrates how complex the routing of the IF harness will be. The custom designed flex circuits are shown as bands 1-3. Flexible transmission lines simplify the install process since the ribbons snap together to complete 8 signal paths whereas the same system would have needed a minimum of 24 discrete semi-rigid coaxial cables for the task.

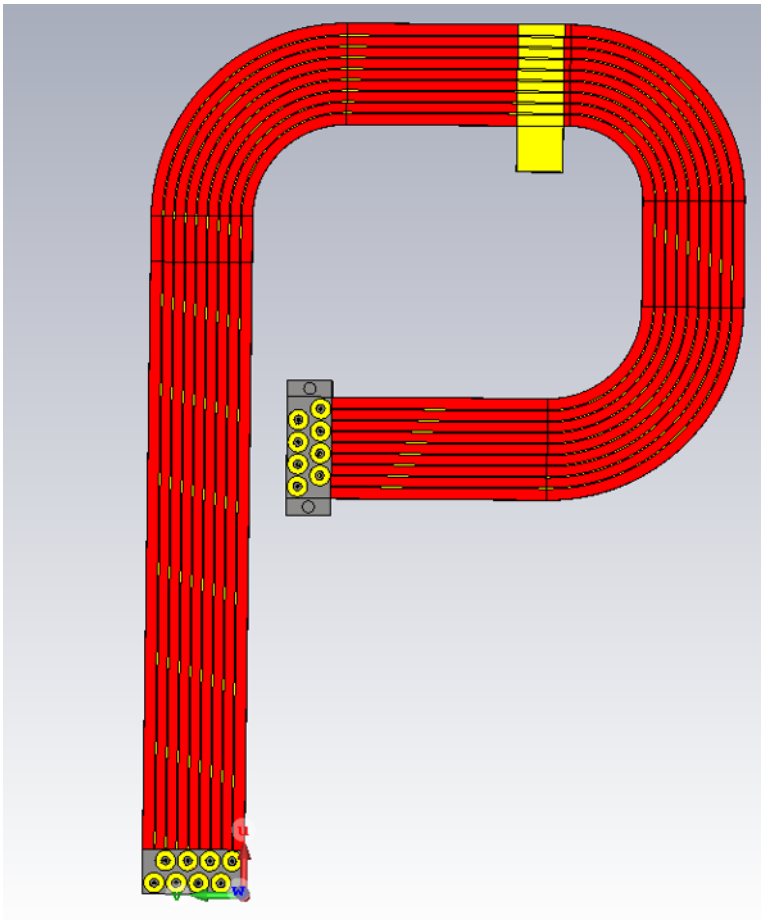

Figure 33. CAD Drawing of a Cold Band

Note: Drawing of an individual custom flex circuit cable. There are two per band, and three bands total within the IF harness. Each circuit has a unique shape in order to facilitate the complex routing within the GUSTO cryostat. Visible in this drawing is a small heat-sinking tab that can be directly soldered to. Each band has two tabs that can be attached to separate stages of the cryostat for temperature control. Also visible are fastener holes used to secure the circuit on one end. Copper is shown in yellow, the kapton substrate is in red, and the top layer of solder mask is shown in grey. The yellow copper stripes that follow the path of the substrate are copper ground planes necessary for stripline transmission. These are not the signal traces themselves. The signal traces are buried under the substrate layer.

For each band the ribbons required two points of contact with the cryostat. This was made possible by small 0.50" x 0.50" copper heat-sinking tabs that could be directly soldered to. The operating temperature for the GUSTO mission will be a 20 K - 300 K gradient. Using both heat-sinking tabs will help maintain that gradient. Like the prototype, each ribbon was an eight-channel transmission line with the connections staggered so they could connect to one another. DELTA Electronics smooth-bore SMP press-on connectors were chosen because of their small form factor and low retaining forces. It was discovered in prototyping that higher mate/de-mate force might reduce the lifetime of a ribbon after repeated use. The eight smooth-bore connections were sufficient to hold the flex circuits together, however a clamp would be used for added security. I designed a two-piece clamp out of Garolite grade-10 (G10) fiber glass material. A CAD model of the G10 clamp can be seen in Figure 34. Objects at cryogenic temperatures would tend to shrink and Garolite was no exception. G10 has a coefficient of linear thermal expansion (CTE): $\alpha = 9.9 \times 10^{-6}$ C^{-1}. The dimensions of the clamp had to be chosen such that when the circuit was at low temperature the clamp would not change so much that they damage the circuit. I used equation 3.7 to design the width and length of the clamp so that, at room temperatures the clamp would be slightly loose (i.e. not allowing full engagement of connectors) and only tighten as the component lengths contracted.

$$\frac{\Delta l}{l_0} = \alpha \Delta T \tag{3.7}$$

In the above equation Δl is the change in length an object will undergo due to temperature change. The initial object length is l_0, the change in temperature is ΔT, and α is the CTE. The largest change in length is $\sim$ 7 mils. Not particularly

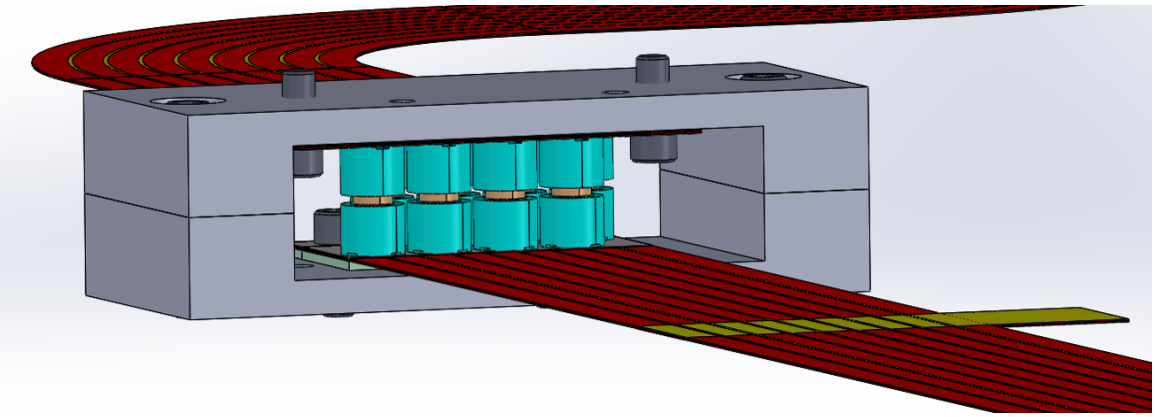

Figure 34. Design of Flex Retaining Clamp

Note: This CAD Figure shows how a two-part G10 fiberglass clamp was designed hold the cold and warm end together for each IF band. The clamps would individually attach to the different flex bands. Then the clamps would be fastened to one another. Also visible here are the smooth bore SMP connectors in teal, and the bullet adapters in tan.

concerning for the safety of the connectors. Figure 34 shows the initial design of the G10 clamp engaged at connection position. Figure 35 is the full cold and warm assembly of a single IF band with the clamp installed, and the approximate location of the vacuum flange on the warm end. This image is before the bending inside the cryostat so it is indicative of how the flex circuit would naturally rest on a test bench when assembled.

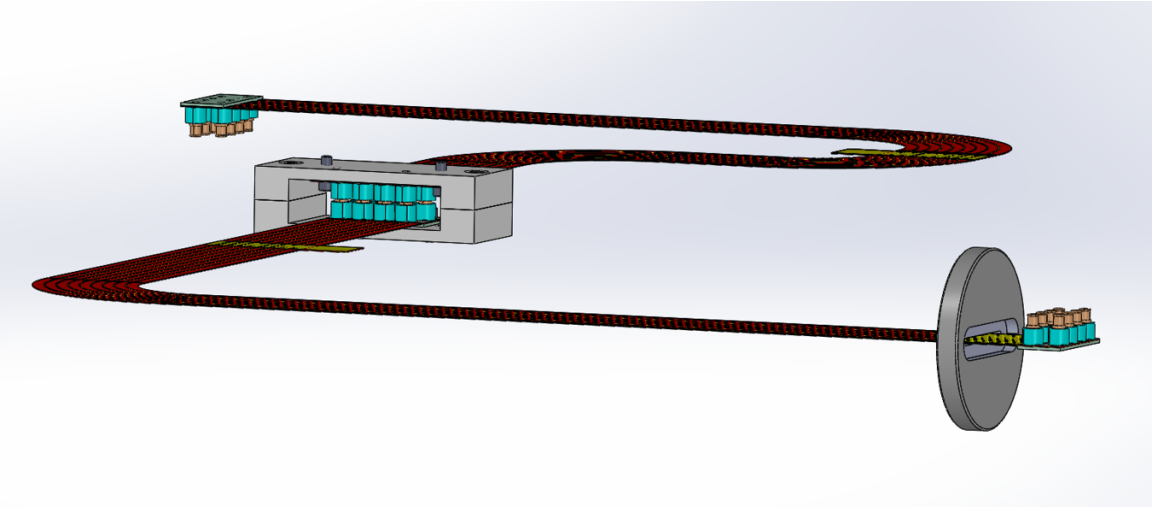

Figure 35. GUSTO Full Band Flex Ribbon

Note: A full band of GUSTO's IF system. The cold and warm flex circuits are attatched with SMP connectors and secured with a clamp. The warm end has a CF flange near the warm IF connections.

3.3.2 Space Qualifying & Fabrication

In order to meet all of NASA's requirements I had to develop and follow a rigorous test plan. This was not just a method for characterizing the RF performance, but a series of steps to be put in place that ensure the hardware was handled carefully and with purpose. Every part of the flex circuit development had to be meticulously documented so that there was a clear line of accountability. This was true for the design phase as well as fabrication.

The fabrication was again done by Coast to Coast Circuits. There were six GUSTO flight flex circuits, two for each of the three intermediate frequency (IF) bands. Duplicates were made as spare hardware. Coast to Coast also provided a test sample of the flex circuit for NASA Goddard to assess the quality of the board lamination and approve for further assembly. The assembly work to solder the SMP connectors to the flex boards was done by GMA Manufacturing LLC. They were chosen because they could solder surface mount connectors using the required IPC class 3 techniques. These were the highest classification of safety and verification reserved for devices used in medical and space industry application. With their automated pick-and-place machine they could easily populate the 16 connectors per each 8-channel ribbon. They used a re-flow oven to precisely control temperatures used in the soldering process to minimize the risk of excess heat flowing into the circuit and de-laminating the layers or damaging the connector. GMA also provided X-ray images of the solder joints for inspection. After that I could began encapsulating the circuits for vacuum use.

3.3.3 Encapsulation & Installation

Bonding and encapsulation of the GUSTO flex circuits was different than in my prototype work. To begin with, I had to use aerospace grade epoxy rather than the standard kind, and I had to provide a test sample of the mix prior to applying any bonding material to the flight hardware. The test brick had to be indicative of the quality of the epoxy that was going to the flex circuit. It was decided rather than mixing the epoxy myself by hand, that I would instead buy it pre-mixed in bulk. Two-part epoxy begins to cure (or harden) immediately after the separate components mix. This leaves only a short $\sim$ 1 hour window to apply the glue. The bond can be slowed using low temperatures, and conversely bonding can be sped up by applying heat. I ordered pre-mixed 3M EC-2216 aerospace certified epoxy from Appli-Tec Adhesive Solutions. The epoxy was mixed and stored in individual manually depressable syringes, and shipped in a container full of dry ice. The epoxy was stored in an industrial freezer at -79 degrees Celsius. The test puck was from the same batch as all 25 epoxy syringes which simplified the inspection requirements rather than having to make a test sample every time I mixed enough epoxy for one or two circuits. I practiced with spare flanges and similar flexible materials so I would have a procedure worked out before the real thing.

The warm flex circuits were potted with the 3M EC-2216 epoxy to vacuum stainless steel ConFlat (CF) flanges. The CF flanges were compatible with the GUSTO cryostat but required an adapter to connect to our system. The "cold" circuits would not exit the cryostat and therefore were not to be potted. The flex circuit could not fit through the flange slit when the connectors were soldered on so they had to be inserted before GMA did the assembly, and carefully worked around

when they were attaching connectors. The warm flex had a solid ground plane where the flange would bond to. This would prevent external signal from permeating the portion of the flex lines exiting the cryostat. Prior to the bond process, Kapton tape was applied to the under-side of the flange to make a barrier and control the flow of epoxy. The epoxy would not adhere to the tape. Panavise clamps were used to hold the flange and the loose end of the flex circuit for stability. Only after everything was setup for bonding would a manual syringe would be retrieved from the freezer. It took $\sim$ 15 minutes for the epoxy to thaw enough to flow easily from the syringe. The trench of the flange was completely filled with epoxy and the setup was left in the clean room to cure for 24 hours, which was more than enough time for the epoxy to reach handling strength. This process took several days. There were the three warm circuits and a series of spares that had to be bonded and vacuum tested. In order to do a full band end-to-end cryogenic RF test of each channel, one additional 5.0 inch test flex circuit was made. This was necessary because the cold end was not able to exit the vacuum system, and there were not enough coax ports on the cryostat to connect to every channel in a single test. To get around this, the cold circuit would instead connect to another short warm circuit that did exit via flange. This allowed access to all 8 channels of the flex circuit in one cryogenic cycle. Figure 36 shows an encapsulated flight warm circuit.

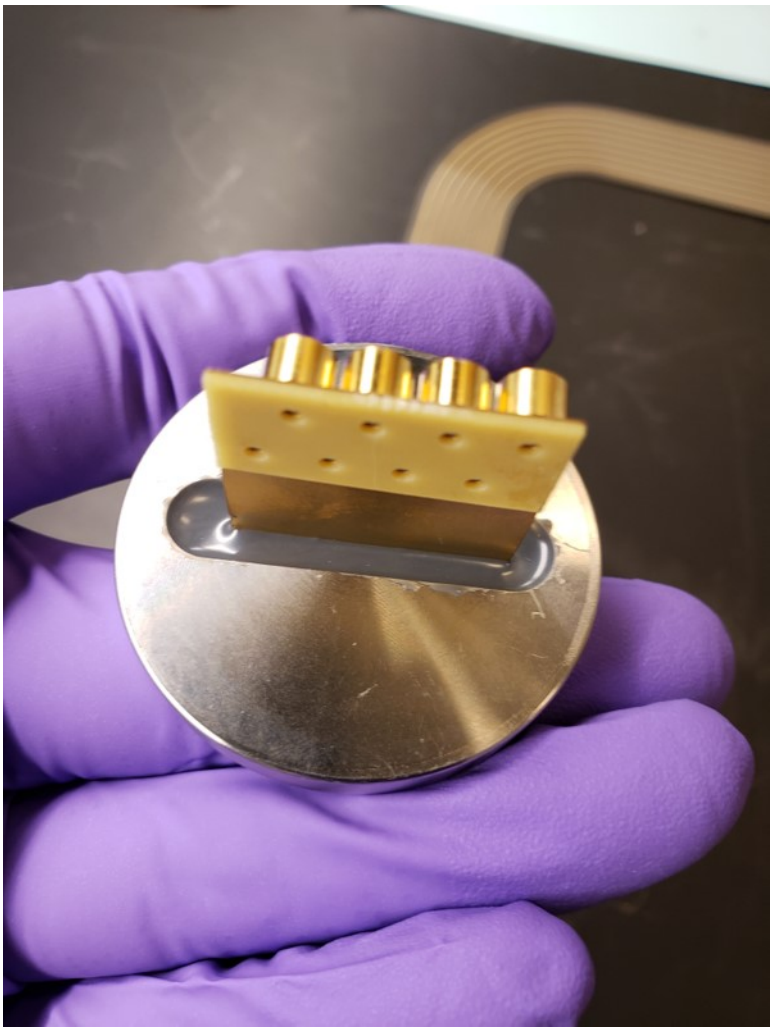

Figure 36. GUSTO Warm Band 1 Epoxy

Note: An example of the encapsulation with epoxy. GUSTO warm circuits were bonded to stainless steel ConFlat flanges. The bonding material was aerospace grade 3M EC-2216 epoxy deposited by manual cyringe.

For installation of an entire IF band, the warm end was fed into the cryostat through a removable blank which left a large hole when detached from the cryostat. The CF flange potted to the flex circuit would mate to another CF flange that was welded to metal tube on one end, and the compatible test cryostat blank was welded to the other side of that tube. This can be seen in Figure 37. The flange was fully secured on the warm end to the cryostat with four fasteners. The cold band was placed entirely inside the cryostat. The size of the test cryostat was not large enough for a full band to come to rest naturally. Although every step was taken to minimize stress on the flex circuit and that each band retained its natural shape, some slight bends were necessary. All prototype circuits showed no defects bending as severe as a 0.5" bend radius. The RF connection between the bands were made by first attaching each circuit to its corresponding clamp (see Figure 38. The clamps were then fastened together. This ensured no extra pressure was added to the connection sites from the clamp or other sources and that the flex circuits could not come apart on their own. Prototype clamps were tested at 10 K temperatures, below what was needed for this test. For thermal connection each of the tabs of the flex circuit were clamped to a copper braid by an aluminum fixture. The cold tab was heat sunk to the 10 K stage, and the warm tab was not heat sunk. This would create a gradient temperature through the circuit. The last step was to install the cryostat "test," or, adapter circuit in the same way the warm end was installed. These adapters were shorter and easier to work with. There were 3 blanks on either side of the cryostat that could be removed to install the adapter. The blank chosen was the one nearest the cold flex which the adapter would connect to. The adapter was clamped in the same way for RF connection as the warm and cold bands. Uninstalling would be the same process in reverse.

Figure 37. GUSTO Band 2D Testing

Note: This figure shows a full band of the GUSTO harness installed for RF testing. Visible to the right is a single channel blank which is a hermetic feed through coax. The GUSTO cryostat was designed for CF type flanges. An adapter had to be machined to fit the CF flange to the KF style of the test bed. Otherwise the flex would be bonded directly to the KF flange instead.

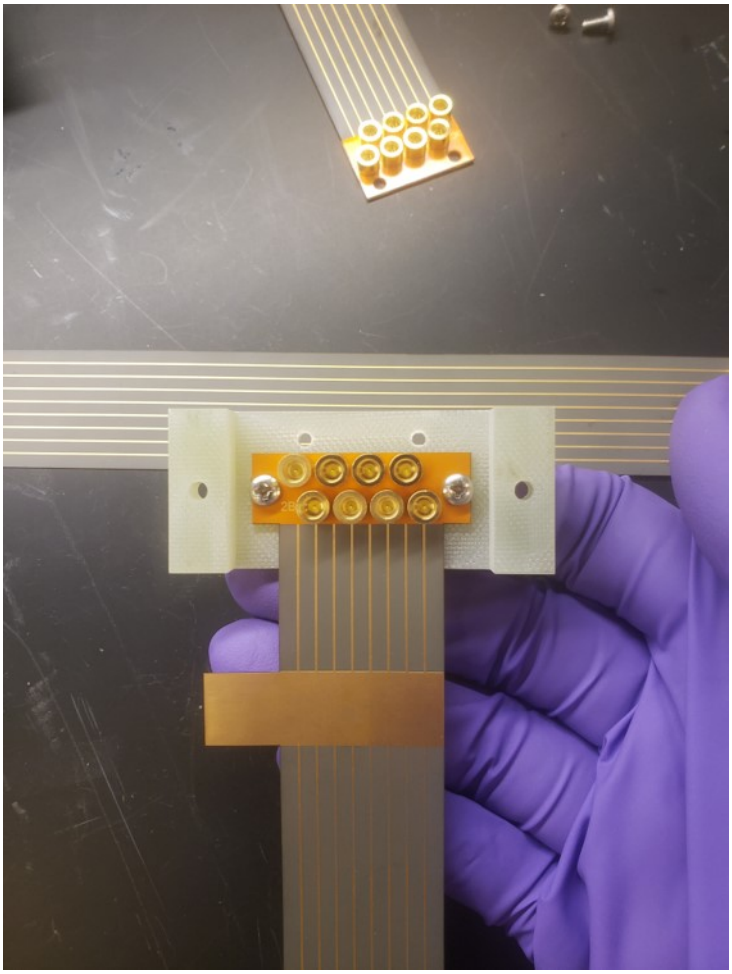

Figure 38. IF Clamp

Note: The cold end of a GUSTO band as it is being fastened to its G10 clamp. This was the first step in attatching the IF bands together.

3.3.4 Heat Cycles & Vacuum Testing

The flex ribbons designed for the GUSTO mission had a solid copper plane where the vacuum flange was to be potted. The vacuum flange was to be a modified stainless-steel CF flange commonly used in high vacuum instruments. All previous flex circuit testing had been designed for aluminum KF flanges. The prototype aluminum flanges were helium leak checked to test their vacuum. A helium mass spectrometer with a roughing pump was attached the cryostat. After reaching vacuum pressure the mass spec would go into test mode. A compressed gas canister of helium with a long hose was used to spray a slow rate of gas around the sealing surfaces of the cryogenic system. An alarm would sound if helium breached the vacuum chamber. No leaks were detected for the prototypes. The flanges were then thermally cycled in a liquid nitrogen bath, and leaked tested again with no leaks detected. It was believed that the same process would suffice for the stainless steel CF type flanges used in GUSTO. This turned out not be the case.

The first set of flight hardware warm circuits were vacuum tested together after epoxy had made it to full cure. All three warm circuits were installed together on copper heat brackets with their entire CF collar. A temperature sensor was placed at the band 2 flange. No leaks were present at the time of the initial leak check. The circuits were than thermally cycled for a temperature range of -40 C to +60 C for a total of six cycles. The bonded circuits were then leak tested again to make sure the adhesive held together. This time unfortunately two out of the three circuits registered an air leak above tolerance. The leak appeared to occur at the interface between flange and adhesive. To be certain of this, the leaking circuits were cut out

of their flange. The epoxy had still adhered to the flex circuit after flange removal, but it broke away easily from the CF flange.

A second set of modified CF flanges were made and this time the surfaces were prepared differently before bonding. The flanges were bead-blasted to give them an abrasive surface that the scotch weld epoxy might better adhere to. Industrial grade chemical solvents were used to clean the CF flange of any machine oils or other contaminants that would prevent complete adhesion. The CF flanges were also cleaned using mineral spirits and isopropyl alcohol in a sonic bath. Test circuits were bonded to the cleaned flanges. Initial leak testing found no leaks. The flanges were thermal cycled and tested again. Just as before, two out of three flanges were observed to leak. The leak was again detected on the interface between flange and adhesive. The flex circuit itself was not believed to be the source of the leak. The test setup can be seen in Figure 39. The CF flanges were cut using precision machines and the flex circuits were saved for future use. They did not suffer RF or mechanical failure from any part of that process. Due to costs of aluminum CF flanges to replace the stainless-steel ones for GUSTO, and the time constraints of the mission, an alternate break-out scheme was designed. A CF flange with 4 hermetic feed through adapters would be used as the outside interface. The flex ribbons would reach this flange and attach via a series of short coax lines which would serve as the interconnects between flange and ribbon.

Figure 39. Thermal Cycles of GUSTO Flex Ribbon

Note: This figure shows the test setup for the flange thermal cycles. A compressor and heaters were used to cycle the temperature between -40 C to +60 C. This was beyond the extremes the instrument would see in flight. A helium leak detector was used before and after the cycles. Vacuum leaks that were not present before thermal cycling had formed after.

3.3.5 RF Testing

The same closed cycle vacuum cryogenic 10 K test bed was used to characterize the IF harness as the one used in prototype testing. All RF measurements were done using a Rhode & Schwarz ZVA 24 Vector Network Analyzer (VNA) that was certified calibrated by the manufacturer, and following a pre-approved test plan. The VNA test port power was set to 0 dBm, with 10x averaging and an IF frequency of 100 Hz. The measurement bandwidth was 0.1 - 6 GHz which encompasses the 0.3 - 4 GHz operating frequencies the IF harness would see during its mission. Due to the limiting size of the test bed only one band could be tested at a time.

The cryostat interface was a custom made bulkhead plate with four hermetic SMA feed-through adapters. Short mini circuits SMA-SMP UT-47 coax cables were used to transition from the bulkhead to the flex ribbon. Earlier tests were done using small flex ribbon segments specifically made to serve as adapters for the flex circuit interface. The change to coax was done because of the vacuum leak. These would now be the new in flight conditions. The coaxial adapters were not heat-sunk and therefor closer to the ambient temperature outside the cryostat. In order to de-embed their effects from the flex ribbon room temperature measurement of the Mini-Circuits cables were recorded. The room temperature data was then subtracted from the cryogenic result at all frequency points. Four total bulkhead adapters were used in each measurement so all eight channels of the IF harness could be reached in a single cool-down. Measuring all eight channels at once saves time by reducing the number of cryogenic cycles per band. This also meant that the environmental conditions inside the test bed remained unchanged for each ribbon.

The two flex ribbons of each band were fastened together using a clamp and

then installed on the 10 K stage of the cryogenic test bed. One heat-sinking tab was thermally coupled to the 10 K stage. There was insufficient space to couple the second tab of any band and still be able to connect the flex ribbon to the cryostat output. This resulted in a much higher temperature gradient through the flex ribbon than the likely temperature profile it will have in flight. Thus all results presented are worse than expected for the actual mission. When the ribbon was fully installed a temperature sensor was placed in contact with the circuit at the heat-sinking tab. Two resistor heaters were attached to the 10 K stage.

The test bed could reach $\sim$ 10 K temperatures in just under three hours. The system was run until a stable 10 K temperature was achieved, and the heaters were slowly dialed up so the cold plate temperature would stay above 20 K as was expected during the GUSTO mission. RF measurements were taken to test the signal transmission, reflections, and isolation or cross-talk. After a band was measured, the heaters, and cryogenic station were turned off. The system was brought back to ambient room temperatures overnight without the use of heaters. Figure 40 is a plot of the average s-parameters of all three bands with an average band length of 3.3 feet.

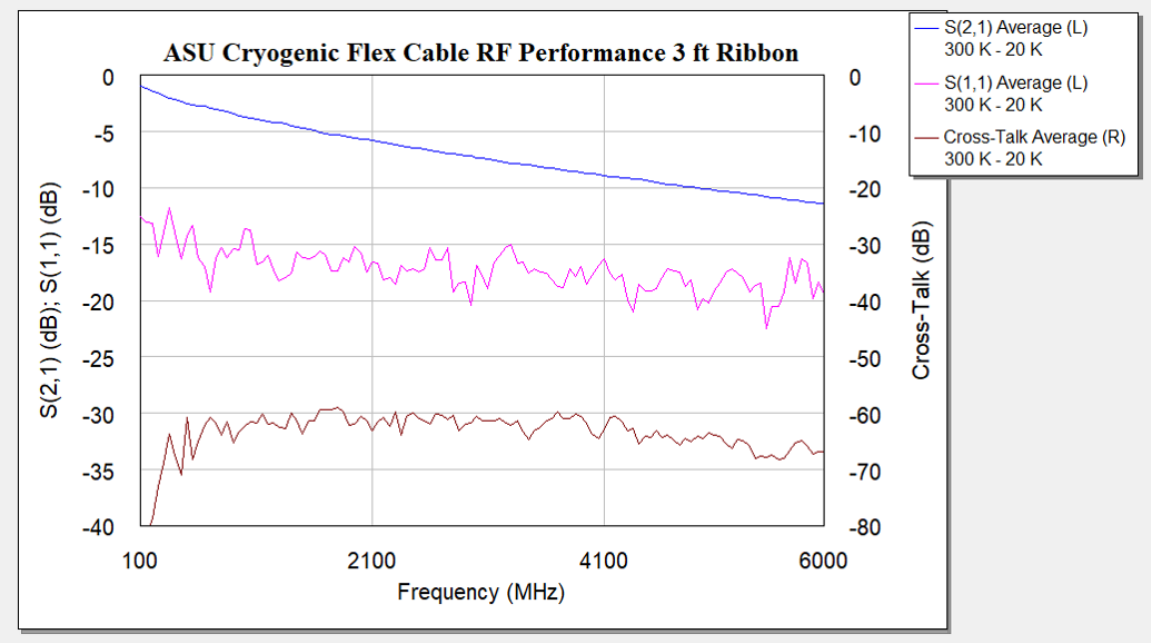

Figure 40. GUSTO RF Performance

Note: Average s-parameters of all three IF bands are shown. The cryogenic testing was done with one end of the band held near 300 K and the other end held at 20 K. The average length of each band is 3.3 ft. At 5 GHz frequency the average loss per band is 3.07 dB/ft which exceeds design specifications. The cross-talk between adjacent channels is below -60 dB for nearly the whole bandwidth which also exceeds the specifications. There are no requirements for the reflection, however a value below -15 dB is usually desirable in RF applications.

The design specifications for the GUSTO IF harness were: IF bandwidth of 0.3 - 4 GHz, a signal loss no greater than 6.00 dB per 20" length of harness at 5 GHz frequency, and 30 dB or more of isolation between channels. As shown in table 4, the average loss of all three bands is 10.14 dB for the full 3.30 ft length which means IL is 5.12 dB per 20" length. The measured cross-talk shows greater than 60 dB of isolation between channels for nearly the entire IF bandwidth. The circuits were measured from 0.1 - 6 GHz. Having met all mission specs the IF harness was delivered and integrated with remaining flight hardware on schedule.

Table 4. RF Performance for Various TL Schemes

	Flex Ribbon*	UT-085	UT-047	UT-034	UT-020
Avg Length (ft)	3.30	3.30	3.30	3.30	3.30
Loss @ 5 GHz (dB)	10.14	9.35	16.61	23.59	40.71
Loss @ 5 GHz (dB/ft)	3.07	2.83	5.03	7.15	12.34

Note: The RF insertion loss for various transmission line options ranging from ASU's custom flex circuits to commercial semi-rigid stainless steel coax. The values are for a TL length of 3.3 ft which is comparable to the GUSTO IF band. Various radii of coax shown for comparison. Coax lines performance taken at room temp.
*The flex ribbon value is for a ribbon at a 20K - 300K temperature gradient.

3.3.6 Lessons Learned

Many new insights were gained through the process of testing the GUSTO IF Harness. The first new issue to come up was the leak post thermal cycling. Some investigation was put into finding the root cause. It is unclear whether or not the leak was a result of the thermal cycling method (i.e. time dependence of thermal cycles) or if the chosen adhesive did not retain its bond with stainless-steel surfaces due to a mismatch in expansion coefficients. Aluminum flanges have not had any

leaks. Having to exit the cryostat using bulkhead adapters is less elegant than the original design. Still, the overall amount of adapters needed were cut down by the flex achieving the route path. The cold end could still mate to the LNA enclosure box. It is also worth noting that the leak did not occur at the flex-epoxy interface. The solution for future missions is either to use only aluminium flanges, or to repeat the thermal cycling for a bonding material that more closely matches to stainless steel's CTE.

Another unexpected event occurred when separating the cold end of the flex from the test circuit. Individual smooth bore connectors required only a small de-mate force. Eight connectors engaged together made removal a problem. The first two test circuits had solder joints that snapped from the net forces of the removal process. No damage was done to any flight hardware, but I wanted to make sure operators could assemble and disassemble the bands without a repeat of this issue. I designed a set of U shaped brackets that would slot in around the connectors. Four sets of bolts could be turned in staggered increments to act as a jack for the flex circuits. This guaranteed an even force applied across the connectors. Two sets of brackets were made. One for the separation of the warm and cold flex, and one for the detaching of the flex from the LNA enclosure box. Future missions were designed using a single strip-connector with four SMPs in a row. The strips have guide pin and fastener holes that can be used to ensure an even de-mate.

The GUSTO mission will showcase several of the best features and abilities of the ASU cryogenic flex ribbons. Upcoming instruments that have a high pixel count, complicated or limited routing space, and have need of compact and lightweight solutions for their IF system will benefit from using the ASU flex cables. The lessons learned from the GUSTO mission will drive further innovation of the flex

ribbon that already offers comparable performance to industry standard semi-rigid coax with other measurable benefits. The ASU flex ribbon exceeds all RF design specifications that were set for the GUSTO mission. They achieved a bandwidth that includes 0.3 - 4 GHz with an insertion loss at cryogenic temperatures that is 3.07 dB/ft and Isolation much greater than 30 dB over the entire bandwidth.

3.4 Future Missions

Looking ahead to future missions that would make use of flex circuits, the next steps for the technology were to improve the assembly techniques and try to further reduce production cost. Some steps have already been taken toward that end. Connector assembly for most circuit boards can be done easily and efficiently with pick and place machines that use a vacuum to pick up and position circuit components like connectors directly to lands and pads. Printed circuit boards are usually run through this automated process while they are still attached to the sheet material they're made from so that many smaller boards can be worked on at the same time. The problem with using pick and place machines for flex circuit design was that the warm end of the flex circuit had to be detached from the progenitor board so that the warm end could be fed through the vacuum flange before connectors were soldered. There was now way to get the circuit through the flange opening with connectors that would not compromise the vacuum seal. The flange was also very heavy and had to be carefully secured on the flex board. The circuit could be taped back into place but it was a manually intensive process for an otherwise fire and forget system. The uncertainty in the flange location while being assembled also caused the manufacturer to increase spacing between the flex ribbons

to make sure the flange would not interfere with a neighboring circuit. The price of the flex circuits changed with how many one could fit on a production panel so any added separation between ribbons could drive cost up significantly. For newer flex circuits I added guide pin holes to the design that could be used by the assembler to more precisely hold and reposition the flex circuit back in place after the flange was secured. The guide pins mate to a backing plate which holds the panel and flanges.

As I mention in section 3.3.6 the next generation of flex will have an SMP connector strip which can be seen in Figure 41. The connector strip were made custom. They had been used in two variant designs one with four, and one with three connectors per strip. I conducted RF tests of circuits with the strip connectors vs individual and found them to have comparable performance.

In addition to the RF performance, the integrity of the vacuum seal for the flex circuits was an important issue. To improve the epoxy bonding process I designed a retaining bracket that can hold both the flex circuit and flange in place. This bracket could be custom designed and cheaply made, but it provides invaluable support. It adds precision to where the bonding will happen at a specific length from the end of the circuit. This means uniformity for the encapsulation process which was not guaranteed by previous methods. I vacuum tested a set of 20 circuits encapsulated this way and they were able to achieve stellar vacuum performance as well as a uniform bond. More details about new missions supported by flex circuits will be in section 5. Gaining heritage on flight and ground based missions is extremely important to boost confidence in the methodology. Thus far the flex lines have proven adaptable to a variety of operating constraints and design challenges. With each revision they get closer to phasing out coax for large scale missions.

Figure 41. SMP Connector Strip

Note: An eight channel ribbon designed with a row of four SMP connected together. This custom made strip improves the strength of the connection sights and solder joints. These rows also help in the flex band assembly and disassembly process.

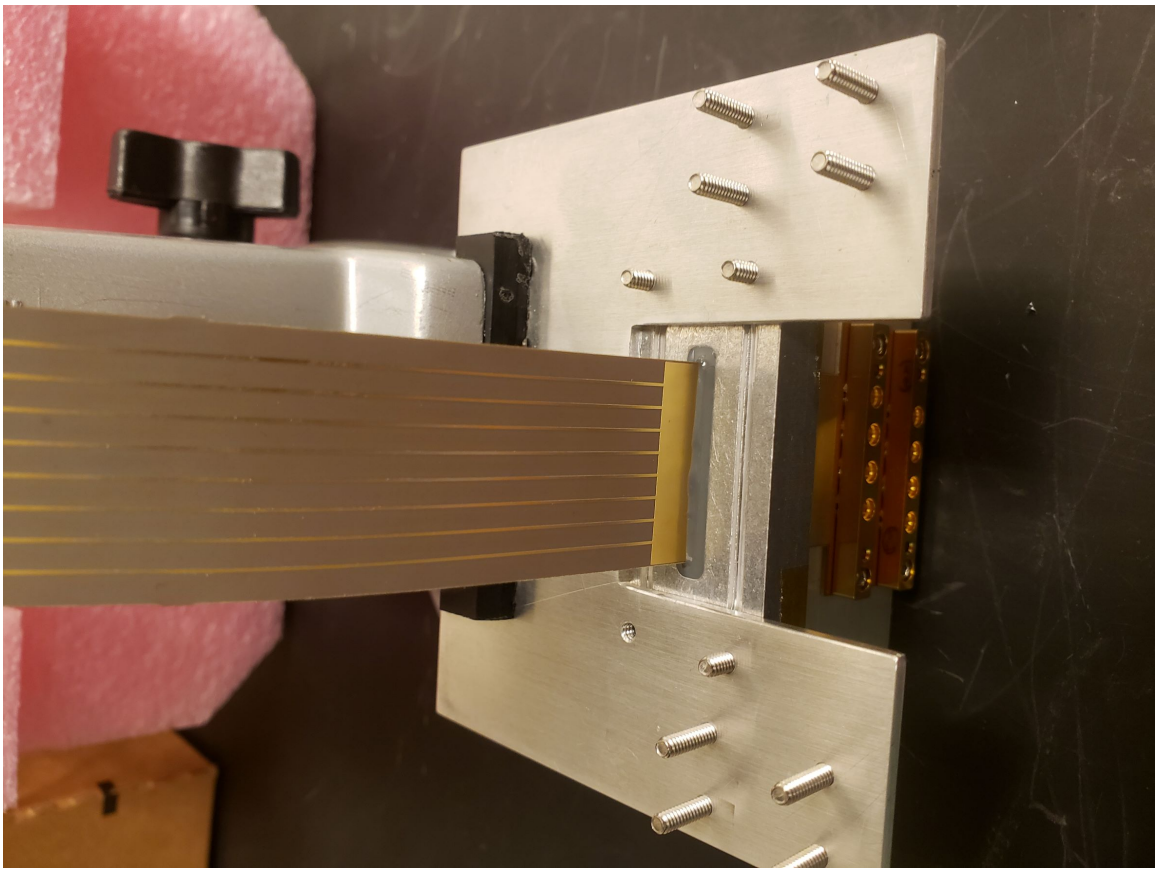

Figure 42. New Encapsulation Method

Note: Pictured here is an assembly bracket that holds the flex ribbon and flange in place at the desired bond point.

Chapter 4

CHARACTERIZATION OF SUPER CONDUCTING NON-LINEAR DEVICES

4.1 GUSTO Hot Electron Bolometer

The non-linear mixing element of the GUSTO IF was a niobium nitride hot electron bolometer fabricated at the Space Research Organization of the Netherlands (SRON). Figure 43 is an example of this type of mixer. The components were a copper block housing with a 5 mm lens bonded to its center. The lens was a hyper-hemispherical lens with the flat end of the sphere facing the reader. On the top of the lens was a spiral antenna coupled to a transmission line via wire bonds. The transmission line was a co-planar waveguide (CPW) that bridged the antenna signal to a single SMA output. Thin film strips of NbN were deposited on the antenna. When light passes through the lens it imparts energy into the thin film which will illicit an interaction between the superconductor and the substrate. Transmission can be read out through the SMA via a bias network that also provides DC power to the device.

This type of HEB mixer served as a receiver for GUSTO, but similar ones were used in STO-2 and even Herschel. Impedance matching the receiver to the rest of the IF system is necessary to remove reflections. Both STO-2 and Herschel suffered from standing waves that resulted from impedance mismatch. This meant that data analysis of IF signals was often difficult to reduce. The HEB complex impedance depended on temperature, frequency, and LO power level. The device was superconducting so it had to be operated at cryogenic temperatures. Device

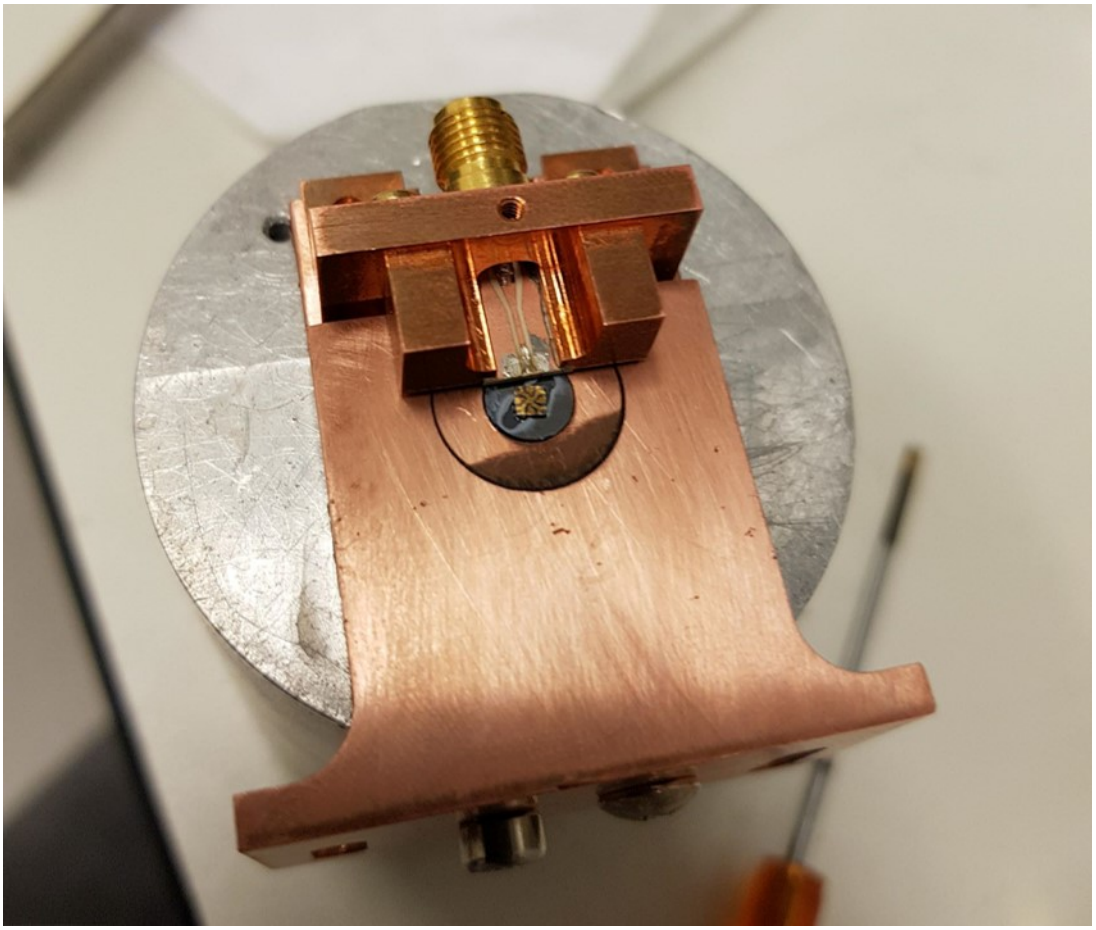

Figure 43. Hot Electron Bolometer Mixer

Note: An HEB mixer fabricated at SRON.

characterization inside cryostats is notoriously difficult since almost no calibration setup is guaranteed to work. In this chapter I detail my setup and attempt to measure the impedance of the GUSTO mixer. The theory behind the HEB impedance is discussed in section 4.1.1, the basics of VNA calibration are introduced in section 4.2. The initial attempt to measure the HEB failed due to the condition of the device at the time, but that is explained in section 4.3, and the final measurement with a working superconducting device is section 4.4

4.1.1 Theoretical Impedance

Two initial models proposed theoretical frameworks for the operating principles of an HEB mixer modeled as a lumped element transition edge sensor (TES). Ekström et al. (1995) presented what is known as the standard model for HEBs where electron heating is suggested as the source of the mixer's non-linear attributes. From that work, the complex impedance as a function of frequency in simplified form can be written as:

$$Z(\omega) = R_0 \left(\frac{1+C}{1-C}\right) \left(\frac{1+i\omega\frac{\tau_\theta}{1+C}}{1-i\omega\frac{\tau_\theta}{1-C}}\right) \tag{4.1}$$

R_0 is the DC resistance for when the superconductor is above T_C. C is known as the self-heating parameter. τ_θ is the electron temperature relaxation time.

Nebosis, Semenov, and Renk (1996), generalized their theory to include feedback between the mixer and IF system. This is commonly referred to as the NSGR model. Since HEB mixers were made by placing a structured superconducting film on a dielectric substrate the authors developed their models with an electron-phonon system in the film, and a phonon system in the substrate thermally coupled to each other. Phonons are a traveling vibration of ions that are like a thermal propagation through a physical structure analogous to photons, but unlike photons they are not quantized. When the lens of the mixer was illuminated by incident radiation, the electrical power was absorbed by electrons in the thin film. The power was then transferred first through the film via electron-phonon interactions and then to the substrate via phonon escape. The system is described by a pair of coupled heat balance equations In this model they write the electron temperature relaxation time in terms of electron-phonon interaction, and phonon escape:

$$\tau_\theta = \tau_{\text{eph}} + \frac{c_e}{c_{\text{ph}}}\tau_{\text{esc}} \tag{4.2}$$

τ_{eph} is the electron-phonon interaction time. τ_{esc} is the phonon escape time that is a measure of how long it takes for the superconducting film to transfer heat via phonons into the substrate. The variables c_e, and c_p are specific heats of electrons and phonons in the film. The impedance in this model is calculated by:

$$Z(\omega) = R_0 \frac{\psi(\omega) + C}{\psi(\omega) - C} \tag{4.3}$$

Like before, R_0 is the dc resistance at the operating point of the mixer, and C is the self heating parameter. Here $\psi(\omega)$ represents the time dependent modulation of the electron temperature.

$$\psi(\omega) = \frac{(1 + i\omega\tau_1)(1 + i\omega\tau_2)}{(1 + i\omega\tau_3)} \tag{4.4}$$

Where the three additional time constants of $\tau_{1,2,3}$ are given by:

$$\tau_1^{-1}, \tau_2^{-1} = \frac{\Omega}{2}\left(1 \mp \sqrt{1 - \frac{4\tau_{\text{eph}}^{-1}\tau_{\text{esc}}^{-1}}{\Omega^2}}\right) \tag{4.5}$$

$$\Omega = \left(1 + \frac{c_e}{c_{\text{ph}}}\right)\tau_{\text{eph}}^{-1} + \tau_{\text{esc}}^{-1} \tag{4.6}$$

$$\tau_3^{-1} = \frac{c_e}{c_{\text{ph}}}\tau_{\text{eph}}^{-1} + \tau_{\text{esc}}^{-1} \tag{4.7}$$

Accurate device measurements are needed to compare to theory. The first challenge was to setup a calibration technique that would work for not only the GUSTO HEB but any superconducting element.

4.2 VNA Calibration

Characterization of any RF device can be done by S-parameter measurements using a vector network analyzer. The accuracy of that measurement is entirely dependent on calibration. The VNA has a factory calibration that sets the point of measurement, or the reference plane, directly at the output ports of the device. In other words any raw measurement taken by the instrument will include every component after the VNA port. If a coax cable leads from the VNA port to the device under test (DUT), then the measurement observes the signal through the full length of that cable to the device and back again. To de-embed the loss effects of that cable requires calibration. This usually means using a set of known calibration standards as references. These are RF components that have predictable behavior over a given frequency range that are already well measured with the VNA. The calibration standards are inserted in the system where the DUT would physically be. A calibration file on the VNA knows what the S-parameters are supposed to look like. The VNA calculates an error matrix then subtracts the effects of cable length (or any other active/passive component) between the output port and the standards. This effectively moves the reference plane from its output ports to the location of the cal standards. A basic representation can be seen in Figure 44.

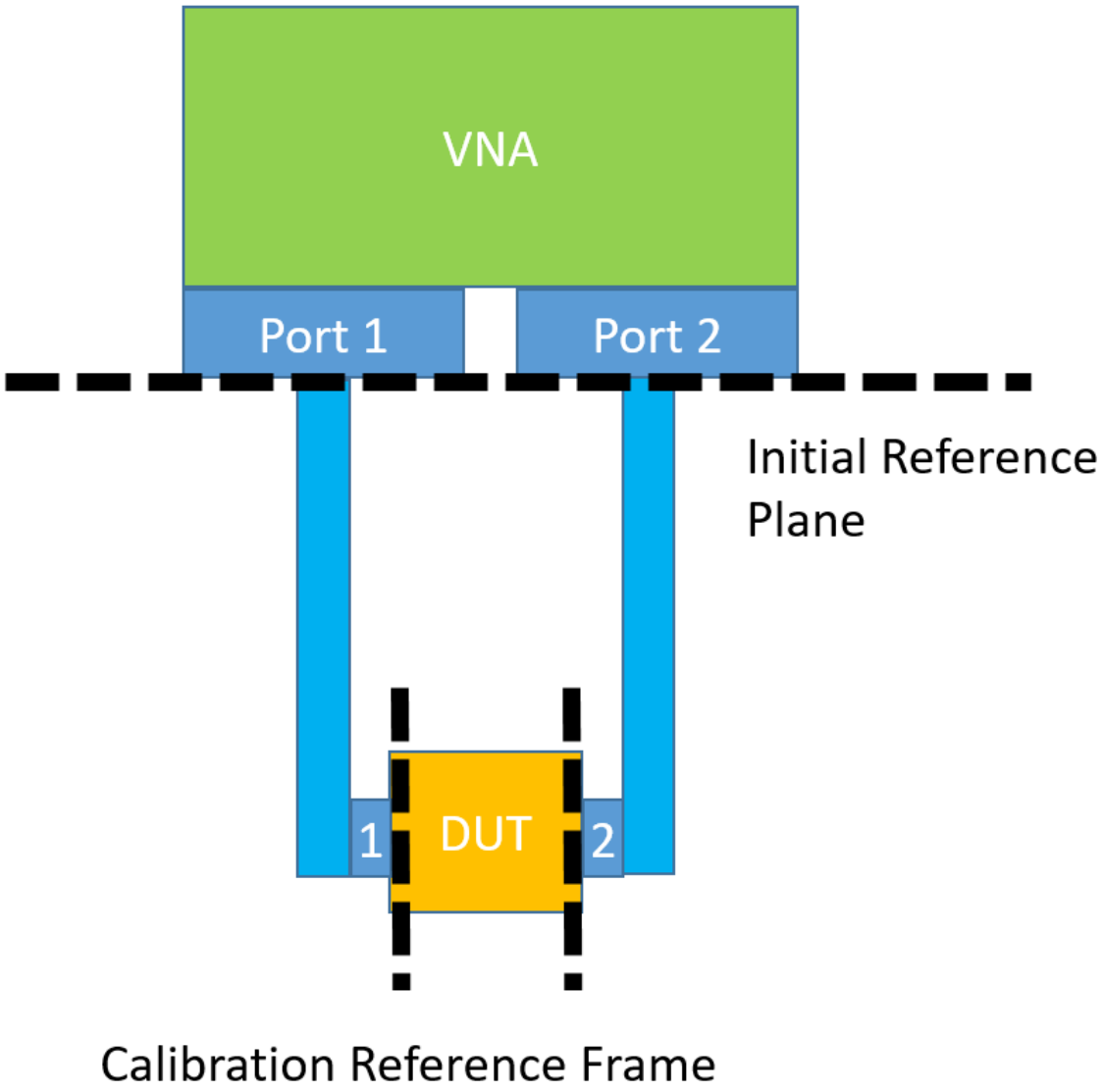

Figure 44. VNA Calibration Reference Plane

Note: The initial factory calibration of a vector network analyzer (VNA) is set to the output ports of the instrument. Calibration standards can be used to move the reference plane through cables and other RF interconnects so that the measurement is taken at the ports of a DUT.

There are many different types of calibration standards. Most of which will not be discussed here. The two types of calibrating that are relevant to this work are the Through-Reflect-Line (TRL) method, and the Open-Short-Load (OSL, sometimes SOL). These names are highly indicative of the objects used in calibration. An RF through is a small length of transmission line, like a coplanar waveguide, or very short coaxial piece. The purpose of the through is to provide a direct low loss path. In TRL calibration the first component is a through that allows signal to pass between two VNA ports. The reflect component is usually similar to the through except that there is a break in the line that prevents transition forward and causes reflection back to the input. The "line" component is a length of transmission line similar to the through, but in the case of the line standard there is intentional loss brought on by the length and shape of the line that is quantifiable and well documented. This method is an ideal calibration technique for moving the reference plane of two-ports simultaneously, i.e. a two-port calibration. It also has the benefit of doing so with only three standards, which reduces the time it takes to calibrate. For these reasons in-situ (or in position) TRL is best used for non-packaged chip measurements which are circuit elements outside of an enclosure or housing. This is useful when trying to identify the properties of a single component before adding it to a larger circuit like an amplifier.

The one-port alternative is to use an open circuit (or something that behaves like an open circuit for a set frequency range), a short circuit, and a known matched purely resistive load. The matched load is typically a 50 Ω resistor. The process can be repeated for each port of the VNA separately so that a two-port calibration is possible with this method, but it required a through line for best accuracy at two-port cal. Typical OSL calibration kits have SMA connectors that are not only

compatible with the VNA, but are often similar to other device packaging. While TRL gives a good staging point for measuring individual components without the need for connectors, an OSL calibration is used to characterise a fully packaged device so that characterization includes the effects from its housing. This better simulates the impedance miss-match the entire device would provide to something like an IF harness.

Device calibration this way is extremely temperature dependent. The impedance of any RF component will change with the shape of the component. Expansion and contraction of the device effects RF performance. The conductivity of the device is also effected by temperatures. This holds especially true for superconducting device which change their behavior once they reach or exceed a critical temperature T_C, which is a value governed by the material. At T_C the materials DC resistance drops to zero. In order to get an accurate device measurement when a superconductor is at operating temperature, a new calibration is necessary. This is often impossible due to the fact that the devices are under vacuum to achieve cryogenic temperatures. A room temp calibration file will not be valid at cryogenic temperatures. There exists a drift from nominal measurement. New methods of calibration must be explored.

4.2.1 Previous Calibration Work

Among the challenges to calibrating devices at cryogenic temperatures is that the DUT is physically isolated inside a cryostat. A manual calibration can be done wherein the calibration standards such as open, short, and load are individually cooled down and measured. This process is extremely time consuming as it requires a cool down and warm up cycle for each standard and then the DUT for a minimum

on average of four cycles. This assumes nothing goes wrong in the process. Replacing the calibration standards after each cycle actively changes the environment for the next cycle. Cables can be unintentionally bent or moved. Moreover is that the standards have a different physical size and footprint. This changes how low the temperature can get inside the cryostat. Each standard should be recorded under the exact same conditions. Without temperature control of the main cryogenic stage there exists a small window to be able to take the measurement. Missing this could lead to an entire restart of the calibration sequence. All of these things add uncertainty to the final measurement. Diego (2010) used a hybrid electronic TRL method, where they cooled the DUT on a custom circuit board, but measured each standard using the manually at room temp. The custom printed circuit board was designed so the TRL standards and a DUT would have the same length of transmission between each. They used a room temperature electronic calibration kit to compare to their TRL board. They averaged the attempts and used VNA software to make their own error matrix for the TRL board and subtract that from the DUT measurement.

Other options exist, like control-arms that can be manipulated from outside the vacuum chamber, but these are subject to mechanical failure when temperatures drop in the low $\sim$ milli-kelvin range. RF switches have existed for a long time but only recently have commercially available ones been developed that can survive repeated cryogenic warm-cold-warm cycles. Even still using switches for calibration adds an uncertainty from the fact that the physical length between switch traces is not equivalent. The point of calibration being to remove the interconnect between DUT and VNA, so it is always this same interconnect that the cal standards are attached to. In order for a switching method to work, separate channels would

have to appear as an identical electrical length. Switches aslo tend to be bulky and take up space in the small vacuum chamber. They also require DC wiring to be controlled. Vacuum systems tend to limit the amount of external wiring going into the chamber as that introduces more external heat to the system.

Still, some switches have been used effectively in the past. It is only in the recent decade or so that these techniques became something that approaches viable. Microwave devices have been measured using RF switches with custom TRL calibrations (Slichter 2011; Ranzani et al. 2012; Ranzani et al. 2013) but a one-port OSL cal for connector based devices has not been done in a single cycle.

In my masters thesis (Neric 2023) I developed three different schemes for one port in-situ OSL cryogenic calibration. One method used a custom build SP4T circuit board, the second was to use my eight-channel flexible ribbon, and the third was a method using a commercial-off-the-shelf first of a kind cryogenic RF switch. The goal was to do a trade-study on the most accurate method. While I had anticipated both the flex circuit and COTS switch to work, the flex connectors (SMP press-on type) did not allow for the flex approach to achieve sufficient trace repeatability. Only the cryogenic SP6T switch provided the necessary measurement accuracy to achieve the calibration.

4.2.2 Calibration Techniques

The main technique I developed was for a one port vacuum cryo in-situ calibration of a vector network analyzer (VNA) using commercial off the shelf (COTS) RF latching electro-mechanical switches. This procedure was developed for use in a closed cycle helium 4 K cryogenic test bench to measure the reflection coefficient

of a single port connectorized DUT, which was loaded onto a cold plate alongside OSL calibration standards. The RF switch allowed for the calibration and device measurement to be carried out in a single thermal cycle as opposed to a minimum of four cycles. Three of those four cycles were needed for a three-term VNA error correction, which was required for industry standard device calibration. This test procedure has been carried out on an arbitrary DUT at $\sim$ 3K temperature, over a 6 GHz bandwidth. However, the goal was to develop a setup and procedure for measuring the frequency and temperature dependent complex impedance of superconducting non-linear devices. The calibration standards were Keysight 85033D mechanical DC – 6 GHz SMA open-short-load standards. The switch used was a cryogenic electro-mechanical single pole six-throw (SP6T) latching DC – 18 GHz switch from Radiall. The calibration standards can be seen in Figure 45, and the full setup for a generic RF DUT can be seen in Figure 46. The DUT was a very basic RLC circuit which was predictable in behavior. Figure 47 shows the results of the cryo calibration (Neric 2023). The original room temperature measurement of the RLC can be seen in the blue trace. The two additional traces are showing a calibration using manual techniques vs doing the calibration with a switch. Because the switch and manual method are in good agreement this signified the RF SP6T switch method was a success. The VNA test port power for all testing was set to P = - 20 dBm. The frequency span was from 0.10 - 6.00 GHz. The IF bandwidth was 10 HZ, I was averaging 16 times and with 201 points. The same process would be repeated now for a non-linear device.

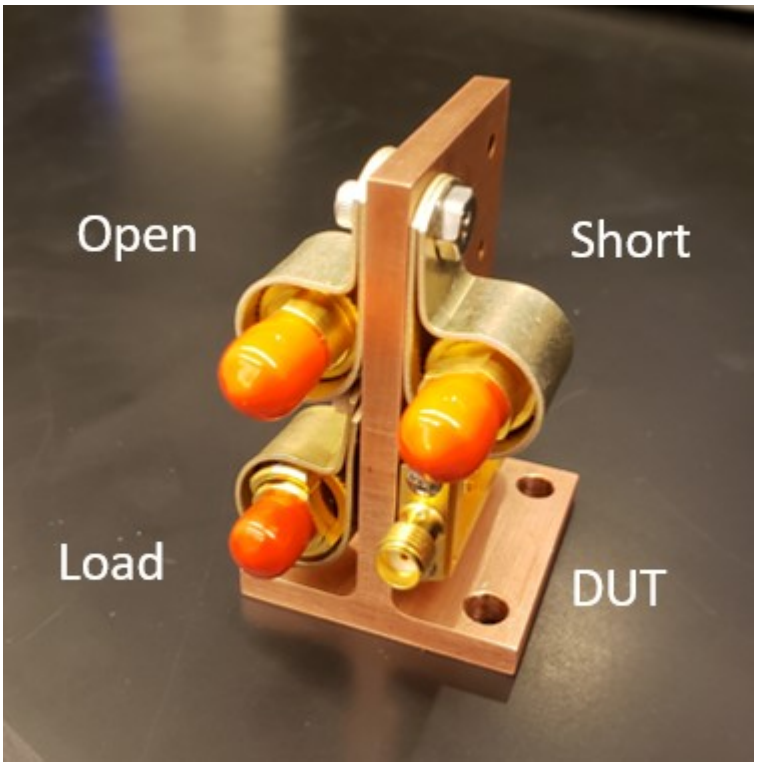

Figure 45. Calibration Standards

Note: Cryo cal standards attached to a heat-sinking copper stand. The red and orange end caps are dust covers for the SMA connector. The DUT is shown without cover, but all connection types are equivalent SMA. Due to physical space constraints not all standards can be placed on the same tower as was the original intent.

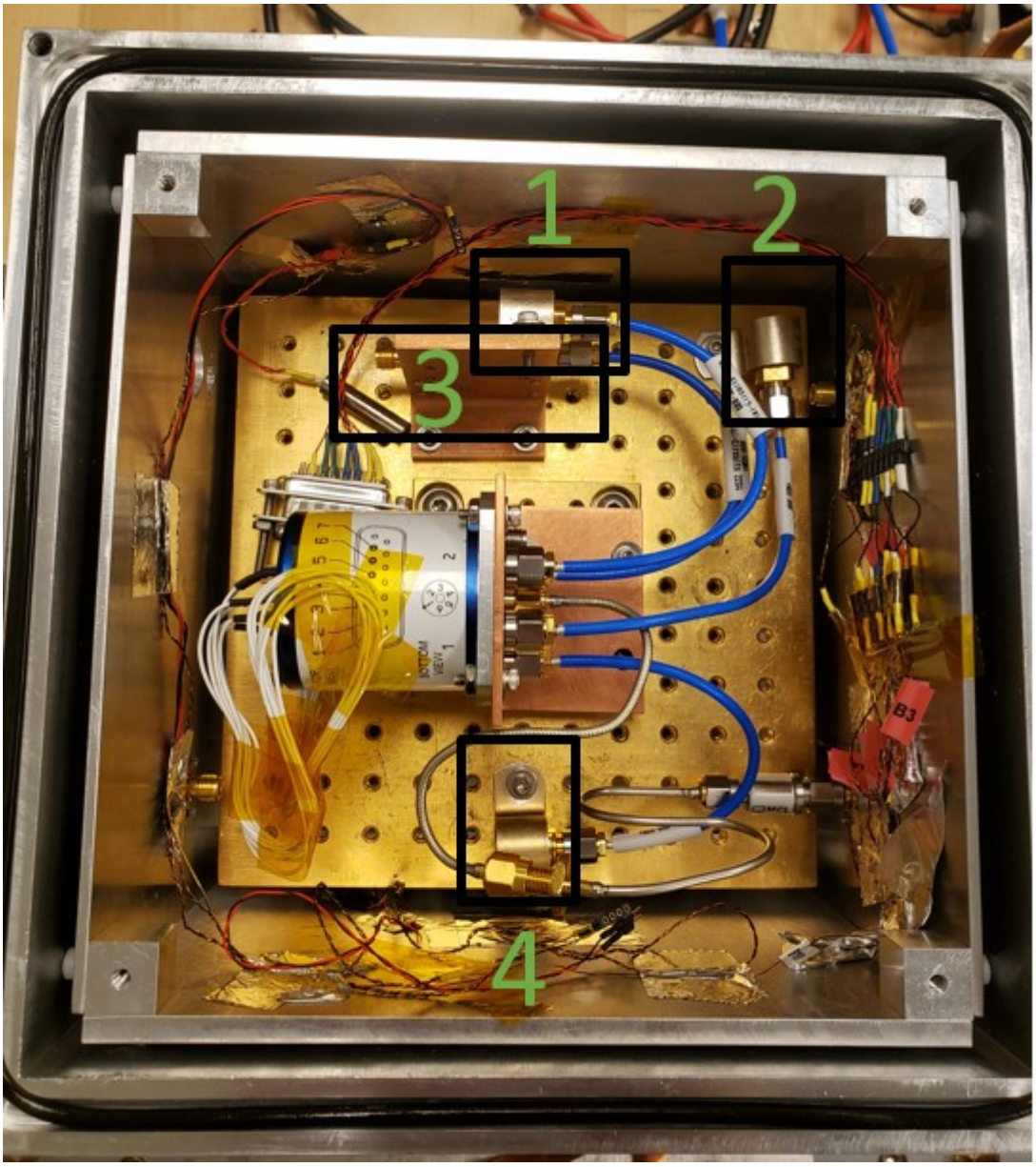

Figure 46. Cryogenic Calibration Test Set-up

Note: Pictured here is ASU's 10 K cryogenic test bed. A 10 K gold plated cold plate can be seen in the background. The calibration standards are outlined in black and labeled as (1) Short, (2) Open (3) DUT with heat bracket, and (4) matched 50 Ω load. The DUT and the short were attached to the same heating stand which is where the temperature sensor was affixed. The open and load standards were clamped directly to the 10 K plate so that the blue Mini-Circuits coax cables would not bend extremely and become damaged.

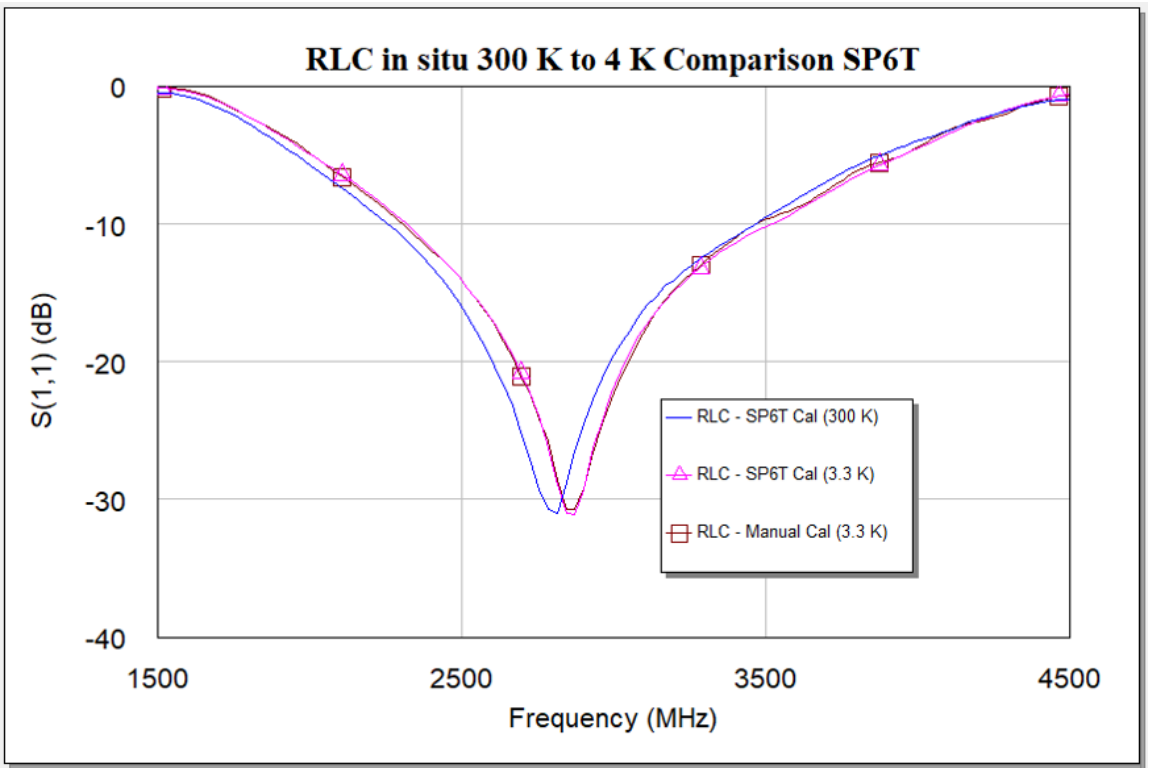

Figure 47. Cryogenic Vacuum In-situ Measurement: RLC

Note: A basic RLC circuit measured at room temperature 300 K (blue), and at 3.3 K using RF switches (pink) and manually calibrating standards (brown).

4.2.3 HEB Previous Methodology

Experimental characterization of the complex temperature and frequency dependent mixer impedance has been carried out in the past. Rodriguez-Morales and Yngvesson (2003) took noise and impedance measurements. Their impedance measurement included a 4 K TRL calibration, however this was done on a device without an antenna, and therefore not a complete system picture. Also the TRL calibration had limited bandwidth. Another approach used the HEB itself as two points of calibration which can be seen in Kooi et al. (2007). The authors used the HEB at 20 K temperature to stand in as a known load impedance, and then below T_C as a short. They used an alternate method as well with simulations to de-embed the measurement. The authors then compared their results to the NSGR model. This approach was in agreement with theory but did not use industry standard calibration references so there is still uncertainty. A very robust approach is presented in Rodriguez-Morales, Yngvesson, and Gu (2010) wherein calibration is done via manual OSL over multiple cycles. The devices were tested with several LO frequencies up to 2 THz and compared their results to the several impedance models, two of which were briefly discussed in section 4.1.1. The cryogenic calibration I developed would accomplish the same measurement in a single cycle. Not only that, but the ability to re-calibrate if temperature changes improves the accuracy of the overall setup.

4.3 HEB Cryogenic Measurements

A 1.9 THz mixer had been sent for testing with the GUSTO IF chain in 2018. The cryo-calibration setup was not developed until 2022. The mixer was stored for four years in a Hammond box to protect for electrical discharges, but not in vacuum. As a result the superconducting thin film was exposed to air for the entire time. There were concerns that the HEB would no longer be operable after all that oxygen exposure, but initial testing was promising. A high precision Keithly source meter with four-wire sense was used to bias the mixer at 86 μA and measured impedance of 107.6 Ω at 300 K. These values were considered high, but still in an operable range. The HEB was carefully installed for the cryogenic measurement and brought to $\sim$ 4 K temperature. The critical temperature $T_C \sim 11$ K was met, but despite reaching lower temperatures, no superconducting effects were observed. Biasing the HEB was expected to be challenging, as the circuit used in the bias network was not with the HEB, and I had thought perhaps the setup using the source meter was the problem. The four kelvin test bed was equipped for a T_C measurement of generic superconducting films and devices. This test procedure was designed to measure the bounds of critical temperature for an unknown sample. When this was attempted for the SRON HEB no critical temperature could be found for the mixer. It became clear than that the quality of the material had degraded due to oxidation. No new HEB mixer could be provided in time for a follow up measurement, and no facilities were available for repair of the mixer. This ultimately concludes where my attempts to measure the HEB ended, however my test setup was designed such that any new user could quickly and efficiently implement the technique. When such a time comes that another mixer is available for testing, the lesson learned here is to keep the

device under vacuum when storing, and only when ready for measurement should it be removed. The setup is not limited to HEBs, any superconducting device with an SMA output could be tested. One such device is discussed in the following section.

4.4 Kinetic Inductance Magnetometer (KIM)

The next superconducting non linear device I attempted to measure was the Kinetic Inductance Magnetometer (KIM) (Luomahaara et al. 2014). The KIM belongs to the family of direct detection sensors known as kinetic inductance detectors (KIDs). The term kinetic inductance refers to inductance that arises from the motion of charge carrying particles through a medium. KIMs sense magnetic fields by exploiting the phenomena of kinetic inductance within nanowires, which are nano-scale threads used in single photon detectors (Marsili et al. 2013) to increase their effective area (Zadeh et al. 2021). The full design and theory of the KIMs is outside the scope of this work, but the basics of kinetic inductance (L_k) and the the device features are important to understanding measured results. When a superconducting device is below the critical temperature T_C the direct current resistance of the superconductor drops to zero. The charge carriers no longer move as independent electrons, but bind together in groups of two, known as cooper pairs (Bardeen, Cooper, and Schrieffer 1957). Cooper pairs can be disrupted or broken apart by photon or phonon interactions. The broken cooper pairs change the number of charge carriers and therefore the kinetic inductance. KIDs work by measuring the change in L_k.

The total inductance of a conductor is $L_{tot} = L_g + L_k$, where L_k is the kinetic inductance that arises from the inertial mass of charge carriers and L_g is the initial

geometric inductance linked to the physical attributes of the object. L_k is usually negligible for most room temperature and low frequency applications, but cannot be ignored in the conservation of energy of a superconducting device below T_C. For a wire of length ℓ, cross-sectional area A, and charge carriers with electric charge e, number density n_e and velocity v one can write the energy as

$$\varepsilon = \frac{1}{2}L_g I^2 + \frac{1}{2}Mv^2 \tag{4.8}$$

The variable I is the current through the wire. The second part of this equation is the classical kinetic energy where M is the total mass of charge carriers and v is velocity. The total mass of charge carriers can be written as $M = m_e n_e A\ell$ where m_e is the mass of the individual electrons. The current through the wire can be written in terms of velocity $I = An_e ev \implies v = I/An_e e$. Plugging M and v back into equation 4.8 and simplifying leads to:

$$\varepsilon = \frac{1}{2}L_i I^2 + \frac{1}{2}\frac{\ell m_e}{An_e e^2}I^2 \tag{4.9}$$

From which we can identify and define the kinetic inductance as:

$$L_k = \frac{\ell m_e}{An_e e^2} \tag{4.10}$$

$$\varepsilon = \frac{1}{2}L_i I^2 + \frac{1}{2}L_k I^2 = \frac{1}{2}(L_i + L_k)I^2 \tag{4.11}$$

KIDs are a type of resonator. A very basic and common lumped element resonator is known as the tank circuit where an inductor and capacitor are in parallel. This type of circuit has an intrinsic resonance frequency when the energy in the capacitor is equal to the energy of the inductor. That frequency can be written as:

$$\omega_0 = \frac{1}{\sqrt{LC}} \tag{4.12}$$

Here ω_0 is in the angular form of frequency where $\omega = 2\pi$f. The quality factor of a resonator circuit is proportional how much energy is stored vs how much is dissipated and can be written in terms of capacitance, inductance, and resistance (Doyle et al. 2008).

$$Q = \omega_0 RC = \frac{R}{\omega_0 L} \tag{4.13}$$

4.4.1 Cryogenic Measurements

Using the procedure detailed in section 4.2.2, I installed the KIM in a four kelvin closed cycle system. The four kelvin system affectionately known as "Forky," was chosen over the 10 K system in order to get below the T_C of certain superconducting materials. The rest of the test setup was the same, only this time I was able to reach much lower temperatures at the expense of having less space to work with. The results of the measurement can be seen in Figure 48.

The 300 K room temperature data can be seen as the blue trace. A very pronounced resonance can be seen in both of the cryogenic data sets. The pink trace illustrates what happens when the VNA is not re-calibrated for lower temperatures. Standing waves induce a ripple effect in the resonator's response. There is also some gain in the pink trace that is an artifact of the room temperature calibration. The brown trace shows the KIM response after cryogenic calibration at 3.5 K. The change from the room temperature (blue) to the cryogenic (brown) trace clearly shows a change in behavior when the DUT reach $T \leq T_C$. The behavior of the

circuit went from largely reflecting signal back to having a sharp resonance. This unfortunately, was not exactly what was anticipated. The resonance of the KIM was expected to have multiple small harmonics and half of the resonance peak.

The measured S_{11} was certainly that of a superconducting device but not that of the designed resonator. The circuit was built on a CPW transmission line made of superconducting NbN material. It became quickly obvious that I had measured the transmission line of the KIM alone and not the resonator circuit. The reason for this was that the inductive component of the KIM was a pair of NbN nanowires. The nanowire was very small and therefore sensitive to thermal transfer. The test port of the VNA was outputting -20 dBm of which translates to 1.0×10^{-5} W of power. The dimensions of the nanowires in the KIM are thickens d $\sim$ 20 nm, $\ell \sim$ 500 nm, and sheet resistance $R_{\square} \sim 165\ \Omega/\square$ (Sypkens et al. 2021). Sheet resistance is a measure of resistance of a material with uniform thickness which is related to the total or bulk resistance by the length (ℓ) and width (w) of the material: $R = R_{\square}\ell w^{-1}$ The sheet resistance uses $\square$ notation to not be confused with the bulk resistance. Power dissipated through the nanowire will cause a change in temperature following:

$$P = \frac{\kappa A \Delta T}{\ell} \tag{4.14}$$

Where κ is the thermal conductivity of the material in units of W m^{-1} K^{-1}, A is the surface area in m^2 and ℓ is the length of the wire. To calculate thermal conductivity for the NbN nanowire: $\kappa = LT\rho^{-1}$ according to the Widemann-Franz law, and $L = 2.45 \times 10^{-8}$ WΩK^{-2} which is the Lorenz number (Yang et al. 2007). The resistivity of the material can be found by $\rho = R_{\square}d$ (Baeva et al. 2018). For the KIM nanowires I found that $\rho = 3.3 \times 10^{-6}\ \Omega$m and $\kappa = 33.4 \times 10^{-2}$ W m^{-1} K^{-1}. For a 500 nm length of nanowire it would only take $\sim 10^{-5}$ W of power to

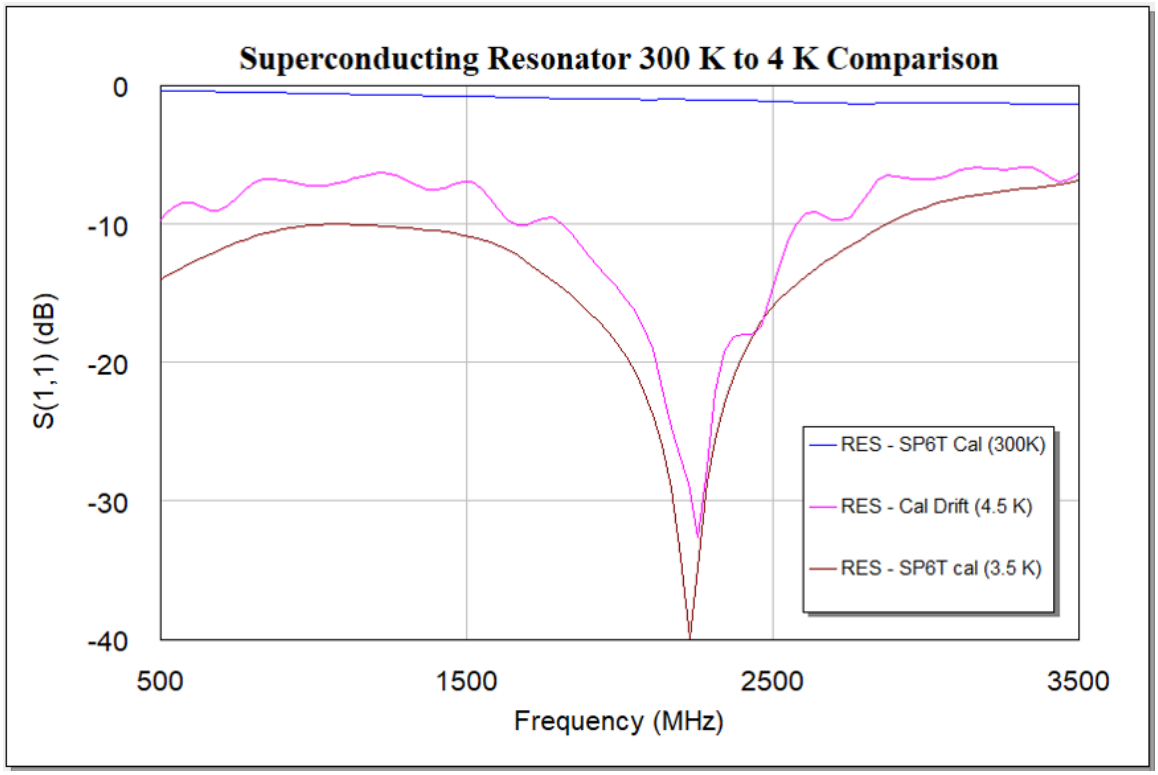

Figure 48. Cryogenic Vacuum In-situ Measurement: KIM TL

Note: A Kinetic Inductance Magnetometer (KIM) superconducting Transmission line measured at room temperature 300 K (blue), and at 3.3 K using RF switches (brown). The pink trace demonstrates how a room temperature calibration can fluctuate or drift from the true value of S_{11} and therefore impedance.

warm the nanowire back up to room temperature if it were entirely absorbed by the superconducting wire. Only 3% of that power would be needed to bring the nanowire above T_C. Power absorbed by the KIM would be in that range for this setup.

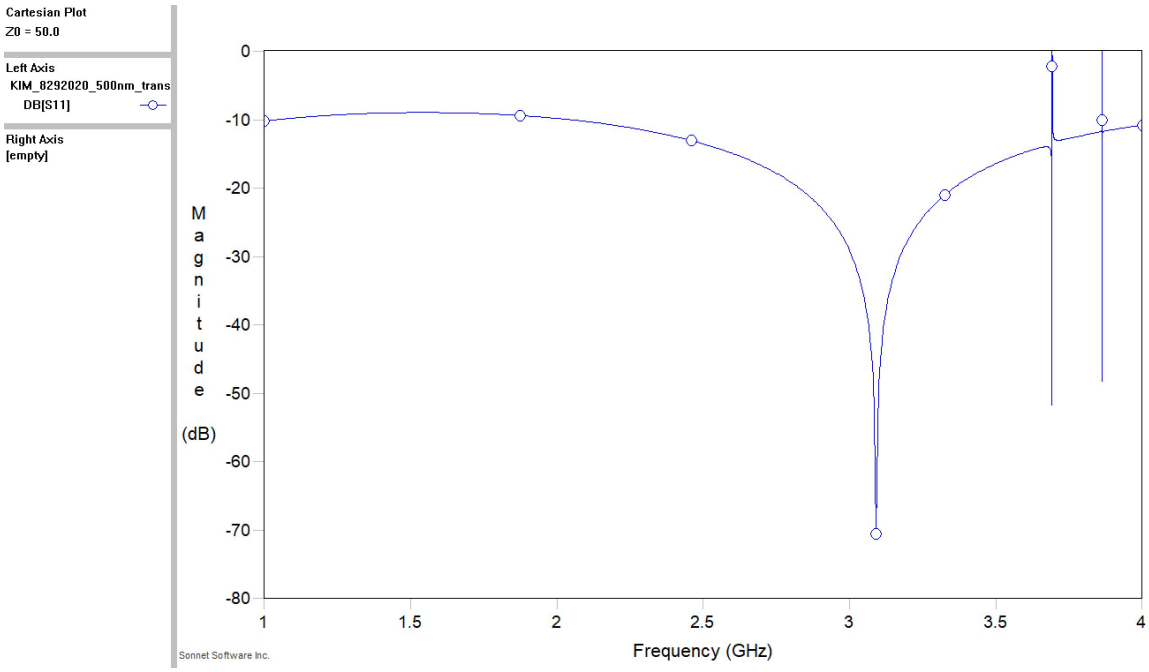

Figure 49. Simulation: KIM TL

Note: A sonnet simulation of the microwave transmission line of the kinetic inductance magnetometer (KIM). The results are magnitude of S_{11} in units of dB.

Typically low power settings, and attenuators are used to measure the KIM with a VNA. The problem is that this brings the measurement to the noise floor of the network analyzer, meaning that the S_{11} measurements are not nearly as reliable under those circumstances. A 1-port impedance measurement with the available VNA is not possible. It is however possible to compare the measurement of the CPW transmission line with that of simulation. The line was also made of superconducting material so it could be used to validate this approach for non linear devices. Figure 49 shows a sonnet simulation for the transmission line. This image compared to Figure 48 shows a similar shape but the resonant frequency location and depth are not equivalent. It is important to note that the actual measurement was carried out at 3.5 K and, the sonnet simulation for the transmission line was at higher temperature. The resonant frequency and quality factor are temperature dependent (Mauskopf 2018). The simulation is that of the CPW alone. It does not include loss effects from device package, wire-bonds, or solder to coax output ports. All those factors will contribute to a departure from the simulation. The fact that the general shape qualitatively matches a resonator, and that the effect is only seen when the NbN is superconducting, indicates that the calibration was effectively done on a superconducting non-linear device in an operating state. There is also evidence that a standing wave was removed during calibration at cryogenic temperatures. This general purpose 1-port in-situ calibration method has been validated at 1-4 GHz for a regular RLC circuit, and a superconducting transmission line at cryogenic temperatures. A full measurement of an HEB at multiple LO points is a high priority to follow this work. Until one becomes available for testing, several other superconducting devices may be tested instead, and even the KIM measurement may be repeated with a different VNA with lower noise floor.

Chapter 5

FUTURE WORK

As I discussed in introductory chapters and for part of my work on the ancillary data for ASTHROS, section 2.1, the field of THz astronomy is still a largely unexplored frontier in astrophysics. Not only are there great opportunities to study the science behind the ISM, but to evolve and advance the technology driving measurements. The science objectives are clear. Observing the galaxy in THz emission lines is an absolute necessity to completing our knowledge of star formation and galaxy evolution. It is of critical importance that surveys of [CII] are done to identify regions and targets of interest especially molecular clouds in transition. With maps of potential H-to-H_2 transition, deep targeted surveys will use [NII] to probe the physical structure and distribution of the clouds in three dimensions. These strategies will be vetted by the GUSTO and ASTHROS missions and be the standard for comparison in THz study.

Looking to the horizon, in the figurative and literal sense, future missions are currently in the works making use of heterodyne THz technology (Kawamura et al. 2020). As these systems mature they will grow in pixel density, and detector complexity. It has been my goal to optimize THz systems, and develop tools that will scale up with the instrument advancements in adjacent fields. The flexible printed circuit stripline-based transmission lines I designed will fly for the first time on GUSTO. They are a step in the right direction to reduce the heat load, form-factor and footprint of the IF transmission system. With cold performance comparable to industry standard alternatives at a better price point for larger missions, they will

be an excellent choice to support new THz missions. The technology as it stands can still be improved upon. The fact that they are large scale printed circuits means that they do not have to serve solely as passive transmission lines. Electronics can be built-in to the ribbon such as amplifiers. This effectively moves more of the IF chain into the same package. The cables transmit DC as well as RF so that opens the possibility of increasing a cryostat's test and use ability for both ground based test benches, and airborne mission systems. Added surface mounted switches to the warm output of the flex lines could also be possible. This could make the flex circuit capable of limited self calibration. Different connector types and orientations are also well worth investigating to ensure the flex circuit can provide signal transmission for a myriad of vacuum systems and missions.

Like the flex circuits, the cryogenic calibration test setup also has the potential to positively impact not only future astronomy missions but also any vacuum cryogenic experiments where no alternate calibration scheme has worked. Quantum computers for example, make use of cryostats with many coaxial transmission lines, and rely on precise instrument measurements. The flex lines alone would serve as an improvement, but coupled with a method for calibration in-situ they could immensely improve measurement precision. Combining device calibration and the flex circuit was one of my earlier goals, however this was not achieved in my time as a graduate student. I will continue to push for this merger of technologies because, with a calibration scheme adapted to work with the flex circuit it would be possible to characterized an entire IF system end-to-end.

For now the future of the flex circuit as a transmission line is more clear. A new set of flex circuits are being prepared for the Advanced Cryogenic L-band Phased Array Camera for the Arecibo Radio Telescope (ALPACA) (Cortes-Medellin

et al. 2015). ALPACA was an instrument originally designed for the 305 m radio telescope at the Arecibo Observatory in Puerto Rico (Parshley et al. 2020). The Eight channel ribbon is the same design as pictured in Figure 42. The 6 m CCAT-prime telescope at Cerro Chajnantor in Chile with a wide field of view is being equipped with instruments for several bands of study (Stacey et al. 2018). This includes the ability to map [CII] (Karoumpis et al. 2022). Prime-Cam is a first light instrument of CCAT-prime with several modules including that of [CII] as well as other cosmology focused instruments (Vavagiakis et al. 2018). For Prime-Cam I am designing 6-channel ribbons. The success of these missions will influence further design of the flex circuits.

REFERENCES

Baeva, E. M., M. V. Sidorova, A. A. Korneev, K. V. Smirnov, A. V. Divochy, P. V. Morozov, P. I. Zolotov, et al. 2018. "Thermal Properties of NbN Single-Photon Detectors." *Physical Review Applied* 10 (6). https://doi.org/10.1103/PhysRevApplied.10.064063.

Bardeen, J., L. N. Cooper, and J. R. Schrieffer. 1957. "Theory of superconductivity." *Physical Review* 108 (5). https://doi.org/10.1103/PhysRev.108.1175.

Barrett, Robert M. 1955. "Microwave printed circuits - a historical survey." *IRE Transactions on Microwave Theory and Techniques* MTT-3 (2). https://doi.org/10.1109/TMTT.1955.1124910.

Bolatto, Alberto D., Mark Wolfire, and Adam K. Leroy. 2013. "The CO-to-H_2 Conversion Factor." *Annual Review of Astronomy and Astrophysics* 51 (1): 207–268. https://doi.org/10.1146/annurev-astro-082812-140944.

Braiding, Catherine, M. G. Burton, R. Blackwell, C. Glück, J. Hawkes, C. Kulesa, N. Maxted, et al. 2015. "The Mopra Southern Galactic Plane CO Survey-Data Release 1." *Publications of the Astronomical Society of Australia* 32. https://doi.org/10.1017/pasa.2015.20.

Braiding, Catherine, G. F. Wong, N. I. Maxted, D. Romano, M. G. Burton, R. Blackwell, M. D. Filipović, et al. 2018. "The Mopra Southern galactic plane CO survey-Data release 3." *Publications of the Astronomical Society of Australia* 35. https://doi.org/10.1017/pasa.2018.18. arXiv: 1902.04249.

Brooks, K. J., P. Cox, N. Schneider, J. W.V. Storey, A. Poglitsch, N. Geis, and L. Bronfman. 2003. "The Trumpier 14 photodissociation region in the Carina Nebula." *Astronomy and Astrophysics* 412 (3): 751–765. https://doi.org/10.1051/0004-6361:20031406.

Brussaard, P. J., and H. C. Van De Hulst. 1962. "Approximation formulas for nonrelativistic bremsstrahlung and average gaunt factors for a maxwellian electron gas." *Reviews of Modern Physics* 34 (3): 507–520. https://doi.org/10.1103/RevModPhys.34.507.

Burton, Michael G., C. Braiding, C. Glueck, P. Goldsmith, J. Hawkes, D. J. Hollenbach, C. Kulesa, et al. 2013. *The mopra Southern galactic plane CO survey,* 1. https://doi.org/10.1017/pasa.2013.22. arXiv: 1307.1027.

Busch, Michael P., Ronald J. Allen, Philip D. Engelke, David E. Hogg, David A. Neufeld, and Mark G. Wolfire. 2019. "The Structure of Dark Molecular Gas in the Galaxy. II. Physical State of "CO-dark" Gas in the Perseus Arm." *The Astrophysical Journal* 883 (2). https://doi.org/10.3847/1538-4357/ab3a4b.

Casey, Sean C. 2004. "The SOFIA program: Astronomers return to the stratosphere." *Advances in Space Research* 34 (3). https://doi.org/10.1016/j.asr.2003.05.026.

Chengalur, Jayaram N., Nissim Kanekar, and Nirupam Roy. 2013. "Accurate measurement of the HI column density from HI 21 cm absorption-emission spectroscopy." *Monthly Notices of the Royal Astronomical Society* 432 (4): 3074–3079. https://doi.org/10.1093/mnras/stt658.

Chevance, Mélanie, Suzanne C. Madden, Christian Fischer, William D. Vacca, Vianney Lebouteiller, Dario Fadda, Frédéric Galliano, et al. 2020. "The CO-dark molecular gas mass in 30 Doradus." *Monthly Notices of the Royal Astronomical Society* 494 (4). https://doi.org/10.1093/mnras/staa1106.

Cortes-Medellin, German, Amit Vishwas, Stephen C. Parshley, Donald B. Campbell, Phil Perilatt, Richard Black, Jay Brady, Karl F. Warnick, and Brian D. Jeffs. 2015. "A fully cryogenic phased array camera for radio astronomy." *IEEE Transactions on Antennas and Propagation* 63 (6). https://doi.org/10.1109/TAP.2015.2415527.

Couëdo, F., L. Bergé, L. Dumoulin, M. Aprili, C. A. Marrache-Kikuchi, and J. Gabelli. 2019. "Sample-based calibration for cryogenic broadband microwave reflectometry measurements." *AIP Advances* 9 (7). https://doi.org/10.1063/1.5097897.

Cubek et al. 2023. "Ph.D. Thesis." *In preperation.*

Dahmen, G., S. Hüttemeister, T. L. Wilson, R. Mauersberger, A. Linhart, L. Bronfman, A. R. Tieftrunk, et al. 1997. "Molecular gas in the Galactic Center Region." *Astronomy and Astrophysics Supplement Series* 126 (2): 197–236. https://doi.org/10.1051/aas:1997389.

De Avillez, Miguel A., and Dieter Breitschwerdt. 2015. "Temperature-averaged and total free-free Gaunt factors for κ and Maxwellian distributions of electrons." *Astronomy and Astrophysics* 580. https://doi.org/10.1051/0004-6361/201526104.

Diego, Juan Cano de. 2010. "Cryogenic Technology in the Microwave Engineering: Application to MIC and MMIC Very Low Noise Amplifier Design." *Tesis Doctorales en Red (TDR).*

Doyle, Simon, P. Mauskopf, J. Naylon, A. Porch, and C. Duncombe. 2008. "Lumped element kinetic inductance detectors." *Journal of Low Temperature Physics* 151 (1-2 PART 1). https://doi.org/10.1007/s10909-007-9685-2.

Draine, Bruce T. 2010. *Physics of the interstellar and intergalactic medium,* 4–9. https://doi.org/10.2307/j.ctvcm4hzr.

Ekström, Hans, Boris S. Karasik, Erik L. Kollberg, and K. Sigfrid Yngvesson. 1995. "Conversion Gain and Noise of Niobium Superconducting Hot-Electron-Mixers." *IEEE Transactions on Microwave Theory and Techniques* 43 (4). https://doi.org/10.1109/22.375258.

Erickson, E. F. 1995. "SOFIA: The next generation airborne observatory." *Space Science Reviews* 74 (1-2). https://doi.org/10.1007/BF00751257.

Field, G. B., D. W. Goldsmith, and H. J. Habing. 1969. "Cosmic-Ray Heating of the Interstellar Gas." *The Astrophysical Journal* 155. https://doi.org/10.1086/180324.

Fromm, W. E. 1955. "Characteristics and some applications of stripline components." *IRE Transactions on Microwave Theory and Techniques* MTT-3 (2). https://doi.org/10.1109/TMTT.1955.1124912.

Goldsmith, Paul F., Mark Heyer, Gopal Narayanan, Ronald Snell, Di Li, and Chris Brunt. 2008. "Large-Scale Structure of the Molecular Gas in Taurus Revealed by High Linear Dynamic Range Spectral Line Mapping." *The Astrophysical Journal* 680 (1): 428–445. https://doi.org/10.1086/587166. arXiv: 0802.2206.

Goldsmith, Paul F., Umut A. Yildiz, William D. Langer, and Jorge L. Pineda. 2015. "Herschel Galactic Plane Survey of [N II] Fine Structure Emission." *Astrophysical Journal* 814 (2). https://doi.org/10.1088/0004-637X/814/2/133.

Gousev, Yu P., G. N. Gol'Tsman, A. D. Semenov, E. M. Gershenzon, R. S. Nebosis, M. A. Heusinger, and K. F. Renk. 1994. "Broadband ultrafast superconducting NbN detector for electromagnetic radiation." *Journal of Applied Physics* 75 (7). https://doi.org/10.1063/1.356060.

Grenier, Isabelle A., Jean Marc Casandjian, and Régis Terrier. 2005. "Unveiling extensive clouds of dark gas in the solar neighborhood." *Science* 307 (5713). https://doi.org/10.1126/science.1106924.

Groppi, Christopher, Christopher Walker, Craig Kulesa, Dathon Golish, Patrick Pütz, Paul Gensheimer, Abby Hedden, et al. 2006. "Supercam : A 64 pixel superheterodyne camera."

Higgins, Ronan D., and Jacob W. Kooi. 2009. "Electrical standing waves in the HIFI HEB mixer amplifier chain," vol. 7215. https://doi.org/10.1117/12.811127.

Hollenbach, D. J., and A. G.G.M. Tielens. 1997. "Dense photodissociation regions (PDRs)." *Annual Review of Astronomy and Astrophysics* 35 (1). https://doi.org/10.1146/annurev.astro.35.1.179.

Karoumpis, C., B. Magnelli, E. Romano-Díaz, M. Haslbauer, and F. Bertoldi. 2022. "[CII] line intensity mapping the epoch of reionization with the Prime-Cam on FYST." *Astronomy and Astrophysics* 659. https://doi.org/10.1051/0004-6361/202141293.

Kawamura, Jonathan, Daniel Cunnane, Boris Karasik, Bruce Bumble, Darren Hayton, Imran Mehdi, Goutam Chattopadhyay, et al. 2020. "Development of THz Superconducting HEB Receiver Systems for Balloons, Aircraft, SmallSats and Future Large Missions."

Khosropanah, P., J. R. Gao, W. M. Laauwen, M. Hajenius, and T. M. Klapwijk. 2007. "Low noise NbN hot electron bolometer mixer at 4.3 THz." *Applied Physics Letters* 91 (22). https://doi.org/10.1063/1.2819534.

Klessen, Ralf S., and Simon C.O. Glover. 2015. "Physical processes in the interstellar medium." In *Star Formation in Galaxy Evolution: Connecting Numerical Models to Reality: Saas-Fee Advanced Course 43. Swiss Society for Astrophysics and Astronomy,* 4–18. https://doi.org/10.1007/978-3-662-47890-5_2.

Kooi, J. W., J. J.A. Baselmans, M. Hajenius, J. R. Gao, T. M. Klapwijk, P. Dieleman, A. Baryshev, and G. De Lange. 2007. "IF impedance and mixer gain of NbN hot electron bolometers." *Journal of Applied Physics* 101 (4). https://doi.org/10.1063/1.2400086.

Kuhn, Michael A., Lynne A. Hillenbrand, Alison Sills, Eric D. Feigelson, and Konstantin V. Getman. 2019. " Kinematics in Young Star Clusters and Associations with Gaia DR2." *The Astrophysical Journal* 870 (1): 32. https://doi.org/10.3847/1538-4357/aaef8c. arXiv: 1807.02115.

Langer, W. D., T. Velusamy, J. L. Pineda, P. F. Goldsmith, D. Li, and H. W. Yorke. 2010. "C+ detection of warm dark gas in diffuse clouds." *Astronomy and Astrophysics* 521 (1). https://doi.org/10.1051/0004-6361/201015088.

Liszt, H. S., and J. Pety. 2012. "Imaging diffuse clouds: Bright and dark gas mapped in CO." *Astronomy and Astrophysics* 541. https://doi.org/10.1051/0004-6361/201218771.

Luomahaara, Juho, Visa Vesterinen, Leif Grönberg, and Juha Hassel. 2014. "Kinetic inductance magnetometer." *Nature Communications* 5. https://doi.org/10.1038/ncomms5872.

Madden, S. C., D. Cormier, S. Hony, V. Lebouteiller, N. Abel, M. Galametz, I. De Looze, et al. 2020. "Tracing the total molecular gas in galaxies: [CII] and the CO-dark gas." *Astronomy and Astrophysics* 643. https://doi.org/10.1051/0004-6361/202038860.

Mani, Hamdi, and Philip Mauskopf. 2014. "A single-stage cryogenic LNA with low power consumption using a commercial SiGe HBT." https://doi.org/10.1109/WOLTE.2014.6881015.

Marsili, F., V. B. Verma, J. A. Stern, S. Harrington, A. E. Lita, T. Gerrits, I. Vayshenker, et al. 2013. "Detecting single infrared photons with 93% system efficiency." *Nature Photonics* 7 (3). https://doi.org/10.1038/nphoton.2013.13.

Mauskopf, P. D. 2018. "Transition edge sensors and kinetic inductance detectors in astronomical instruments." *Publications of the Astronomical Society of the Pacific* 130 (990). https://doi.org/10.1088/1538-3873/aabaf0.

McGarey, Patrick, Hamdi Mani, Caleb Wheeler, and Christopher Groppi. 2014. "A 16-channel flex circuit for cryogenic microwave signal transmission." In *Millimeter, Submillimeter, and Far-Infrared Detectors and Instrumentation for Astronomy VII,* vol. 9153, 91532F. https://doi.org/10.1117/12.2055472.

McKee, C. F., and J. P. Ostriker. 1977. "A theory of the interstellar medium - Three components regulated by supernova explosions in an inhomogeneous substrate." *The Astrophysical Journal* 218. https://doi.org/10.1086/155667.

McKee, Christopher F., and Mark R. Krumholz. 2010. "The atomic-to-molecular transition in galaxies. III. A new method for determining the molecular content of primordial and dusty clouds." *Astrophysical Journal* 709 (1): 308–320. https://doi.org/10.1088/0004-637X/709/1/308. arXiv: 0908.0330.

Merkel, Harald. 1999. "A hot-spot mixer model for phonon-cooled nbn hot electron bolometric mixers." *IEEE Transactions on Applied Superconductivity* 9 (2 PART 3). https://doi.org/10.1109/77.783951.

Molinari, S., B. Swinyard, J. Bally, M. Barlow, J.-P. Bernard, P. Martin, T. Moore, et al. 2010. "Hi-GAL: The Herschel Infrared Galactic Plane Survey." *Publications of the Astronomical Society of the Pacific* 122 (889): 314–325. https://doi.org/10.1086/651314. arXiv: 1001.2106.

Nebosis, R. S., Yu. P. Semenov, and K. F. Renk. 1996. "Rigorous Analysis of a Superconducting Hot-Electron Bolometer Mixer: Theory and Comparison with Experiment."

Neric, Marko, Christopher E. Groppi, Hamdi Mani, Justin Mathewson, Kristina Davis, Matthew Underhill, Craig Kulesa, Christopher Walker, Thomas Mozdzen, and Abram Young. 2018. "IF system design for the Galactic/Extragalactic ULDB Spectroscopic Terahertz Observatory (GUSTO)," 101. https://doi.org/10.1117/12.2314096.

Neric, Marko, Hamdi Mani, Thomas Mozdzen, and Chris Groppi. 2019. "Design and Prototyping of New Flexible Stripline based Transmission Lines as Alternatives to Semi-Rigid Coaxial Cables." In *ISSTT 2019 - 30th International Symposium on Space Terahertz Technology, Proceedings Book,* 69–71.

Neric, Marko, Hamdi Mani, Thomas Mozdzen, and Chris Groppi. 2020. "Characterization of cryogenic flexible transmission lines designed for the GUSTO if harness." In *Proceedings of the 31st Symposium on Space Terahertz Technology, ISSTT 2020,* 50–53.

Neric, Marko. 2023. "M.S. Thesis." *In preperation.*

Oberst, T. E. 2009. "Submillimeter spectroscopy of the Carina Nebula: observations, operations and upgrades of the South Pole imaging Fabry-Perot interferometer." PhD diss., Cornell University.

Parshley, Stephen C., German Cortes-Medellin, Amit Vishwas, Donald B. Campbell, and Terry Herter. 2020. "Cryo-Mechanical Design of ALPACA: A Mixed-Material Radio-Frequency Transparent Vacuum Vessel Operating at 20 K." https://doi.org/10.1115/pvp2020-21818.

Pilbratt, G. L., J. R. Riedinger, T. Passvogel, G. Crone, D. Doyle, U. Gageur, A. M. Heras, et al. 2010. "Herschel Space Observatory." *Astronomy and Astrophysics* 518 (7-8). https://doi.org/10.1051/0004-6361/201014759.

Pineda, Jorge L., T. Velusamy, W. D. Langer, P. F. Goldsmith, D. Li, and H. W. Yorke. 2010. "A sample of [C II] clouds tracing dense clouds in weak FUV fields observed by Herschel." *Astronomy and Astrophysics* 521 (1). https://doi.org/10.1051/0004-6361/201015089. arXiv: 1007.5068.

Pineda, Jorge L., William D. Langer, Paul F. Goldsmith, Shinji Horiuchi, Thomas B. H. Kuiper, Erik Muller, Annie Hughes, et al. 2017. "Characterizing the Transition from Diffuse Atomic to Dense Molecular Clouds in the Magellanic Clouds with [C ii], [C i], and CO." *The Astrophysical Journal* 839 (2): 107. https://doi.org/10.3847/1538-4357/aa683a. arXiv: 1704.00739.

Pozar, David M. 2011. *Microwave engineering.* 178–187.

Preibisch, T., V. Roccatagliata, B. Gaczkowski, and T. Ratzka. 2012. "Herschel far-infrared observations of the Carina Nebula complex." *Astronomy & Astrophysics* 541:A132. https://doi.org/10.1051/0004-6361/201218851.

Ranzani, Leonardo, Lafe Spietz, Zoya Popovic, and Jose Aumentado. 2012. "A 4:1 transmission-line impedance transformer for broadband superconducting circuits." *IEEE Transactions on Applied Superconductivity* 22 (5). https://doi.org/10.1109/TASC.2012.2202116.

Ranzani, Leonardo, Lafe Spietz, Zoya Popovic, and José Aumentado. 2013. "Two-port microwave calibration at millikelvin temperatures." *Review of Scientific Instruments* 84 (3). https://doi.org/10.1063/1.4794910.

Rebolledo, David, Tony Wong, Rui Xue, Adam Leroy, Jin Koda, and Jennifer Donovan Meyer. 2015. "Scaling Relations of the Properties for CO Resolved Structures in Nearby Spiral Galaxies." *Astrophysical Journal* 808 (1). https://doi.org/10.1088/0004-637X/808/1/99. arXiv: 1506.05599.

Rebolledo, David, Michael Burton, Anne Green, Catherine Braiding, Sergio Molinari, Graeme Wong, Rebecca Blackwell, Davide Elia, and Eugenio Schisano. 2016. "The Carina Nebula and Gum 31 molecular complex - I. Molecular gas distribution, column densities, and dust temperatures." *Monthly Notices of the Royal Astronomical Society* 456 (3): 2406–2424. https://doi.org/10.1093/mnras/stv2776. arXiv: 1511.07513.

Rebolledo, David, Anne J. Green, Michael Burton, Kate Brooks, Shari L. Breen, B. M. Gaensler, Yanett Contreras, Catherine Braiding, and Cormac Purcell. 2017. "The Carina Nebula and Gum 31 molecular complex - II. The distribution of the atomic gas revealed in unprecedented detail." *Monthly Notices of the*

Royal Astronomical Society 472 (2): 1685–1704. https://doi.org/10.1093/MNRAS/STX2047. arXiv: 1708.02864.

Rebolledo, David, Anne J. Green, Michael G. Burton, Shari L. Breen, and Guido Garay. 2021. "The Carina Nebula and Gum 31 Molecular Complex. III. The Distribution of the 1–3 GHz Radio Continuum across the Whole Nebula." *The Astrophysical Journal* 909 (1): 93. https://doi.org/10.3847/1538-4357/abd7a3. arXiv: 2012.14872.

Roccatagliata, V., T. Preibisch, T. Ratzka, and B. Gaczkowski. 2013. "Herschel* far-infrared observations of the Carina Nebula complex** :III. Detailed cloud structure and feedback effects." *Astronomy and Astrophysics* 554. https://doi.org/10.1051/0004-6361/201321081. arXiv: 1303.5201.

Rodriguez-Morales, Fernando, and K. Sigfrid Yngvesson. 2003. "Impedance and Bandwidth Characterization of NbN Hot Electron Bolometric Mixers."

Rodriguez-Morales, Fernando, K. Sigfrid Yngvesson, and Dazhen Gu. 2010. "Wideband if-integrated terahertz HEB Mixers: Modeling and characterization." *IEEE Transactions on Microwave Theory and Techniques* 58 (5 PART 1). https://doi.org/10.1109/TMTT.2010.2045566.

Roelfsema, P. R., F. P. Helmich, D. Teyssier, V. Ossenkopf, P. Morris, M. Olberg, R. Shipman, et al. 2012. "In-orbit performance of Herschel-HIFI." *Astronomy and Astrophysics* 537. https://doi.org/10.1051/0004-6361/201015120.

Rosolowsky, Erik, and Adam Leroy. 2006. "Bias-free Measurement of Giant Molecular Cloud Properties." *Publications of the Astronomical Society of the Pacific* 118 (842): 590–610. https://doi.org/10.1086/502982.

Ryden, Barbara, and Richard W. Pogge. 2021. *Interstellar and Intergalactic Medium,* 1–30. https://doi.org/10.1017/9781108781596.

Schneider, N., V. Ossenkopf, T. Csengeri, R. S. Klessen, C. Federrath, P. Tremblin, P. Girichidis, S. Bontemps, and Ph André. 2015. "Understanding star formation in molecular clouds: I. Effects of line-of-sight contamination on the column density structure." *Astronomy and Astrophysics* 575. https://doi.org/10.1051/0004-6361/201423569. arXiv: 1403.2996.

Seo, Young Min, Paul F. Goldsmith, Christopher K. Walker, David J. Hollenbach, Mark G. Wolfire, Craig A. Kulesa, Volker Tolls, et al. 2019. "Probing ISM Structure in Trumpler 14 and Carina I Using the Stratospheric Terahertz

Observatory 2." *The Astrophysical Journal* 878 (2): 120. https://doi.org/10.3847/1538-4357/ab2043. arXiv: 1903.09517.

Siles, Jose V., Robert H. Lin, Choonsup Lee, Erich Schlecht, Alain Maestrini, Peter Bruneau, Alex Peralta, Jenna Kloosterman, Jon Kawamura, and Imran Mehdi. 2015. "Development of high-power multi-pixel LO Sources at 1.47 THz and 1.9 THz for astrophysics: Present and future."

Siles, Jose V., Jorge Pineda, Jonathan H. Kawamura, Cristopher Groppi, Pietro Bernasconi, Joshua Gundersen, and Paul F. Goldsmith. 2020. "ASTHROS-Astrophysics stratospheric telescope for high-spectral resolution observations at submillimeter-waves: Mission overview and development status."

Slichter, Daniel Huber. 2011. "Quantum Jumps and Measurement Backaction in a Superconducting Qubit." *Doctoral Thesis.*

Smith, Nathan. 2006. "A census of the Carina Nebula - I. Cumulative energy input from massive stars." *Monthly Notices of the Royal Astronomical Society* 367 (2): 763–772. https://doi.org/10.1111/j.1365-2966.2006.10007.x.

Smith, Rowan J., Simon C.O. Glover, Paul C. Clark, Ralf S. Klessen, and Volker Springel. 2014. "CO-dark gas and molecular filaments in milky way-type galaxies." *Monthly Notices of the Royal Astronomical Society* 441 (2). https://doi.org/10.1093/mnras/stu616.

Spietz, Lafe, Kent Irwin, Minhyea Lee, and Joś Aumentado. 2010. "Noise performance of lumped element direct current superconducting quantum interference device amplifiers in the 4-8 GHz range." *Applied Physics Letters* 97 (14). https://doi.org/10.1063/1.3497008.

Stacey, Gordon J., Nicholas Battaglia, Frank Bertoldi, Michel Fich, Martha P. Haynes, Terry L. Herter, Benjamin Magnelli, et al. 2018. "CCAT-Prime: science with an ultra-widefield submillimeter observatory on Cerro Chajnantor." https://doi.org/10.1117/12.2314031.

Sternberg, Amiel, Franck Le Petit, Evelyne Roueff, and Jacques Le Bourlot. 2014. "H I-TO-H2 transitions and H i column densities in galaxy star-forming regions." *Astrophysical Journal* 790 (1). https://doi.org/10.1088/0004-637X/790/1/10. arXiv: 1404.5042.

Sypkens, Sasha, Farzad Faramarzi, Marco Colangelo, Adrian Sinclair, Ryan Stephenson, Jacob Glasby, Peter Day, Karl Berggren, and Philip Mauskopf. 2021. "Development of an Array of Kinetic Inductance Magnetometers (KIMs)." *IEEE*

Transactions on Applied Superconductivity 31 (5). https://doi.org/10.1109/TASC.2021.3056322.

Tielens, A. G.G.M. 2005. *The physics and chemistry of the interstellar medium,* 2–6. https://doi.org/10.1017/CBO9780511819056.

Vavagiakis, Eve, Zeeshan Ahmed, Aamir Ali, Kaustuv Basu, Nicholas Battaglia, Frank Bertoldi, Richard Bond, et al. 2018. "Prime-Cam: a first-light instrument for the CCAT-prime telescope." https://doi.org/10.1117/12.2313868.

Velusamy, T., W. D. Langer, J. L. Pineda, P. F. Goldsmith, D. Li, and H. W. Yorke. 2010. "(CII) observations of H2 molecular layers in transition clouds." *Astronomy and Astrophysics* 521 (1). https://doi.org/10.1051/0004-6361/201015091. arXiv: 1007.3338.

Walker, C., C. Kulesa, P. Bernasconi, H. Eaton, N. Rolander, C. Groppi, J. Kloosterman, et al. 2010. "The Stratospheric THz Observatory (STO)," vol. 7733. https://doi.org/10.1117/12.857765.

Walker, Christopher K. 2015a. "SuperCam: A 64 pixel SIS receiver array for submillimeter-wave astronomy." In *2015 IEEE MTT-S International Microwave Symposium, IMS 2015.* https://doi.org/10.1109/MWSYM.2015.7166873.

Walker, Christopher K. 2015b. *Terahertz Astronomy,* 1–10. https://doi.org/10.1201/b19111.

Walker, C. K., C. A. Kulesa, and Paul Goldsmith. 2020. "The gal/xgal ultra-long duration balloon-borne spectroscopic thz observatory (GUSTO)." In *Proceedings of the 31st Symposium on Space Terahertz Technology, ISSTT 2020,* 13.

Weinreb, Sander, Joseph C. Bardin, and Hamdi Mani. 2007. "Design of cryogenic SiGe low-noise amplifiers." *IEEE Transactions on Microwave Theory and Techniques* 55 (11). https://doi.org/10.1109/TMTT.2007.907729.

Wheeler, C. H. 2016. "Advancement of Heterodyne Focal Plane Arrays for Terahertz Astronomy." PhD diss., Arizona State University.

Wilson, Thomas L., Kristen Rohlfs, and Huttemeister Susanne. 2009. *Tools of Radio Astronomy,* 250–252. https://doi.org/10.1007/978-3-540-85122-6.

Wolfire, Mark G., David Hollenbach, and Christopher F. McKee. 2010. "The dark molecular gas." *Astrophysical Journal* 716 (2): 1191–1207. https://doi.org/10.1088/0004-637X/716/2/1191. arXiv: 1004.5401.

Wu, Ronin, Emeric Bron, Takashi Onaka, Franck Le Petit, Frédéric Galliano, David Languignon, Tomohiko Nakamura, and Yoko Okada. 2018. "Constraining physical conditions for the PDR of Trumpler 14 in the Carina Nebula." *Astronomy and Astrophysics* 618. https://doi.org/10.1051/0004-6361/201832595. arXiv: 1801.01643.

Yang, Joel K.W., Andrew J. Kerman, Eric A. Dauler, Vikas Anant, Kristine M. Rosfjord, and Karl K. Berggren. 2007. "Modeling the electrical and thermal response of superconducting nanowire single-photon detectors," vol. 17. https://doi.org/10.1109/TASC.2007.898660.

Yeh, Jen Hao, and Steven M. Anlage. 2013. "In situ broadband cryogenic calibration for two-port superconducting microwave resonators." *Review of Scientific Instruments* 84 (3). https://doi.org/10.1063/1.4797461.

Young, E. T., E. E. Becklin, P. M. Marcum, T. L. Roellig, J. M. De Buizer, T. L. Herter, R. Güsten, et al. 2012. "Early science with SOFIA, the stratospheric observatory for infrared astronomy." *Astrophysical Journal Letters* 749 (2). https://doi.org/10.1088/2041-8205/749/2/L17. arXiv: 1205.0791.

Zadeh, Iman Esmaeil, J. Chang, Johannes W.N. Los, Samuel Gyger, Ali W. Elshaari, Stephan Steinhauer, Sander N. Dorenbos, and Val Zwiller. 2021. "Superconducting nanowire single-photon detectors: A perspective on evolution, state-of-the-art, future developments, and applications." *Applied Physics Letters* 118 (19). https://doi.org/10.1063/5.0045990.

Zmuidzinas, Jonas, and Paul L. Richards. 2004. "Superconducting detectors and mixers for millimeter and submillimeter astrophysics," vol. 92. https://doi.org/10.1109/JPROC.2004.833670.